2007

FINITE ELEMENT MODELING OF AN INFLATABLE WING

Johnathan Rowe
University of Kentucky, jmrowe0@engr.uky.edu

ABSTRACT OF THESIS

FINITE ELEMENT MODELING OF AN INFLATABLE WING

Inflatable wings provide an innovative solution to unmanned aerial vehicles requiring small packed volumes, such as those used for military reconnaissance or extra-planetary exploration. There is desire to implement warping actuation forces to change the shape of the wing during flight to allow for greater control of the aircraft. In order to quickly and effectively analyze the effects of wing warping strategies on an inflatable wing, a finite element model is desired. Development of a finite element model which includes woven fabric material properties, internal pressure loading, and external wing loading is presented. Testing was performed to determine material properties of the woven fabric, and to determine wing response to static loadings. The modeling process was validated through comparison of simplified inflatable cylinder models to experimental test data. Wing model response was compared to experimental response, and modeling changes including varying material property models and mesh density studies are presented, along with qualitative wing warping simulations. Finally, experimental and finite element modal analyses were conducted, and comparisons of natural frequencies and mode shapes are presented.

KEYWORDS: Finite Elements, Inflatable Wings, Unmanned Aerial Vehicle, Modal Analysis, Internal Pressurization

Johnathan Rowe

August 7, 2007

FINITE ELEMENT MODELING OF AN INFLATABLE WING

By

Johnathan Michael Rowe

Dr. Suzanne Weaver Smith
Director of Thesis

Dr. L. Scott Stephens
Director of Graduate Studies

August 7, 2007

RULES FOR THE USE OF THESES

Unpublished theses submitted for the Master's degree and deposited in the University of Kentucky Library are as a rule open for inspection, but are to be used only with due regard to the rights of the authors. Bibliographical references may be noted, but quotations or summaries of parts may be published only with the permission of the author, and with the usual scholarly acknowledgments.

Extensive copying of publication of the thesis in whole or in part also requires the consent of the Dean of the Graduate School of the University of Kentucky.

A library that borrows this thesis for use by its patrons is expected to secure the signature of each user.

Name Date

_____

_____

_____

_____

_____

_____

_____

_____

_____

_____

_____

_____

_____

THESIS

Johnathan Michael Rowe

The Graduate School

University of Kentucky

2007

FINITE ELEMENT MODELING OF AN INFLATABLE WING

THESIS

A thesis submitted in partial fulfillment of the
requirements for the degree of Master of Science in the
College of Engineering at the
University of Kentucky

By

Johnathan Michael Rowe

Lexington, Kentucky

Director: Dr. Suzanne Weaver Smith, Associate Professor of Mechanical Engineering

Lexington, Kentucky

2007

ACKNOWLEDGMENTS

I would like to thank my advisor Dr. Suzanne Smith for offering me such a challenging research project, and for offering guidance and insight throughout the course of my research. Through her role as my advisor she has helped me grow substantially as an engineer over the past few years.

The author would like to acknowledge Stephen Scarborough and Matt MacKusick at ILC Dover for performing experimental testing of the Vectran material and providing the data from those experiments. Thanks go to David Miller for performing additional experimental tests on the wings.

Former co-worker Dr. Jonathan Black must be acknowledged for his help in performing the experimental modal analysis and performing modal parameter estimation using the X-Modal software. Thanks to Andrew Simpson for his general knowledge of the wings, his help with performing experimental testing, and the use of his discount card for free drinks at Jimmy Johns.

Funding for this research was provided by a grant from The Kentucky Science and Engineering Foundation and also by fellowships from the Kentucky Space Grant Consortium and the Center for Computational Sciences at the University of Kentucky.

I must thank my parents, Kenzie and Beverly Rowe for their love and support throughout both my undergraduate and graduate careers, without which I would not be where I am today.

Finally, thanks must be given to The Crystal Method for recording *Vegas*, which served as excellent background music during the writing of this thesis.

TABLE OF CONTENTS

LIST OF TABLES

LIST OF FIGURES

CHAPTER 1: INTRODUCTION

An Unmanned Aerial Vehicle (UAV) is any aircraft that does not have a pilot onboard. Instead, UAV's are controlled from a remote location through the use of radio-control (RC), or by an onboard autopilot system. The most common uses of UAV's are by the military for surveillance or reconnaissance missions. Use of UAV's has the benefit of allowing missions to be completed without risking human lives. In addition, by removing the pilot element from the overall flight mission equation, UAV's allow for more freedom in mission objectives, such as the ability to lengthen flight times. Also, UAV's have the potential to be less expensive than standard aircraft, as no accommodations are needed for an onboard pilot, for example, lesser environmental or atmospheric accommodations are needed for high-altitude flight. UAV sizes range from very large to micro [1]. The focus of this thesis is on the class of small (~ 6 ft wingspan) UAVs.

In addition to military uses, another application that a UAV is especially well suited for is extra-planetary exploration, most specifically Mars. A Mars airplane would allow for a more detailed view of the planet's surface than a satellite, yet can cover a larger area than a rover. One major challenge in deployment of a Mars glider is the problem of getting such an aircraft to Mars to be deployed. The concept of inflatable wings provides a unique solution to the problem of stowing an aircraft in a small volume. The wings can be packed in a deflated state in a volume many times smaller than the final deployed volume of the wings, and then once the aircraft is released from the launch vehicle, the

wings can be inflated to their full span. Figure 1.1 shows a conceptual image of what a Mars glider employing inflatable wings might look like.

Low-pressure inflatable wings provide a promising solution to defense applications by allowing for concepts such as “backpack” UAV’s, where a soldier could carry a lightweight aircraft stowed in a backpack. When needed, the aircraft could be inflated and deployed by the soldier for front-line surveillance.

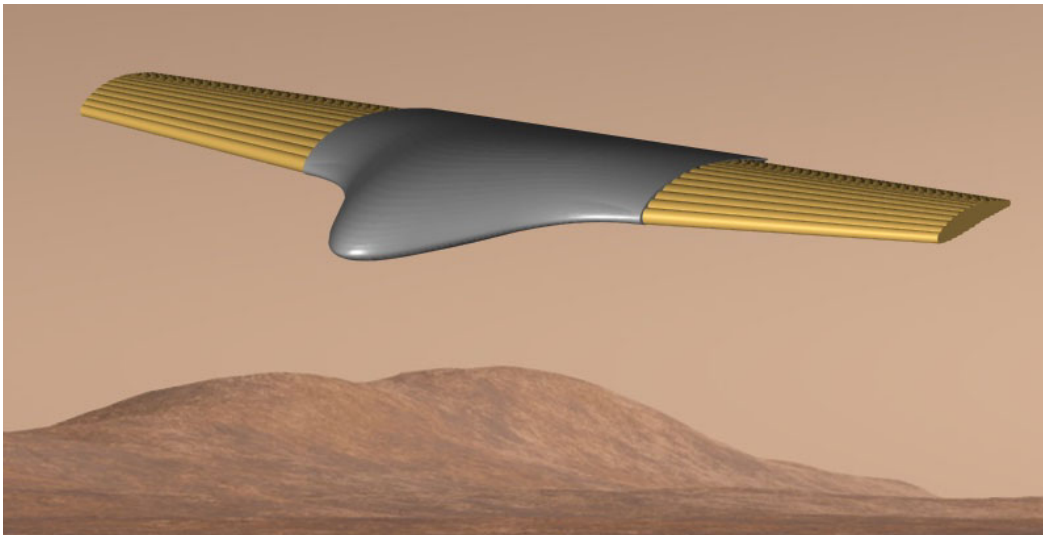

Figure 1.1 – Conceptual configuration of a Mars glider employing inflatable wings

1.1 Motivation

The flexible nature of inflatable wings lends itself to the concept of wing warping, changing the shape of the wing during flight, much like a bird. The ability to change the shape of the wing increases the flight performance capabilities of the aircraft, as well as the number of applications the wings could be used for. Strategies for actuating wing warping range from simple actuators to more advanced concepts involving smart materials.

A finite element (FE) model is desired to evaluate wing warping strategies and actuation implementation designs in order to reduce lengthy trial and error design cycle

times. Ultimately, the interest in the development of a finite element model of inflatable wings lies in the desire for the ability to predict responses of the wings to combined-loading situations including applied aerodynamic loads from wind tunnel or actual flight testing and forces applied to change the shape of the wings. Of course in order to predict unknown responses, the model of such a complex structural system must first be validated through comparisons of results from FE analyses and experiments, which is where the majority of the focus of this thesis lies. For this complex system, phased validation is necessary, ranging from material properties and simpler pressurization models, to static response to external loads, and finally to dynamic response.

1.2 Objectives

Therefore, the objectives for this research are outlined as follows:

- Determine the response of an inflatable wing.
    - Investigate the material properties of Vectran.
    - Perform experimental tests on the wing to determine static response to bending and torsion loads.
    - Determine dynamic characteristics of the wing through an experimental modal analysis.
- Develop a FE model that can be used to predict wing response.
    - Combine methods previously used to model inflatable structures and morphing inflatable wings.
    - Validate the model through comparison of FE simulations and experimental results.
    - Use the FE model to predict responses to wing warping loads.

1.3 Overview of Thesis

In this thesis, Chapter 2 provides a literature review of previous work on inflatable wings, as well as previous attempts to model inflatable structures, using both analytical and FE methods. Material property testing performed by the wing manufacturer is discussed in Chapter 3, along with static testing performed on the wing for this research. Chapter 4 discusses the FE modeling process of the inflatable wing, as well as FE simulations to static load cases. Chapter 5 gives a description of experimental modal testing performed on the wing, as well as FE predictions of the natural frequencies and mode shapes of the wing. Finally, Chapter 6 presents a summary of the work contained herein as well as possibilities for future work.

CHAPTER 2: BACKGROUND

Inflatable structures provide unique solutions for designs requiring small packed volumes. The concept of inflatable wings was developed decades ago, but a new cycle of research and innovation is underway. New missions are being considered, requiring unique packaging solutions and employing new materials to address previous concerns. Inflatable wing technology is being studied as an alternative for small UAVs providing packaging advantages and opportunities for wing warping or morphing [2-5]. Development of morphing technology for inflatable wings is of interest because it allows for adjustments to be made to the profile of the wing during flight, thus enlarging the flight envelope for the aircraft. New materials address previous concerns about punctures and deflation. Wings can be constructed of rigidizable fabric composites that harden after deployment and exposure to UV radiation or of rugged woven materials to prevent damage [6-9]. Inflatable wing technology is also being studied as a feasible option for extra-planetary exploration, particularly for Mars [10, 11]. To date, four successful high-altitude balloon experiments have demonstrated deployment of inflatable wings at low density, low temperature conditions [12-15].

2.1 Early Inflatable Wing Technology

An early example of inflatable aircraft technology is the Goodyear Inflatoplane. Goodyear Aircraft Company designed and built this aircraft as a plane that could be dropped uninflated from an aircraft to downed pilots behind enemy lines. The pilot could then inflate the plane and use it to escape. The aircraft was able to be inflated using less pressure than a car tire in approximately five minutes. The project began in 1956 and was

finally cancelled in 1973. Twelve Inflatoplanes were built during the course of the project [16].

Figure 2.1 – Model GA-468 Goodyear Inflatoplane

Inflatable wings were developed for an unmanned aircraft in the 1970's by ILC Dover with the Apteron R/C plane shown in Figure 2.2. The wingspan of the Apteron was 5.1 ft, and the aircraft had a total weight of 7 lbs. Propulsion was provided by a 0.5 HP engine, and elevons provided control.

Figure 2.2 – Apteron R/C UAV designed by ILC Dover [17]

2.2 Recent Developments in Inflatable Wing Technology

ILC Dover has more recently resumed efforts on inflatable wing technology, and has developed many inflatable and inflatable/rigidizable wings which have been documented extensively elsewhere [5, 8, 9, 12-14, 18-20]. Inflation pressures are generally low, ranging from 7 to 27 psig. ILC Dover is the manufacturer of the wings considered in this thesis.

In 2001, NASA Dryden successfully demonstrated in-flight deployment of an inflatable wing aircraft followed by a successful low-altitude glide. The I-2000 UAV employed wings developed by Vertigo Inc. for use by the U.S. Navy. The wings were constructed of cylindrical, inflatable spanwise spars that ran from wingtip to wingtip, with a wingspan of 64 in. and a chord length of 7.25 in [4]. The wings were designed for inflation pressures ranging from 150 psi to 300 psi. Figure 2.3 shows the release and inflation sequence of the UAV.

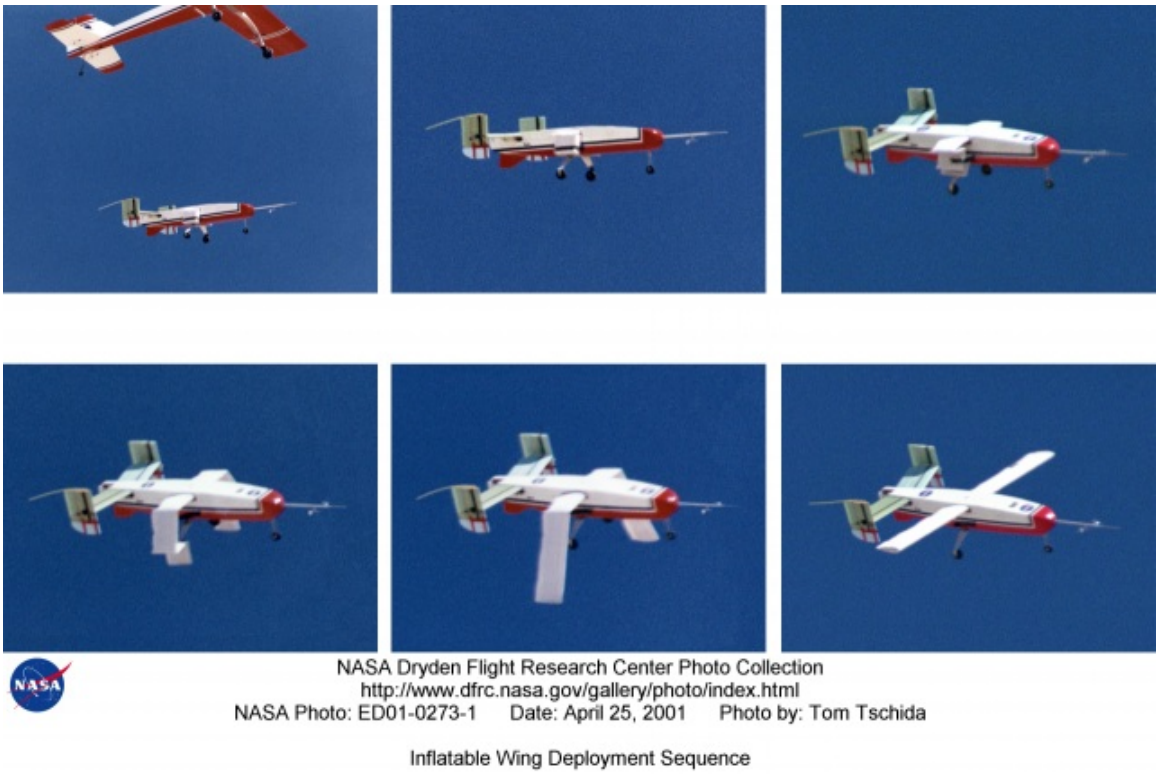

Figure 2.3 – Deployment and inflation sequence of NASA Dryden's I-2000 UAV

Work has been done at the University of Kentucky to verify the feasibility of inflatable wing technology for use on a planetary scout aircraft; most notably, an inflatable wing "scout" glider for Mars exploration. The BIG BLUE project (Baseline Inflatable-wing Glider Balloon Launched Unmanned Experiment) is an undergraduate program at the University of Kentucky in which high-altitude tests are conducted by sending inflatable wings to roughly 100,000 ft on weather balloons. At this altitude, the atmospheric density is similar to that seen at flight level on Mars. Each year, a new group of students participated in the project, with a high-altitude balloon launch or other major flight test being the final goal each Spring. To date, there have been five BIG BLUE mission groups, with four of those culminating in high-altitude balloon launches, each increasing in complexity toward a final high-altitude flight mission. For the final mission,

the end goal was to inflate the wings during ascent, allow the wings to cure, and then when the balloon reached critical altitude , the gliders would fly back to a designated landing location [12, 15].

The first two years of the BIG BLUE project proved the feasibility of inflatable/UV-rigidizable wings. The BIG BLUE I balloon launch marked the first time that this technology had been demonstrated. The wings considered in these projects were designed by the University of Kentucky in conjunction with ILC Dover, and contained a UV-curable resin so that after the wings were inflated, internal pressurization was only required for approximately 20 minutes while the resin cured and the wings became rigid.

Figure 2.4 – BIG BLUE II glider after recovery with rigidized wings

Beginning with BIG BLUE 3 in 2005, the focus of the project moved from inflatable/rigidizable to purely inflatable wing technology. BIG BLUE 3 culminated with a successful high-altitude balloon launch with the sole purpose of testing the design of an inflation system to inflate the wings at high-altitude, and maintain pressure as the wings returned to earth under a parachute. The wings considered during this project – the same wings that are the focus of the research in the later chapters of this thesis – are described in Section 2.7. Figure 2.5 shows the deployment of the wing at an altitude of approximately 98,000 ft [13]. The following year, BIG BLUE 4 did not culminate in a high altitude balloon launch as previous years had. The focus that year was to take the successes of the previous year and develop an unmanned aerial vehicle utilizing inflatable wings. The AIRCAT UAV with inflatable wings is shown in Figure 2.6.

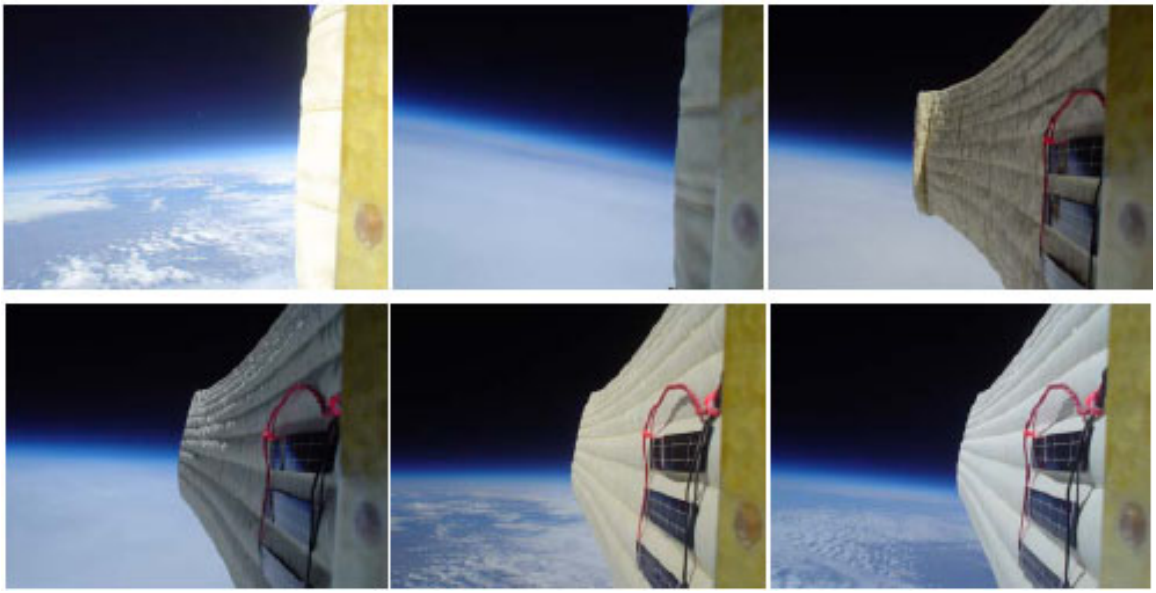

Figure 2.5 – High-altitude deployment of inflatable wing, April 30, 2005

Figure 2.6 – AIRCAT UAV with inflatable wings

BIG BLUE V brought the project full circle with a high altitude launch of a lightweight glider with new, lower-pressure inflatable wings. All subsystems functioned during the launch and ascent, but a problem with the mechanism used to restrain the wings in the stowed position led to a critical failure of one wing. As such, the final portion of the mission, a low altitude glide controlled by the autopilot, was unable to be executed.

Figure 2.7 – BIG BLUE V glider, just before high-altitude launch.

2.3 Morphing Inflatable Wings

Extensive research has been conducted at the University of Kentucky by Jacob and Simpson on developing UAV's with inflatable wings and varying methods of wing warping [2, 3, 6, 7, 19-28]. An effective summary of this testing will be presented in Simpson's PhD Dissertation, published in 2007 [29].

An inflatable wing constructed of urethane coated nylon is shown in Figure 2.8 with an early method of actuating warping for roll control. This wing, manufactured by ILC Dover, is currently undergoing testing at the University of Kentucky to explore warping capabilities and flight performance as shown in Figure 2.9.

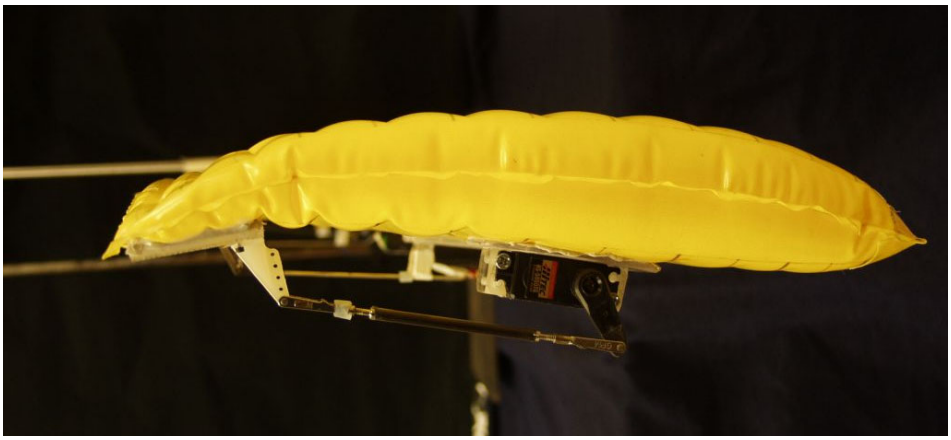

Figure 2.8 – Low pressure inflatable wings with attached warping mechanism.

Figure 2.9 – In-flight photo of inflatable wing aircraft with servo actuated wing warping.

2.4 Previous Analytical Modeling of Inflatable Structures

Some understanding of response of inflatable wings can be gained through analytical models and experimental studies of static loading and deployment response of inflated cylinders and of spacecraft structures composed of inflated cylinders [30-33]. Main et al. developed an analytical model for inflatable cylinder beam bending which closely correlated to experimental testing [31]. This model expanded on previous work by

accounting for the beam fabric's biaxial stress state, and its effect on the onset of wrinkling. The model also accounts for the bending behavior of the beam after wrinkling has occurred.

Analytical models for the response of inflated cylinders have been developed for the prediction of static and dynamic response of inflating beams and for aeroelastic response of inflatable wings for UAVs [34, 35]. Analytical modeling approaches have also been applied to inflatable torus structures [36].

Researchers at NASA Dryden developed an analytical prediction of beam bending as a supplemental effort to the I-2000 UAV [4]. In order to validate this analytical model, comparisons to experimental testing were performed. This experimental testing showed that over the range of pressures tested (150-300 psig) the initial slope of the load-deflection curve was equivalent until the onset of wrinkling. In effect, it was seen that the benefit of higher wing pressure is to expand the pre-wrinkle load range. The analytical models developed correlated well to the experimental bending results, though other types of loading were not considered. A finite element approach was also considered, but results were not presented.

In Griffith's Master's thesis, work is presented on an experimental modal analysis of an inflatable torus, as well as analytical methods to predict natural frequencies and mode shapes [36]. One method of estimating natural frequencies considered by Griffith was the use of circular ring models including bulk properties for the inflated system. It was found that a finite element approach incorporating shell elements and prestress effects from internal pressure loading was more accurate than using the analytical ring models. In order to develop an accurate circular ring model, the frequency-dependent dynamic

modulus of the structure is needed, thus limiting the usefulness of this method as a pre-test model.

2.5 Previous Modeling of Inflatable Structures using Finite Elements

FE models of inflatable/rigidizable wings were created previously by Usui as part of the design effort for the wings used in the BIG BLUE II project at the University of Kentucky [15]. The wings considered in this analysis contained a resin that would harden the wings when exposed to UV radiation. Once the wings were rigidized, internal pressure was no longer required. As the rigidized state was the flight state of these wings, the FE models included material properties of the rigidized wings and did not include internal wing pressures. These models included external aerodynamic loading as distributed loads with appropriate spanwise and chordwise profiles. The wing models developed by Usui are similar in concept to those considered in the later chapters of this thesis. The FE modeling work done by Usui was an important reference for the work contained in this thesis, and the general idea was to take the methodology used by Usui and expand it to model wings that required internal pressurization to maintain their shape.

Previous FE modeling of an inflatable structure which includes internal pressurization was performed by Griffith at the University of Kentucky.[36] FE modal analyses of an inflatable Kapton torus were performed with natural frequencies and mode shapes being correlated to experimental results. Two FE models were created for this purpose, one modeling the torus with beam elements and using bulk properties for the inflated system, and one modeling the torus with shell elements and performing a two-step solution process: first applying internal pressure loading to the model, and then performing a modal analysis incorporating these prestress effects. Griffith found that using this FE

shell modeling approach, the natural frequencies of the torus can be modeled within 30% of those found experimentally. In fact, many frequencies were predicted more accurately than this 30% error value. The FE shell modeling approach was of most interest as a pre-test model, since it required no prior knowledge of the structure's dynamic modulus.

2.6 Previous Experimental Testing of Inflatable Structures

Experimental static testing has been performed previously on circular inflatable beams.

Experimental modal testing has also been conducted on inflatable structures. Slade et al. performed a modal analysis on an inflatable solar concentrator. The test was performed in both ambient and vacuum conditions [37]. Successful modal tests have also been conducted on an inflatable kapton torus. Song et al. and Griffith successfully used acoustic excitation to identify natural frequencies and mode shapes [36, 38].

2.7 Description of Test Article

The wing considered herein is manufactured by ILC Dover and consists of a gas-retaining polyurethane bladder contained inside a porous external structural restraint. The restraint is composed of a silicone-coated plain weave vectran fabric with a yarn count of 53x53. The yarns are made from 200 x 2 ply denier (400 denier total in each yarn) Vectran HS fiber. The breaking strength of the fabric is approximately 900 lbs/inch, with a coated fabric weight of 8.5 oz/yd^2. Restraint thickness is 0.013 in.

The two yarn orientations of a woven fabric are referred two as warp and fill. The warp yarn direction of the fabric generally has a higher modulus the fill yarns must be woven in and out of the warp fibers, making it more likely for the fill yarns to be crimped

or damaged. For the wing, the warp direction of the fabric restraint is oriented parallel to the wing span and the fill direction is oriented parallel to the wing chord. The fabric of the internal spars is also oriented with the warp direction parallel to the wing span.

The inflatable wing is designed such that constant internal wing pressure is required to maintain the wing shape. Design pressure is 27 psig (an order of magnitude less than the Dryden wing), though the wing has been successfully flight tested at values down to 5 psig with sufficient wing stiffness for low speed applications carrying small, low mass payloads. Most recently, the wings have been flight tested at the University of Kentucky at internal pressures ranging from 12-18 psig. The design uses internal span-wise spars separating inflation cavities to help maintain structural stiffness at lower internal pressures. The outer restraint and internal spars are constructed from high-strength Vectran woven fabric. Figure 2.11 shows the components of the wing.

Wing construction is completed by sewing the internal spars to the external restraint, and sewing the external restraint edges together along the wing trailing edge and the wing tip. This results in spanwise seams along the trailing edge and wing tip. A close up view of the rounded, seamed wing tip is shown in Figure 2.10.

Figure 2.10 – Close up view of wing tip.

The wing is constructed in semi-span sections that can be attached to an aircraft fuselage. Construction of the wings is such that the wings can be stored in volumes much smaller than the deployed wing volume. Figure 2.12 compares the deployed wing volume to the packed wing volume. The wing profile is based around a NACA 4318 with a 4 degree incidence angle. The taper ratio is 0.65 with an aspect ratio of 5.39 and a full span of approximately 6 ft. Wing dimensions are shown in Figure 2.13.

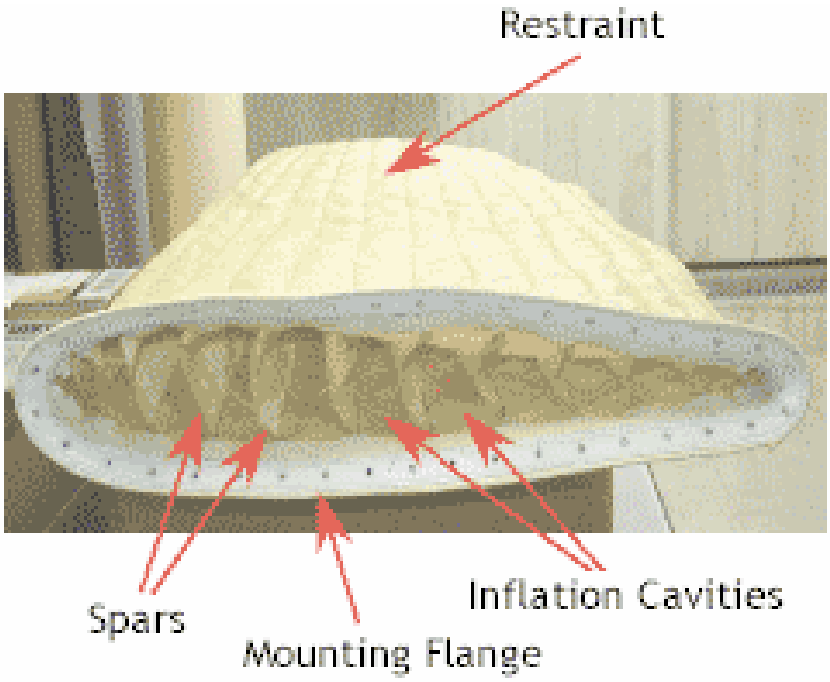

Figure 2.11 – Inflatable wing components. (Image provided by ILC Dover)

Figure 2.12 – Inflatable wings in packed and deployed configurations. (Image provided by ILC Dover)

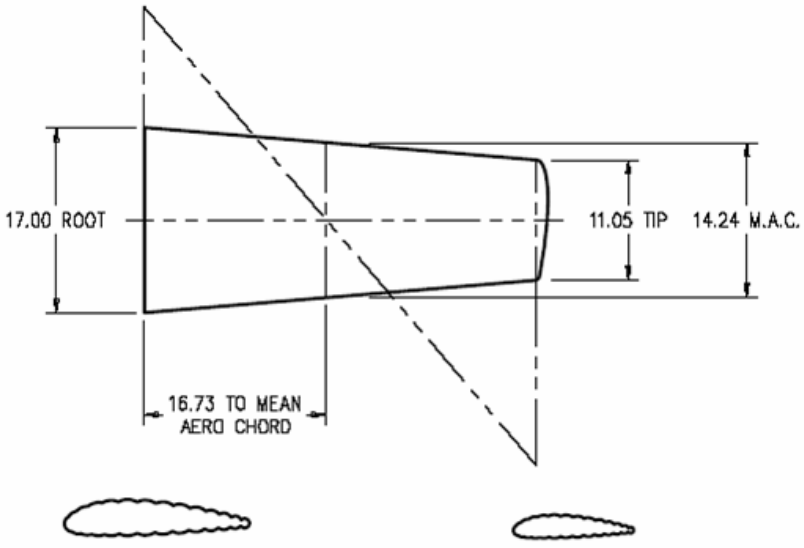

Figure 2.13 – Wing dimensions. (Image provided by ILC Dover)

CHAPTER 3: STATIC EXPERIMENTAL TESTING

In order to construct and validate a finite element model, experimental data is needed. This chapter presents the static experimental testing that was performed on the wings as well as material samples. Material testing was performed at ILC Dover to support manufacturing efforts, but is used here to determine constitutive properties. Tensile tests on strips of the Vectran wing restraint material were conducted to determine Young's Modulus properties, along with tests on inflatable cylinders to determine the shear modulus of the material. For this thesis, static experimental testing was performed on the wings to determine response to bending and torsion loads applied at the wing tip.

3.1 Tensile testing of Vectran strips

The Vectran material tested was a urethane coated 2x2 basket weave fabric with a thread count per inch of 48x48. The yarns were made from 400 denier Vectran HS fiber. The breaking strength of the fabric was approximately 950 lbs/inch with a coated fabric weight of 9.2 oz/yd^2. Sample strips of the material measuring 10 in. long and 2 in. wide were placed in tension in an Instron universal testing machine and tested using Federal standard test method 191-5104 "Ravel Strip Tensile." Strips were tested at a speed of 12 inches per minute to failure. The material was tested in both fiber orientations. Five samples of the warp direction and five samples of the fill direction were tested. The load-versus-deflection data was recorded and graphed to determine a tensile modulus in both directions. The ultimate load of each sample was also recorded during the testing. Resulting Young's moduli from the testing are presented in Table 3.1. The fill-direction modulus for the urethane-coated Vectran is 10.3% less than the warp direction. When the

finite element modeling process began, the only available tensile data was the data seen in Table 3.1 for the urethane-coated Vectran.

Table 3.1 – Initial Young's moduli determined from tensile testing of urethane coated Vectran.

	Young's Modulus, E	
Coating	Warp Direction	Fill Direction
Urethane	1360 ksi	1220 ksi

3.2 Shear Testing of Inflatable Cylinders

This section details a shear test performed to determine the shear modulus of the Vectran material. The test was conducted at ILC Dover, but is included in detail here because of its importance for this effort. The Vectran material tested was a urethane coated 2x2 basket weave fabric with a thread count per inch of 48x48. The yarns were made from 400 denier Vectran HS fiber. The breaking strength of the fabric was approximately 950 lbs/inch with a coated fabric weight of 9.2 oz/yd^2. It should be noted that the material of the inflatable wings is silicone-coated Vectran, and as such, proves less stiff than the Vectran samples used in this test. Without available test data using silicone-coated material, it was determined that resulting properties could be used with a reduction factor applied to approximate the material properties of the silicone-coated Vectran in the wings.

Two inflatable cylinders as shown in Figure 3.1 were used in the test, one with longitudinal warp fibers and one with longitudinal fill (hoop warp) fiber orientations. Each cylinder was loaded onto a test rig, with the coated side of the material on the inside of the cylinder, and the ends were clamped. Figure 3.1 shows this test set-up. The cylinder was then proof inflated to 40 psig +/-1 psig and this pressure was held for 2 minutes +/-3 seconds. The rate of inflation during this process did not exceed 5 psig/sec.

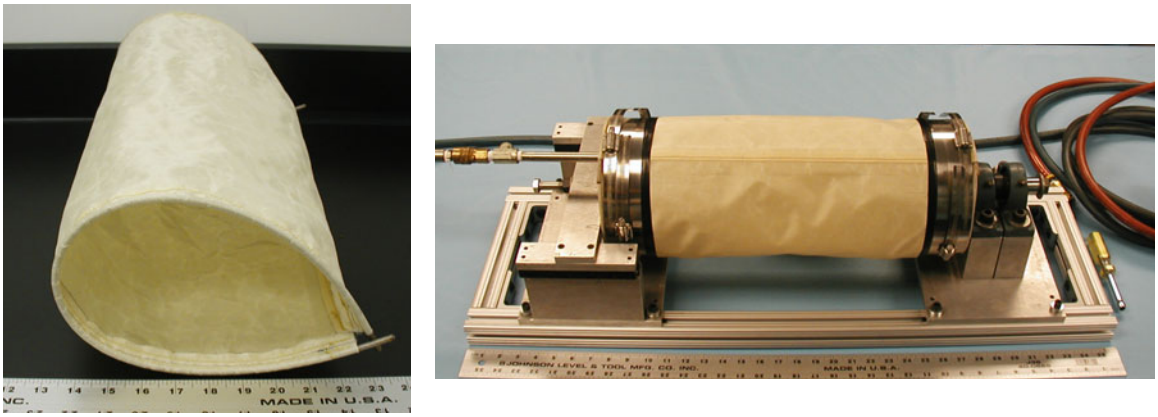

Figure 3.1 – Uninflated shear test cylinder and shear test setup. (Images provided by ILC Dover)

Once this initial set-up was complete, the cylinder was inflated to 1 psig and torques from 1 ft*lb to 9 ft*lb were applied to the cylinder in increments of 1 ft*lb, and angular displacement was recorded for each loading case. This process was then repeated for cylinder inflation pressures of 5, 10, and 20 psig. Then the entire above procedure was repeated for the second cylinder. Results of the tests are presented respectively in Figure 3.2 and Figure 3.3.

Shear stresses and strains were calculated from the experimental data using the following equations[39]:

$$\tau = \frac{Tc}{J} \tag{3-1}$$

$$\gamma = \frac{\phi c}{L} \tag{3-2}$$

Where: τ = shear stress
γ = shear strain
T = applied torque
c = radius of cylinder
J = cylinder moment of inertia
ϕ = angular displacement
L = Length of cylinder.

The shear modulus is the slope of the shear stress versus shear strain curve. Results for both fiber orientations show that the shear modulus increases with increased internal pressure. Results for both orientations also show a slight trend to softening under larger stress, although a linear approximation is reasonable. At the lower pressures, the two orientations have similar results, but the longitudinal warp test shows higher moduli than the longitudinal fill (hoop warp) orientation. Table 3.2 lists the resulting shear moduli for both fiber orientations, calculated by taking the slope of the best fit line through the data points in Figure 3.2 and Figure 3.3.

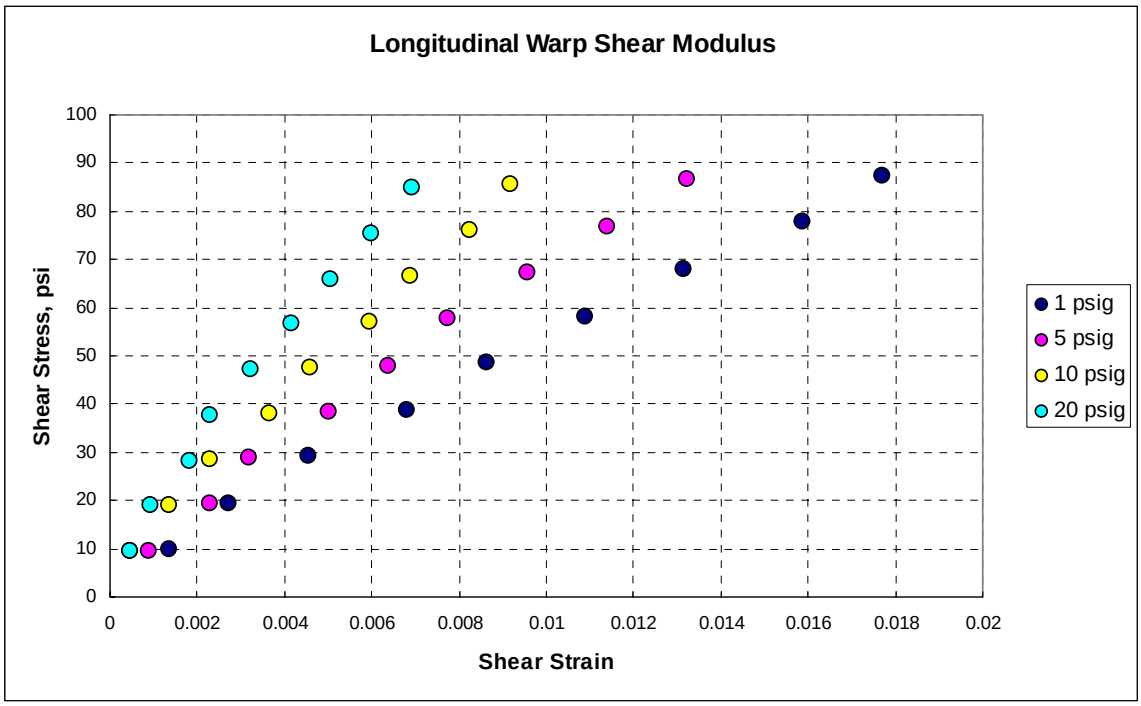

Figure 3.2 – Shear stress-strain diagram for cylinder with longitudinal warp

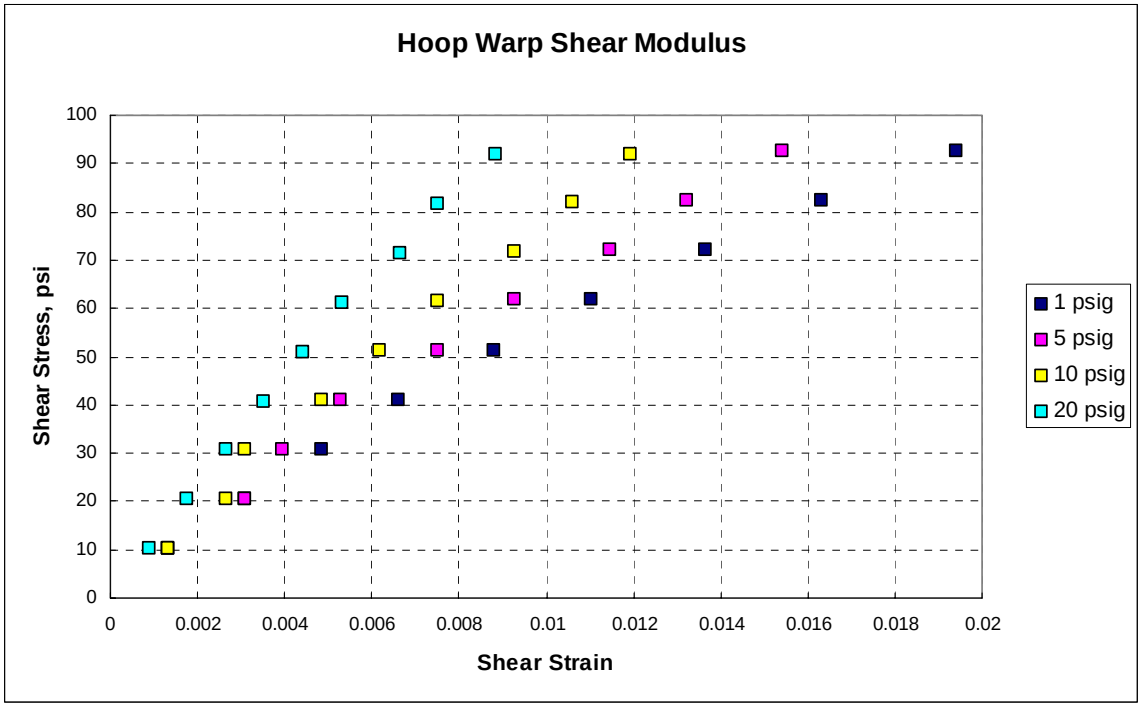

Figure 3.3 – Shear stress-strain diagram for cylinder with hoop warp

Table 3.2 – Experimentally determined values of shear moduli of urethane-coated Vectran

Internal Pressure, psi	Shear Modulus, ksi	
	Longitudinal Warp	Longitudinal Fill
1	4598	4554
5	6223	5771
10	8514	7491
20	11383	10345

3.3 Preliminary Static Bending Tests

3.3.1 Experimental Set-up

An experimental test measuring wing deflection due to cantilever bending was performed to determine wing response. The wing was mounted to a rigid test stand as shown in Figure 3.5, and upward vertical loads ranging from 2.25 lbf to 11.24 lbf (10 N to 50 N) were applied to the wing tip in increments of 2.25 lbf (10 N). Loads were applied at a location 1.5 inches from the inflated wing tip, inboard of the wing-tip seam

and transition region seen in Figure 3.5, and at a chord location 4.5 inches from the leading edge, coinciding with a spar location. This load placement was used to minimize twisting of the wing during the bending test. Also, because the load was applied at a spar/restraint interface, local deformation was minimized.

Loading was applied using a force sensor mounted on a precision linear stage. Stage height was increased until the desired loading was output from the sensor. A small rod was connected to the sensor to apply the load to the wing. The circular contact area between wing and rod had a diameter of 0.25 in. Internal wing pressures of 10, 15, and 20 psig were tested. Vertical deflections were recorded at 3 points shown in Figure 3.4: 1) wing tip at the point of load application, 2) wing tip at the leading edge, and 3) 18 inches from wing root (midpoint of semi-span) at the trailing edge. Vertical deflections were measured using a linear scale, taking initial location due to internal pressure and no tip load as reference.

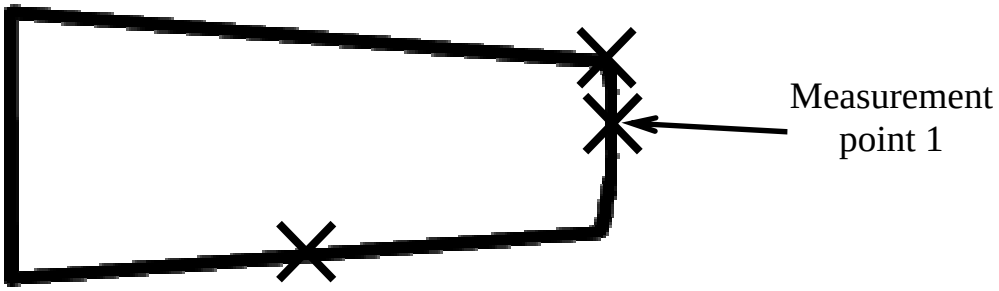

Figure 3.4 – Measurement points for initial bending test

Measurements were taken using the wing seam as a reference. Figure 3.6 shows resulting vertical deflections at measurement Point 1 due to loads applied at the wing tip for all internal pressures tested. These results are representative of those of the other measurement points. As the bending test was being performed, no noticeable twist was evident in the wing. Vertical deflections of both measurement points at the wing tip were

very similar for all pressure cases, showing that twisting of the wing was minimized during this bending test.

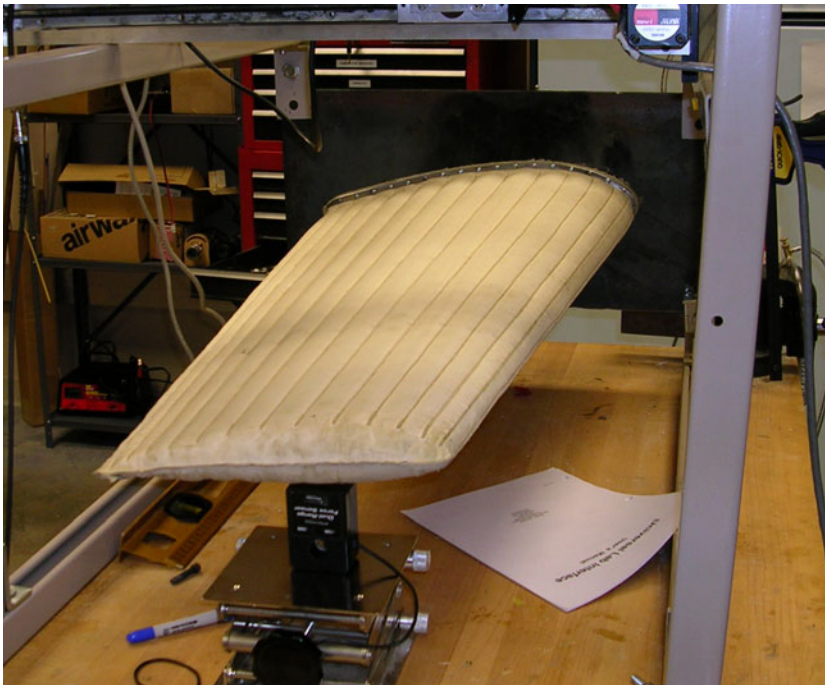

Figure 3.5 – Wing bending test set-up.

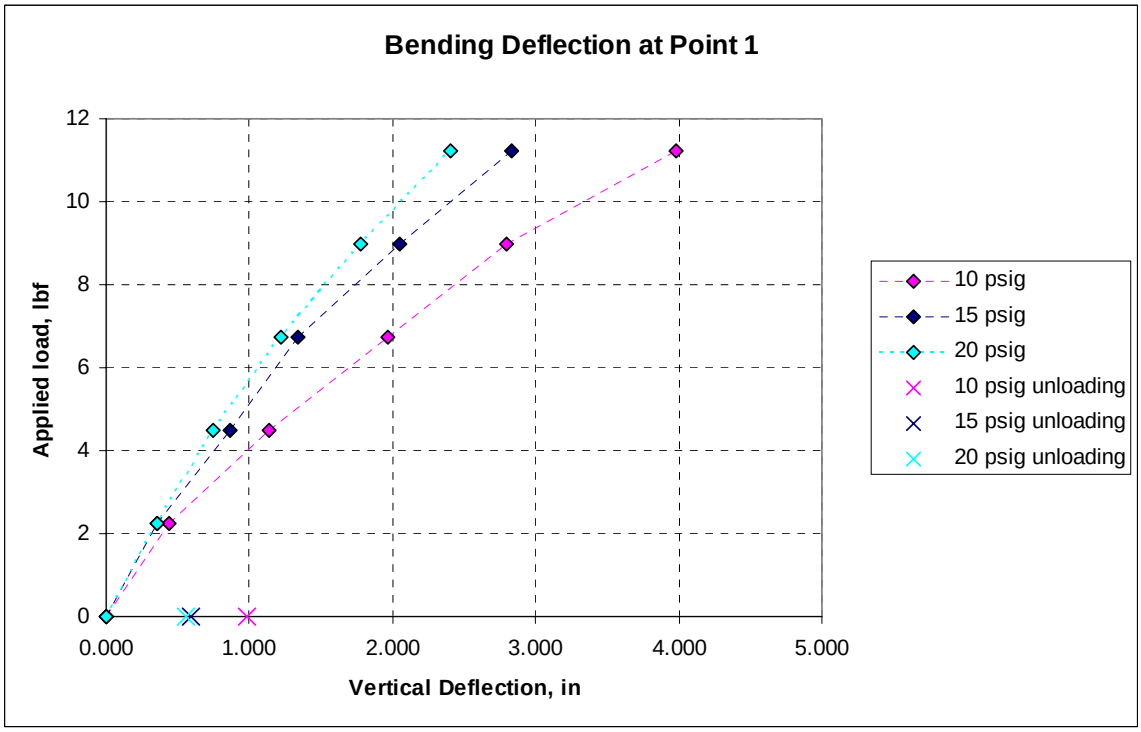

Figure 3.6 – Inflatable wing tip deflection results.

The bending test results show slightly softening behavior, as the load/deflection slope gradually decreases with increased load and deflection. The softening trend is more pronounced for the lowest pressure of 10 psig. Still, for all three pressures, a linear approximation of the incremental loading response is reasonable. As expected, wing deflection decreased with increasing internal pressure. For the highest loading case of 11.24 lbf, the highest internal pressure case, 20 psig, had a resulting wing tip deflection 60% of the wing tip deflection for the lowest internal pressure case, 10 psig. At an internal pressure of 15 psig, deflection at the wing tip was 71% of deflection for the 10 psig case. Note that while the wing stiffens with internal pressure, the increase in stiffness seen between 10 and 15 psig is larger than that seen between 15 and 20 psig.

Note that there are two deflection values corresponding to the applied load of 0 lbf for each pressure case. The first measurement taken at 0 lbf applied load was the reference point from which all deflections were measured and so is recorded here as 0 inches. When the wing was unloaded after applying the final largest load, the wing did not return to its original position. For the lowest pressure of 10 psig, the wing tip returned to a point nearly 1 inch from its original position; for the higher pressures of 15 and 20 psig, the wing tip returned to a position approximately 0.5 inches from the original position. Increasing internal pressure decreased this hysteresis effect. Note that this set of experiments did not include incremental unloading of the wing, so the full hysteresis effect was not determined from this test. Another series of experiments were conducted which provide more insight into the hysteresis of the system; these tests are documented in Section 3.4.

3.3.2 Wing Stiffness Calculations

The following results could be used for future design considerations, or by researchers interested in developing equivalent beam models of the inflatable wings.

Treating the wing as a linearly elastic cantilever beam with a tip load, the flexural rigidity of the wing can be calculated from Equation (3-3).[39]

$$EI = \frac{FL^3}{3\Delta} \tag{3-3}$$

Where: EI = Flexural Rigidity
F = Applied Tip Load
L = Beam Length
Δ = Beam deflection at tip

Wing flexural rigidity results are plotted in Figure 3.7 for the three pressures considered. As expected, the wing rigidity increased with internal pressure. Further, the rigidity decreased with increased load consistent with the softening trend seen in the force-deflection data. For the highest pressure, 20 psig, the rigidity decreased by approximately 30% over the load range; for the lowest pressure, 10 psig, the wing rigidity decreased by nearly half over the load range.

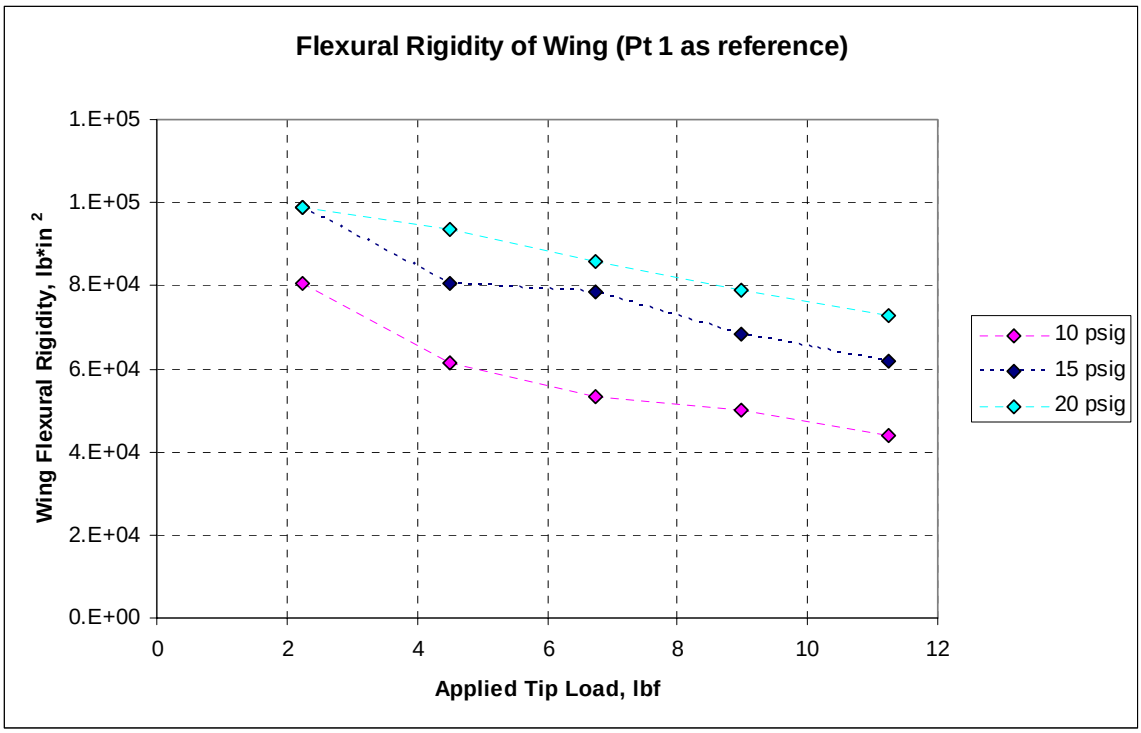

Figure 3.7 – Flexural rigidity of wing.

3.4 Revised Wing Bending Tests

Previous experimental bending tests of the wing measured vertical deflections at only three points on the wing; two points on the wing tip, and one at the mid-span of the trailing edge. To more fully observe the response of the wing, additional bending tests were conducted, with vertical deflections measured at multiple positions along the span of the wing along both the leading and trailing edges. The set-up for this test is shown in Figure 3.8. The wing was mounted to a rigid test stand, and upward tip loadings were applied to the wing one inch from the wing tip using a pulley/weight system. Loads were transferred to the wing by affixing strips of Vectran to the wing with RTV 157 silicone rubber sealant. After loading was applied to the wing, a linear scale was used to measure the vertical deflection of multiple points along the span of the wing with the unloaded inflated state of the wing taken as reference. Loadings of 2.25 lbf to 11.24 lbf (10 N to 50

N) were applied to the wing in increments of 2.25 lbf (10 N). After the maximum loading was applied, the wing loading was reduced to 6.74 lbf and then fully removed and deflections were measured at each state to determine the amount of hysteresis present in the system. This process was performed at wing pressures of 10, 15, and 20 psig.

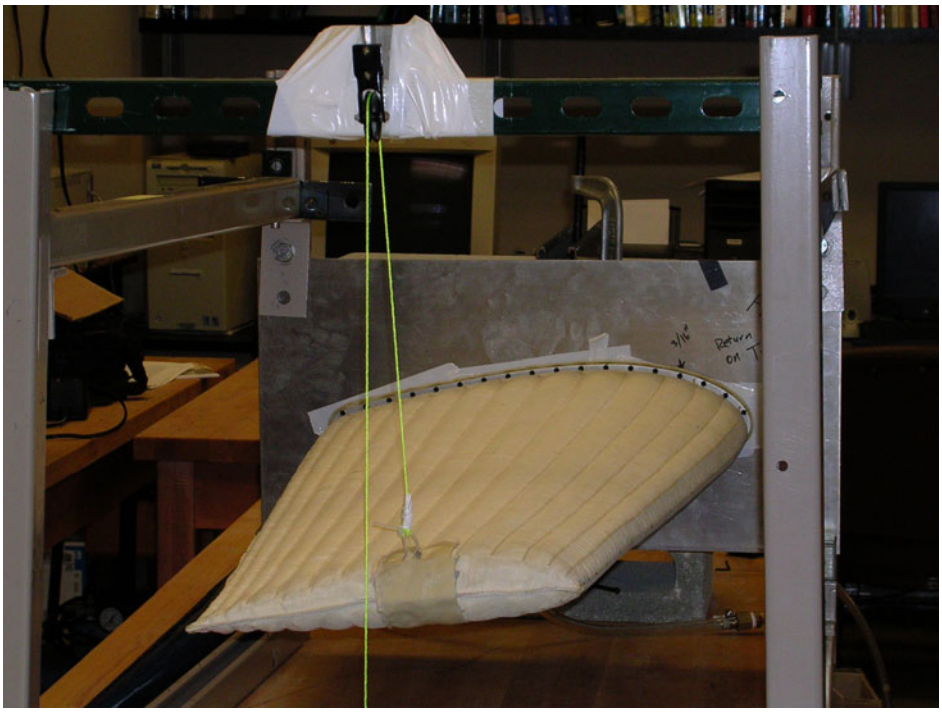

Figure 3.8 – Bending test set-up.

Figure 3.9 shows the vertical deflection of points along the span of the wing for tip loadings spanning this range, for an internal pressure case of 15 psig. Data sets plotted with square markers represent deflections as the wing was incrementally loaded with increasing loadings, while data sets plotted with triangular markers correspond to the wing displacements as the wing was unloaded. Note that when the wing was unloaded from a tip load of 11.24 lbf to 6.74 lbf, the wing did not return to the same position as when it was initially loaded, and actually remained with more deflection than the 8.99 lbf loading had caused. Also, when fully unloaded, the wing did not return to its original unloaded position. It in fact returned to a deflected position very near to that seen with a

tip loading of 4.50 lbf, with the wing tip returning to a position 1.25 inches above the original unloaded position. This hysteresis poses a challenge when attempting to model the wing, as the finite element model does not have the same “memory” that the actual wing material has.

In order to see how long the wing remains in a deflected state after loading is removed, the wing was inflated to 15 psig, loaded with a tip load of 11.24 lbf (50 N), and then unloaded. Vertical deflections at the leading and trailing edge of the wing tip were measured at the time of unloading and every 60 seconds afterward for 5 minutes, and then a final measurement of the vertical deflection was taken 10 minutes after the wing was unloaded. Resulting deflections are plotted vs. time in Figure 3.10. Figure 3.10 shows that after 10 minutes, the deflection at the wing tip position decreases by only approximately 0.5 in, to a deflection of approximately 0.75 in from the original position. During the course of this test, wing pressure slowly decreased from 15 psig to 11 psig at the time of the final data points due to a small leak in the inflation system setup. This decrease in pressure may account for the small change in position during the 10-minute test.

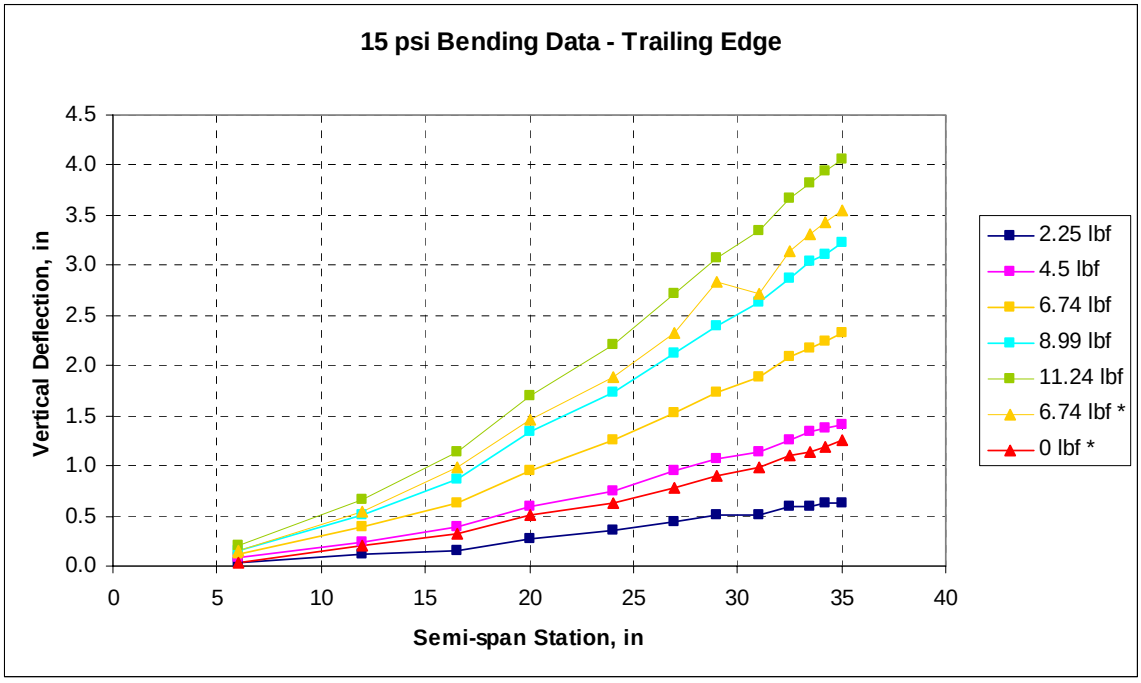

Figure 3.9 – Vertical wing deflections, 15 psig internal pressure.

**Corresponds to wing location while being unloaded from highest applied loading*

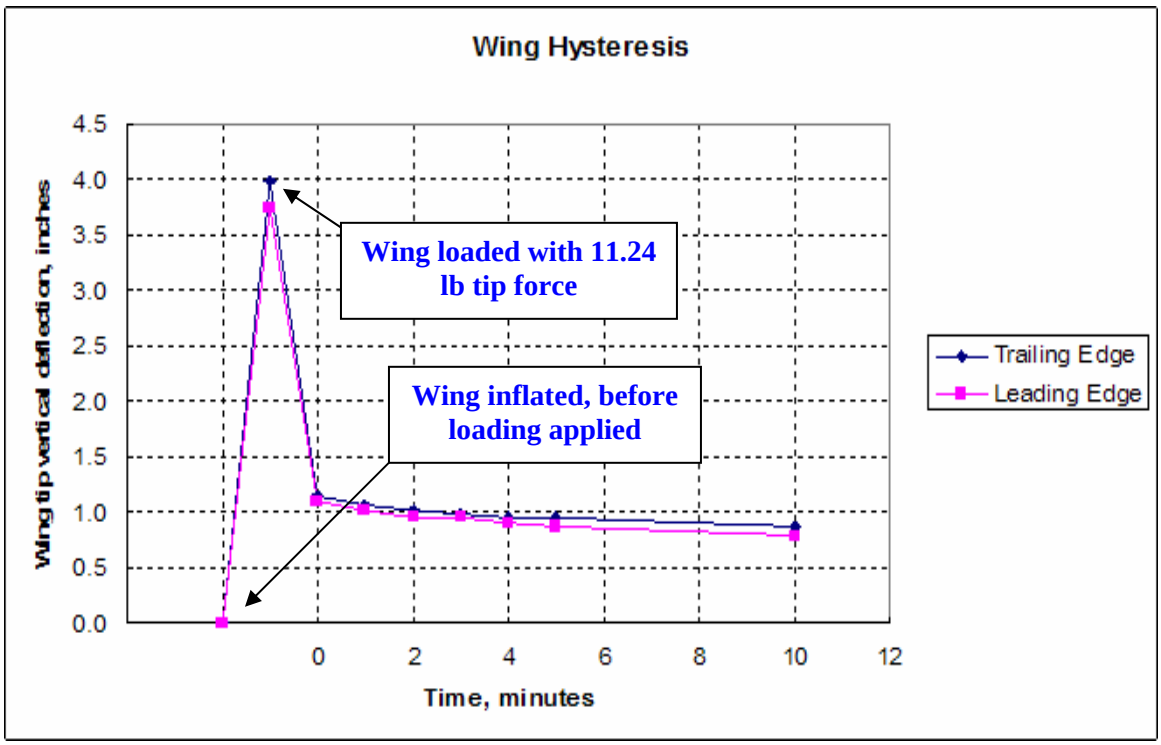

Figure 3.10 – Vertical deflection at wing tip after applying and removing 11.24 lbf loading

Figure 3.11 shows the vertical deflections along the span of the wing for internal pressures of 10, 15, and 20 psig. This plot shows, as expected, that wing stiffness increases with increasing internal pressure, and shows that the wing deflection is higher near the tip of the wing. Note that for all cases, the trailing edge deflection is higher than the leading edge deflection, with the difference at the wing tip being approximately 0.25 in. When conducting the test, deflections along the leading edge were measured first, from wing tip to wing root, and then deflections along the trailing edge were measured, from wing tip to wing root. Readings began immediately after loads were applied. After the test was completed and the data analyzed, the difference in deflection between leading and trailing edges was interesting, because there was no visible twist in the wing during the test. Upon further inspection, it was found that after load is applied to the wing tip, the wing continues to deflect upward approximately 0.25 in. over the next 45 to 60 seconds, though this deflection occurs slowly and was not easily noticeable during the test. Since leading edge measurements were taken first every time, by the time the trailing edge measurements were taken, this deflection had already occurred, producing the disparity in the results seen in Figure 3.11.

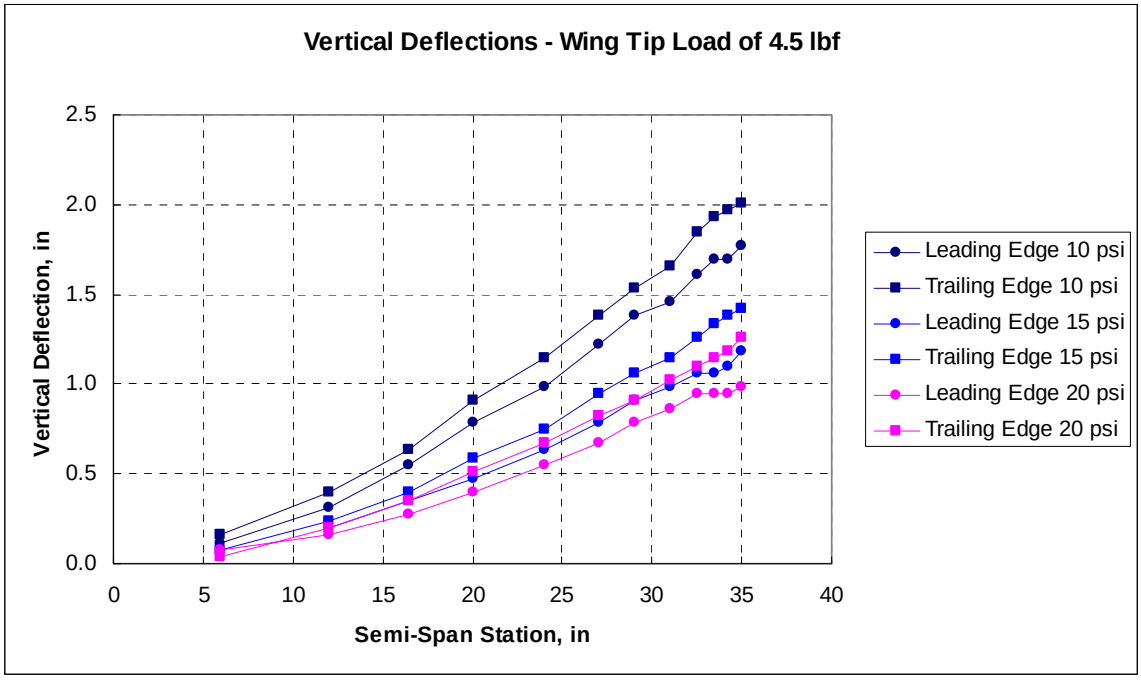

Figure 3.11 – Wing deflections, 4.5 lbf tip load over a range of internal pressures

It must also be noted that the wing used in this bending test is not the same wing that was used in the previous bending tests from Section 3.3. Figure 3.12 shows a comparison between tip deflections for the two wings over the range of internal pressures and tip loadings tested. Square data points correspond to the previously tested wing; while diamond shaped points correspond to the wing tested here. These wings are manufactured in the same manner, to the same specifications, but the wing response varies significantly. Between the times that each wing was tested, the current wing has been flight tested on aircraft, mounted and unmounted numerous times, and has been handled extensively by many students for other research projects. When this, along with the inherent variations in such a complex system constructed of a woven fabric, is taken into account such differences are not unexpected. At the lowest pressure of 10 psig, with the highest applied tip load of 11.24 lbf (50 N), the deflection at the wing tip was in test 2 was seen to be approximately 1.6 in larger than that seen in test 1 for the same loading case, a 33%

difference. The percent differences between the two tests for the highest tip load case for 15 psig and 20 psig are approximately 35% and 34% respectively.

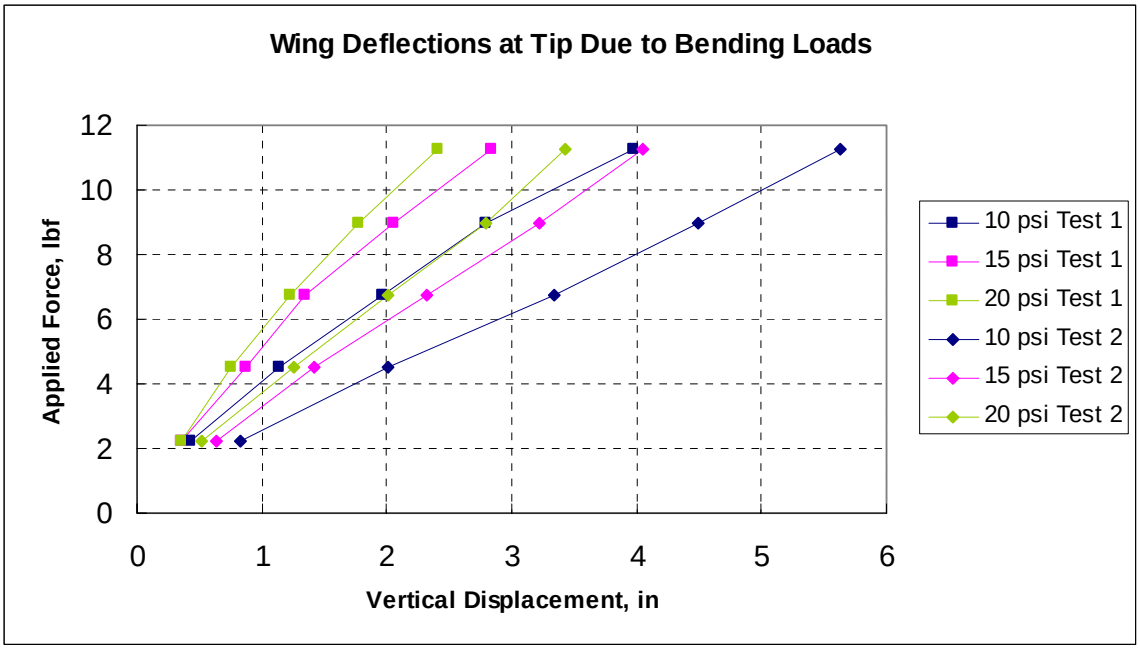

Figure 3.12 – Comparison between bending tests, deflections at wing tip shown.

Inspired by the difference in wing response seen in Figure 3.12, further testing was conducted to determine the range of response of different inflatable wings. Figure 3.13 shows the averages and standard deviations of the wing tip deflections for these tests. In this plot, it must be noted that data for three wings was included for tip loadings of 4.25 and 11.24, while data from only two wings was included for all other data points. In analyzing Figure 3.13, it is seen that the averages of the newest tests more closely correlate with bending Test 1 from Figure 3.12. This suggests that perhaps the range of response of the wings is not necessarily as large as originally thought, and perhaps the wing tested in Test 2 is an anomaly. At the same time, Figure 3.13 shows that there is a range to the response of the wings, which poses a challenge to creating a validated model of the response.

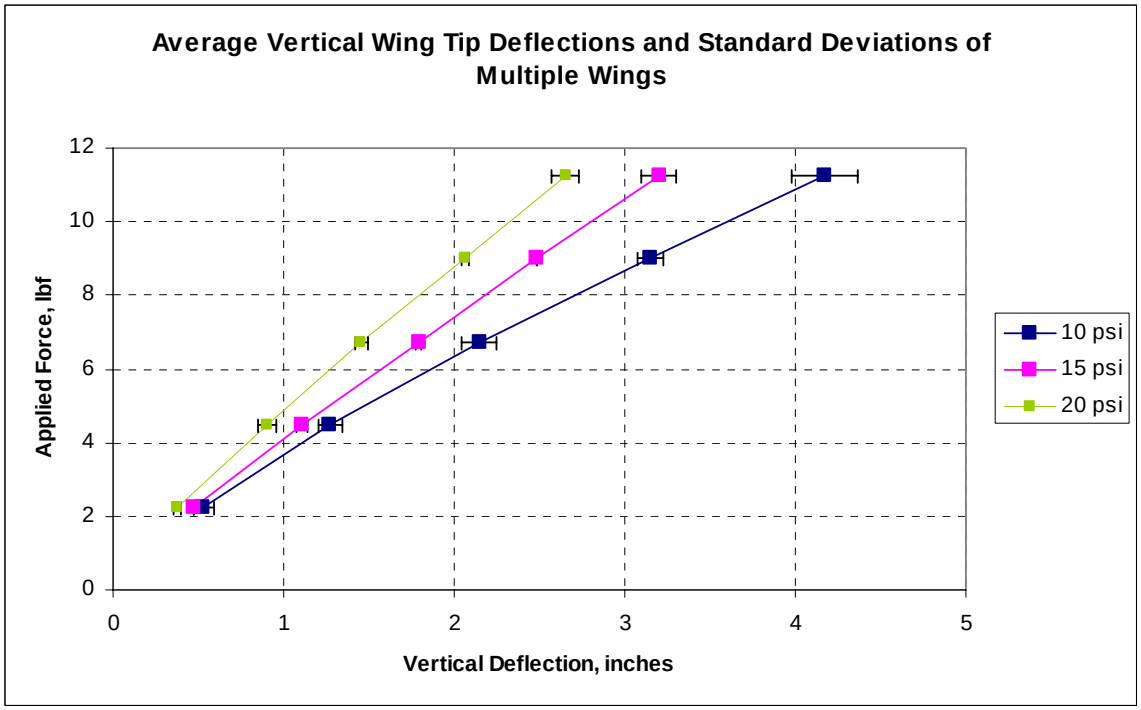

Figure 3.13 – Average vertical wing tip deflections and standard deviations of inflatable wings
**Note, four wings included for loadings of 4.25 and 11.24 lbf, three wings included for all other loadings.*

3.5 Wing Twist Tests

3.5.1 Experimental Results

The inflatable wing was tested to determine wing response due to twisting loads applied at the tip of the wing. The wing was mounted to a rigid test stand, just as in the previous bending test. Equal magnitude loadings were applied vertically to the leading and trailing edges of the wing tip to produce twisting deflections. Loadings were applied by attaching loops of Vectran material to the wing tips with silicone rubber adhesive and hanging weights (using a pulley for upward loading) from the wing. The loadings were applied at the tips of the leading and trailing edges, which are 35 inches from the wing root. Force transducers were used to measure the actual load applied to the wing. Loadings of 2.52, 4.77, and 7.01 lbf (11.2, 21.2, and 31.2 N) were applied at pressures

ranging from 10 to 25 psig, in increments of 5 psig. With the 11.75-inch chord-wise separation between the applied vertical loads, the applied moments are 29.6, 56.0, and 82.4 lb-in, respectively. Both clockwise and counterclockwise twisting loads were examined. Figure 3.14 shows the wing pressurized to 25 psig with applied loadings of 7.01 lbf (31.2 N) upward at the wing tip leading edge and downward at the wing tip trailing edge.

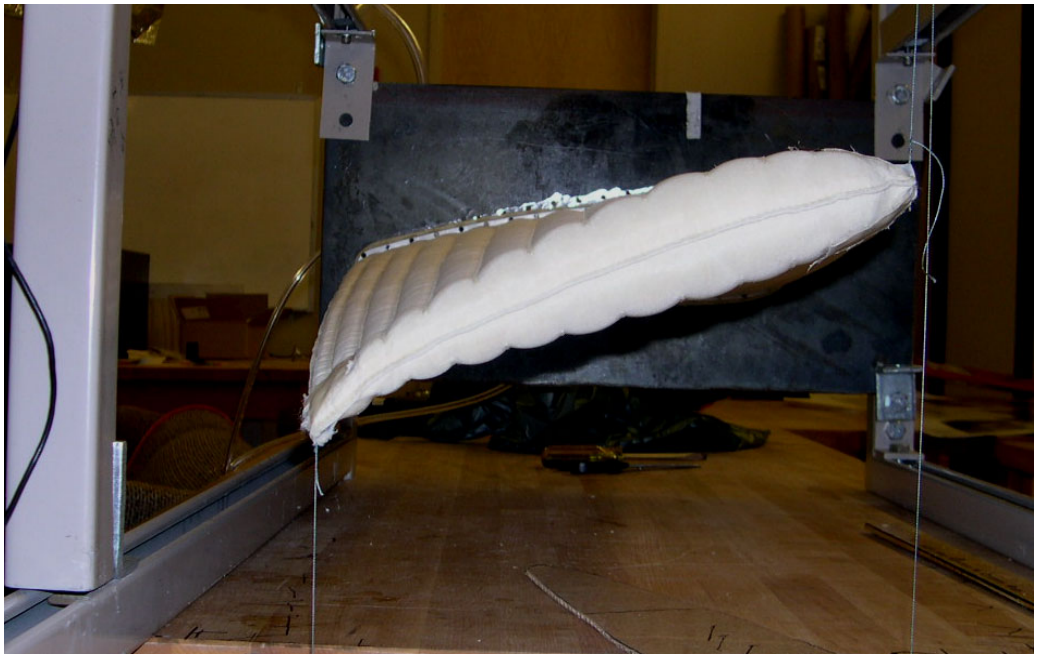

Figure 3.14 – Wing under 7.01 lb couple forces for twist loading and 25 psig internal pressure.

Vertical deflection was measured at several points along the span of the wing at the leading and trailing edges. Results are shown in Figure 3.15 for a counterclockwise twisting load and internal pressure of 15 psig. Clockwise loading results are not shown but Figure 3.15 is representative of the negative of the deflections for clockwise loading. In Figure 3.15, the leading edge vertical deflection under twisting load is seen to be less than that of the trailing edge. Note that data points corresponding to 0 lbf loading are deflections after the largest loading was removed, again showing hysteresis in the wing response. The leading edge shows only small final displacements along the span after

unloading. However, the trailing edge shows final unloaded displacements similar to the lowest loading and increasingly larger along the span to the wing tip. Incremental unloading was not measured. Figure 3.16 presents the dependence of the wing deflections on internal pressure. The deflections of the leading and trailing edges are larger for smaller internal pressures. The difference among the leading edge deflections over the range of all the pressures is much smaller than that of the trailing edge deflections. In addition to the hysteresis of the system that is evident from Figure 3.15, it can be seen from both results that the trailing edge of the wing is less stiff than the leading edge for all load cases.

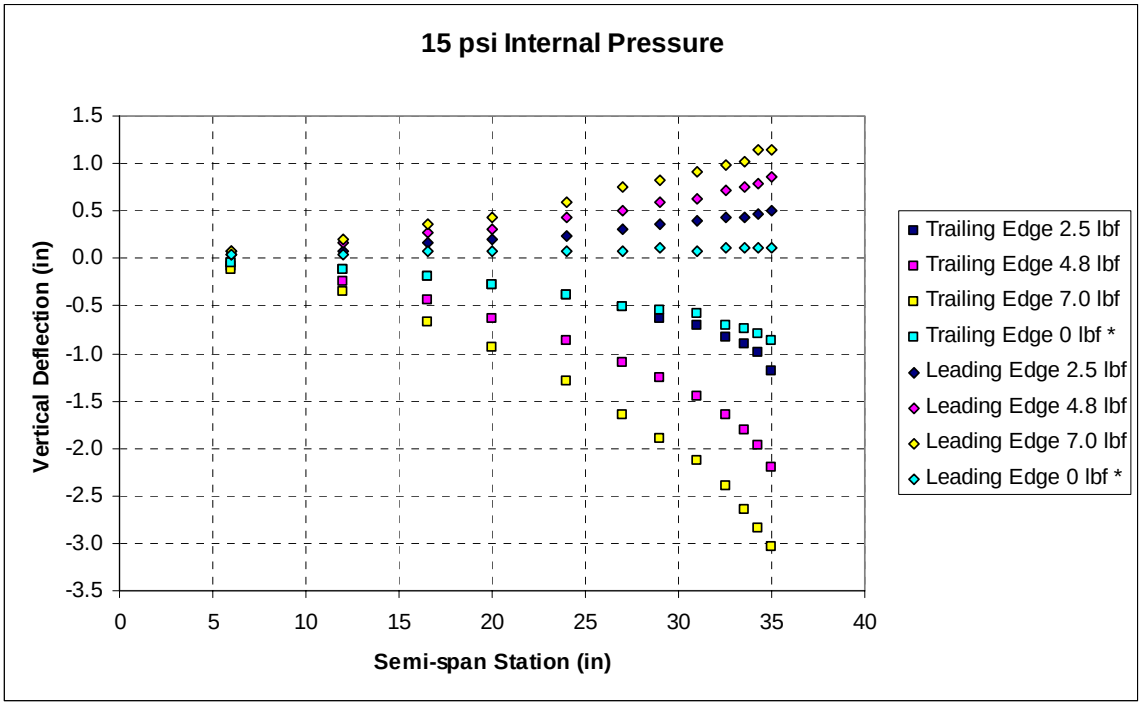

Figure 3.15 – Wing deflections, 15 psig internal pressure.

**Corresponds to deflections after all loading removed, not before loading applied*

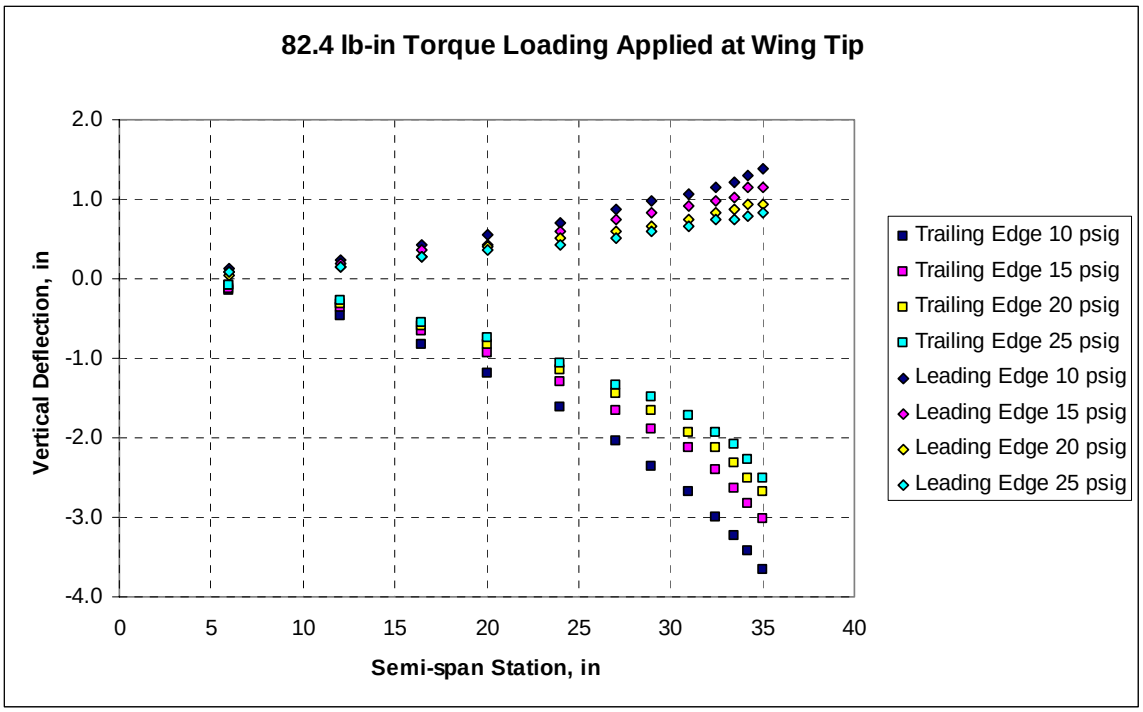

Figure 3.16 – Wing deflections, 82.4 lb-in applied torque.

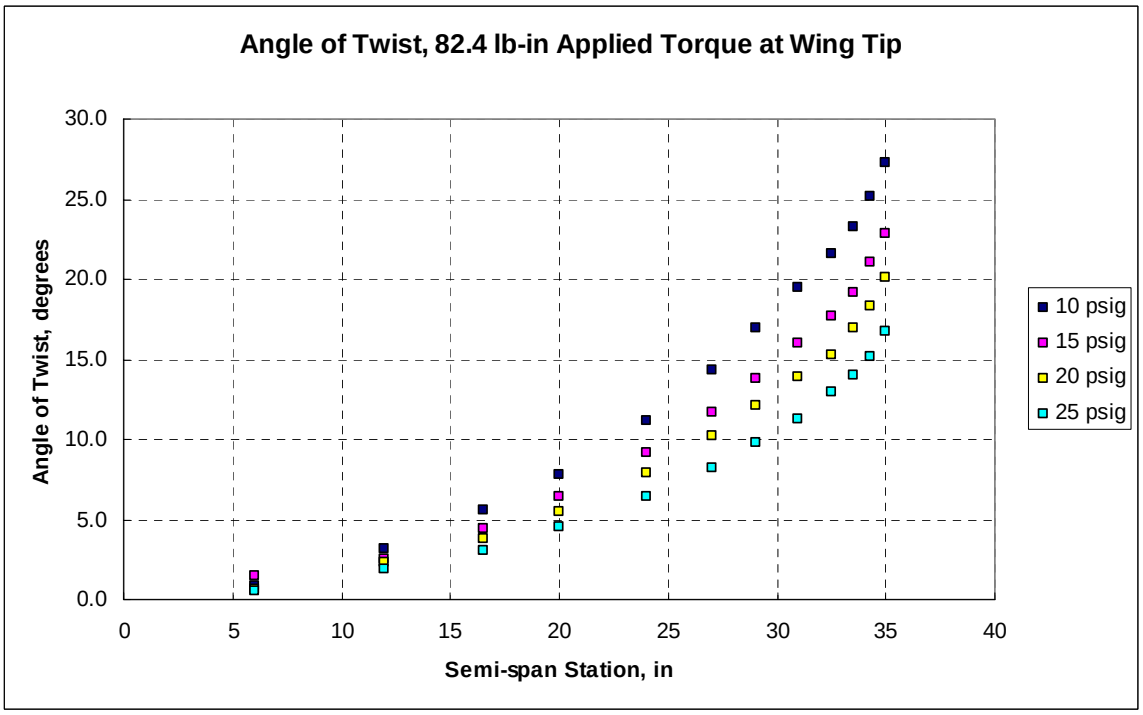

Figure 3.17 – Angle of twist of wing for 82.4 lb-in applied torque.

Figure 3.17 shows the angle of twist vs. semi-span station due to an applied torque of 82.4 lb-in, for all tested pressure cases. This figure shows the angle of twist due to a

counterclockwise torque load on the wing (leading edge deflected upward, trailing edge deflected downward). Clockwise torque results are similar. In Figure 3.17, the angle of twist was calculated using the local chord length and measured deflections of the leading and trailing edges.

3.5.2 Wing Torsional Stiffness Calculations

The following results could be used for future design considerations, or by researchers interested in developing equivalent beam models of the inflatable wings.

Similar to the bending results above, treating the wing as a linearly elastic cantilever beam with a torque load at the tip, the flexural rigidity of the wing can be calculated from Equation (3-4).[39]

$$GI_p = \frac{TL}{\phi} \tag{3-4}$$

Where: GI_p = Torsional rigidity
T = Applied torque load
L = Beam length
ϕ = Angle of twist

The resulting torsional rigidity calculations are plotted in Figure 3.18, for the three torque loadings considered and an internal pressure of 10 psig. The results vary for each loading and pressure similarly for each point along the semi-span of the wing; however, due to the scales of Figure 3.18 and Figure 3.19, this is not evident. However, if each span location is plotted separately, results resemble those near the wing root in Figure 3.18 and Figure 3.19.

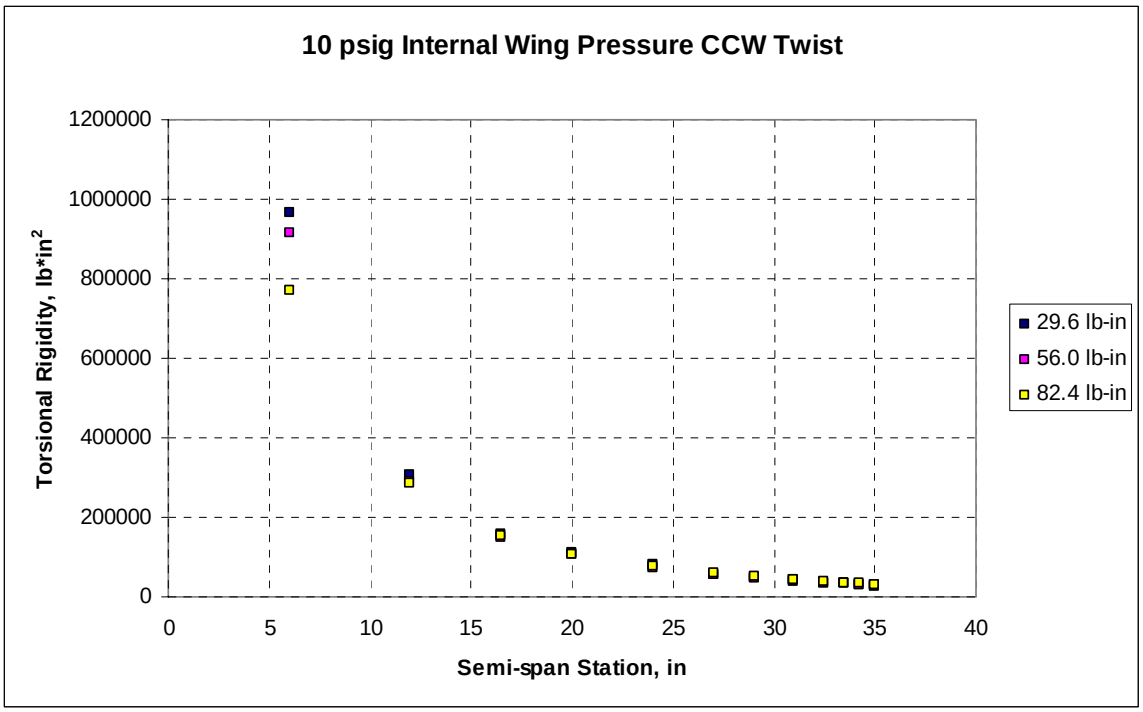

Figure 3.18 – Torsional rigidity of wing for 10 psig internal pressure.

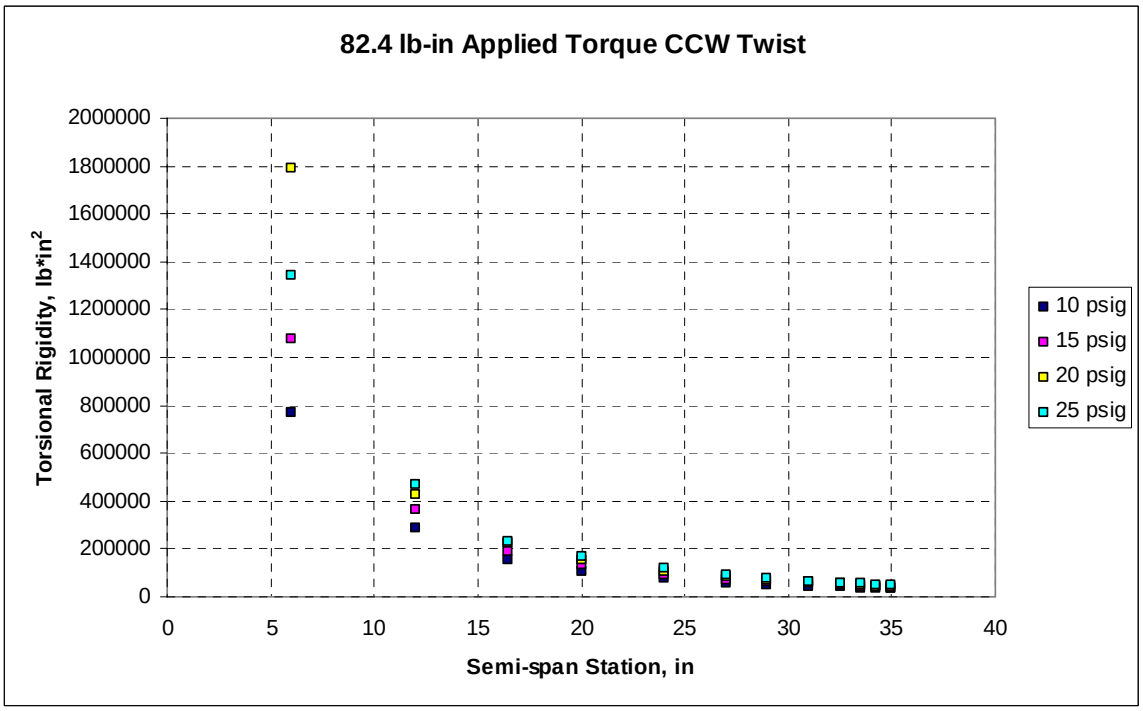

Figure 3.19 – Torsional rigidity of wing for 82.3 lb-in torque applied at wing tip.

CHAPTER 4: FINITE ELEMENT MODELING OF STATIC LOAD CASES

This chapter details the efforts of simulating static load cases on the inflatable wing and presents comparisons of these simulations to the experimental tests discussed in Chapter 3.

The process of developing the FE model of the wing began with a previous "pathfinder" model by Nathan Coulombe, defined and evaluated as part of an undergraduate independent study course. His model was constructed using shell elements with Young's modulus material properties discussed in Section 3.1 for the Urethane-coated Vectran. The pathfinder model proved too stiff when compared to experimental results. The test data discussed in Section 3.2 was sent to UK by ILC Dover, and simpler models of inflatable test cylinders were considered to determine the validity of the modeling approach.

After these models were validated through comparisons with experimental data, focus shifted back to the wing model, and correlation of the FE model to experimental static loading. Initially, a linear orthotropic material model with different Young's Moduli in the warp and fill directions was considered, with final "effective" moduli being determined by modifying the moduli values and comparing FE simulations to experimental results. This process led to the conclusion that the FE model was in general too stiff. Subsequently, the mesh density of the model was varied to first verify that the model was meshed sufficiently to reach a converged solution, and then to reduce solution time. These mesh density studies were conducted in parallel with models incorporating a nonlinear isotropic material model that more closely resembles the true stress-strain curves of the Vectran material.

It should be noted that the order of presentation throughout this chapter is not necessarily chronological. Also note that the term “model” in this section refers to the FE model, and when referring to material data models, the term “material model” will be used. All pressures are gage pressure.

4.1 FE Analysis of Shear Test Cylinders

For validation purposes, finite element models of the urethane-coated test cylinders were created using ANSYS (version 8.0). The goal here was to use these models to simulate the shear modulus tests discussed in Section 3.2. A cylindrical model was created using single-layer orthotropic shell elements (SHELL181) for the surface of the cylinder. The length of the model was 15 inches, corresponding to the distance between the two end clamps on the test stand. Nodes at the “fixed” end of the cylinder were constrained in all directions. Multipoint constraint (MPC184) elements were used to apply the load torque on the opposite end of the cylinder. Constraint elements were attached to the free end of the cylinder and to a master node (for torque application) located two inches beyond the end of the cylinder on the centerline. Also, models with both coarse and fine meshes were created. With all constraints applied, the coarse model contained 385 nodes and 2166 DOF, while the fine model contained 1861 nodes and 10,806 DOF. These finite element meshes are shown in Figure 4.1.

Two models were created, corresponding to the two test cylinders. One model had warp material properties in the longitudinal direction, and fill properties in the hoop direction, while the other model had the directions of these two material property orientations interchanged. The same basic model was used for both test cylinders, with

only the longitudinal- and hoop-direction material properties different between them. A linear orthotropic material model was used, with the properties shown in Table 4.1.

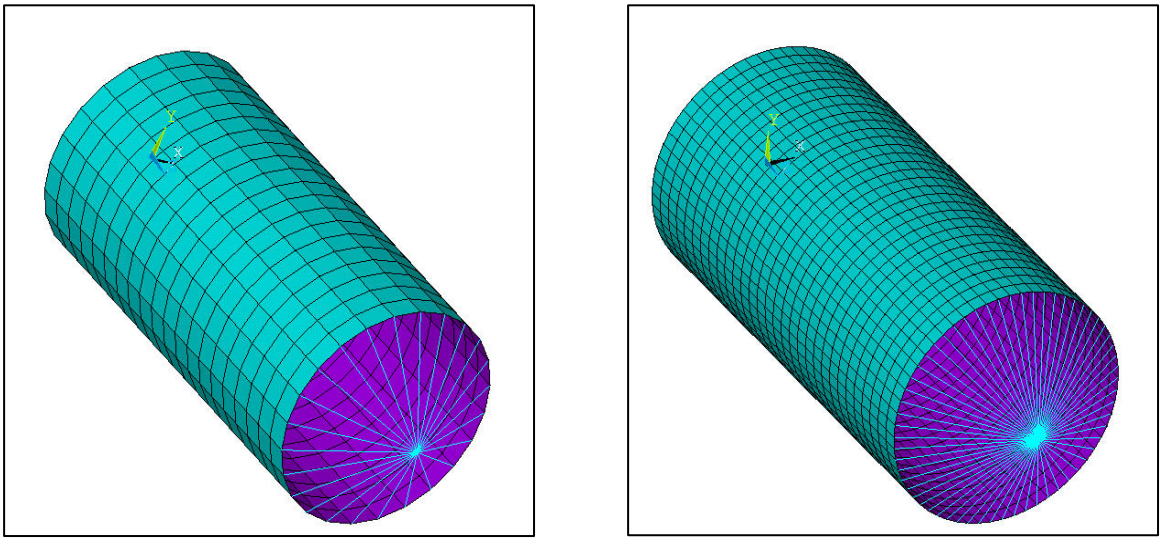

Figure 4.1 – FE model of inflatable test cylinders with coarse (left) and fine (right) meshes

Table 4.1 – Vectran material properties used in the cylinder model

Material Property	Value
Fill Modulus	1.22 Msi
Warp Modulus	1.36 Msi
Shear Modulus	Variable*
Thickness	0.013 in

**For each case, the appropriate shear modulus was used from the test data depending on the internal pressure applied to the model.*

For each case of different pressure loading, the solution process represents the experimental sequence. First, internal pressure loading was applied to the cylinder, and the nonlinear static solution was obtained. Once this solution was obtained, the appropriate torque was applied to the master node at the free end of the cylinder. The model was solved again, including the stress-stiffening effects of the pressure solution. For both solution steps, a nonlinear analysis was performed to account for large deflections and stress stiffening.

Comparisons between the results of the FE analyses and the experimental data for an internal pressure of 1 psi can be seen in Figure 4.2 and Figure 4.3. In these figures, circumferential displacement, the distance any point at the cylinder tip travels in the direction of the circumference of the cylinder, is plotted to allow for ease of comparison of experimental to FE results. These results are representative of results at higher pressures.

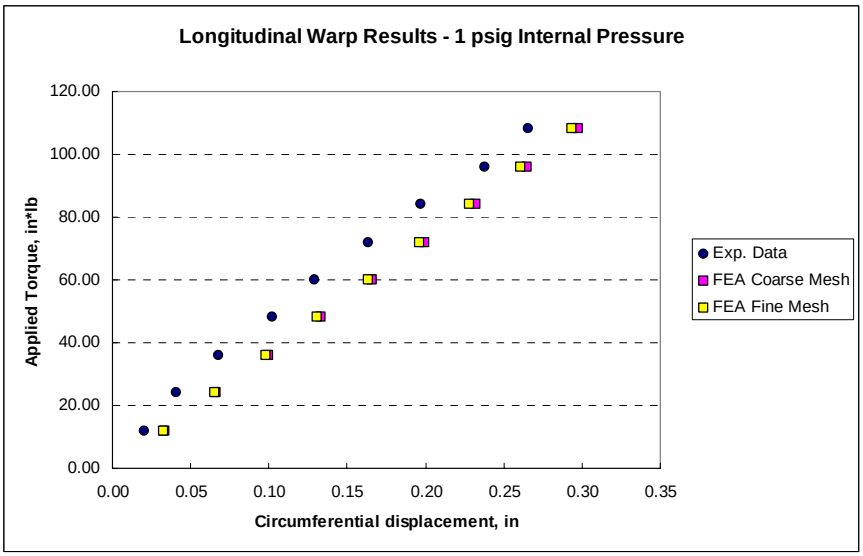

Figure 4.2 – Comparison of results from cylinder with longitudinal warp, 1 psi internal pressure

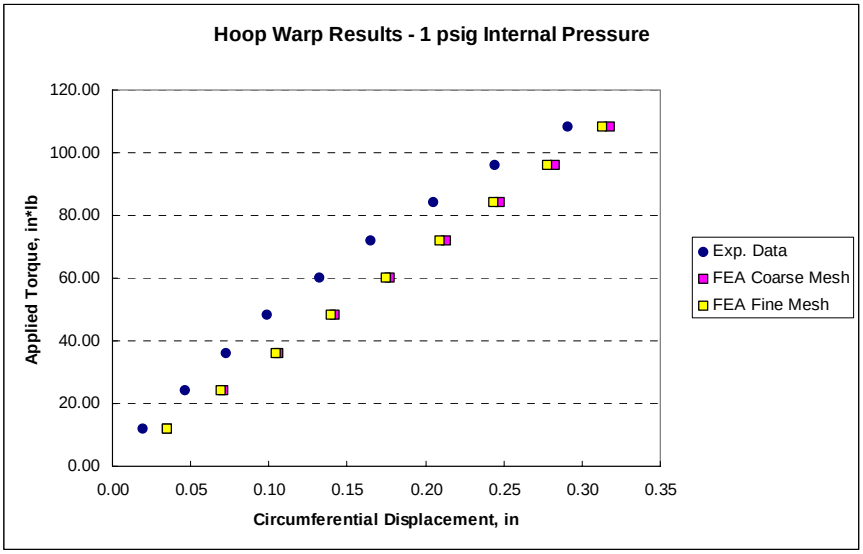

Figure 4.3 – Comparison of results from cylinder with hoop warp, 1 psi internal pressure.

There proved to be little difference between the fine and course FE model results. It was therefore determined that a course mesh would be sufficient and would reduce solution times. In both orientations, the FE model results have slopes that generally correlate to those of the plotted experimental data.

For the longitudinal warp orientation and loads greater than 30 in-lb, the FE analysis angular deflection results are greater than the experimental data by a near constant difference. Both the experimental and FE results for the longitudinal warp orientation are linear or nearly so. For the longitudinal fill (hoop warp) orientation in Figure 4.3, the experimental data shows a nonlinear softening trend, so the FE model and experimental results do not correlate as well for all load cases at this lowest pressure. A linear approximation for the moduli appears to be less accurate for fill shear modulus, as can be seen from the experimental data.

Also, the experimental data shows an initial angular deflection of the cylinder even when no torque has been applied. Initial twist was in the same direction as the loading. For the longitudinal fill cylinder, initial twist ranged from 2.2 – 5.0 degrees, and

decreased as pressure increased. For the longitudinal warp cylinder, initial twist ranged from 5.6 – 6.4 degrees, and increased as pressure increased. Initial twist in the cylinders may be due to initial twist in the cylinder during test set-up, or may possibly come from inherent properties of the weave in the Vectran. This initial twist was not present in the FE results. For comparison between experimental deflection and FE deflection, the initial twist was subtracted from the loaded twist.

Furthermore, it is important to note that when the model is loaded with pressure only, the computed radial deflection of the cylinder in all cases is much less than the radial deflection recorded experimentally. Knowing that the radial deflection of the cylinder FE models due to pressure loading did not match the radial deflection seen in the laboratory testing, various factors were applied to reduce the Young's moduli in the warp and fill directions in the FE model, until the radial deflection of the model matched the radial deflection seen in laboratory testing.

The fact that the urethane coating of the test cylinders would make the material more stiff than the silicone-coated Vectran used in the wings also motivated determination of a reduction factor to apply to the cylinder material properties to be used in the inflatable wing model. For correlation of the radial deflections, the urethane-coated Young's moduli were reduced to 25% of the values used for the initial model.

Although a few questions remain for the correlation of the cylinder model to the available data, the correlation seen in Figure 4.2 and Figure 4.3 is sufficient for use in the initial FE model of the internally pressurized Vectran wing.

4.2 FE Model of Inflatable Wings

4.2.1 FE Model Geometry

ANSYS finite element software was used to create the finite element model of the inflatable wing. The profile of the wing root was initially modeled in ProEngineer™ from cross section drawings provided by ILC Dover, shown in Figure 4.4. This profile was imported into ANSYS, and the resulting keypoint locations were recorded. These keypoint locations were then included in an ANSYS batch file (See Appendix A) to remove the step of importing a geometry file each time the model was created.

For modeling purposes, an assumption was made that each inflated section of the wing had a cross section shape composed of circular arcs for the external restraint and straight lines for the internal spars. The cross-section of the wing tapers linearly along the span from the root to the tip, so the complete geometry was created in ANSYS by scaling down the root profile to create the tip profile, then “connecting” the two profiles with areas that create the external restraint and internal spar areas. Rather than trying to reproduce the detail for the rounded seamed tip of the wing, a flat end was meshed to allow pressure forces to stiffen the restraint elements along the span-wise direction. The actual wing has a nominal semi-span of 36 in. with leading and trailing edge lengths of 35 in. For the FE model, due to the simplification of modeling a flat wing tip, the semi-span length for the wing, including both leading and trailing edges, is 36 in. The seams present in the wing were not included in the FE model. Rather, the internal spars were modeled with a rigid connection to the external restraint. The internal bladder was not included in the FE model. Because the internal volume of the bladder is larger than the

internal volume of the restraint, an assumption was made that the two layers would align and act as one, and the Vectran material properties would dominate wing response.

The geometry was then meshed as shown in Figure 4.5. ANSYS shell (SHELL181) elements were used. These are four-node elements with six degrees of freedom per node and are suitable for thin to moderately-thick shell structures [40]. An element thickness value of 0.013 in. was used, which is the nominal thickness of the Vectran fabric. As seen in Figure 4.5, the FE mesh was created such that spanwise mesh density increases toward the wing tip, with the element length at the tip being ½ the element length at the root. Spanwise elements were created using the mapped mesh option in ANSYS, while the flat wing tip area was meshed with a free mesh. As in the physical wing, the wing tip area was connected only to the external restraint and not to the internal spars. This initial model contained 17,681 elements and 16,887 nodes. All nodes at the wing root were constrained in all DOF, simulating the cantilever mount configuration. After these constraints were applied, the initial model contained 100,428 DOF.

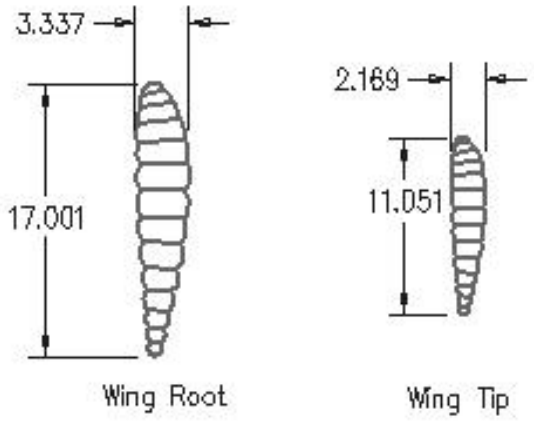

Figure 4.4 – Wing dimensions in inches

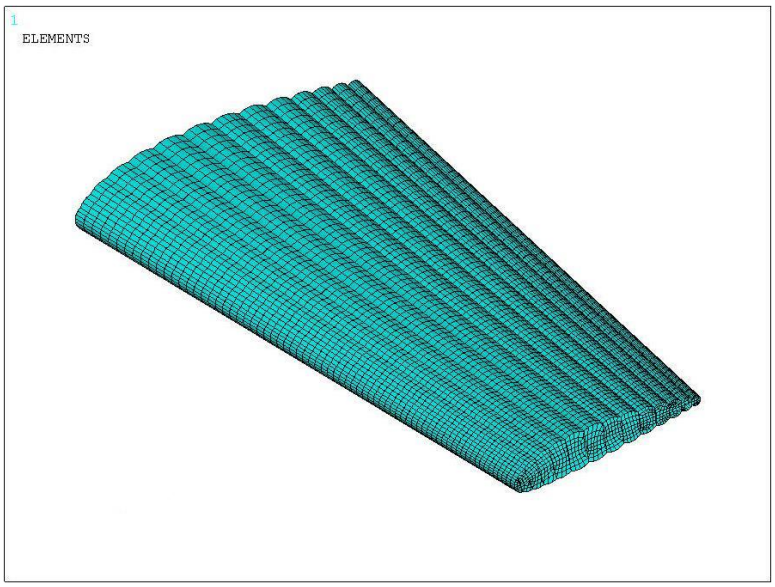

Figure 4.5 – Meshed inflatable wing model

4.2.2 Mesh Convergence

From the initial correlation comparisons, it was seen that the FE model proved stiffer than the wing. In order to confirm that the model mesh contained enough DOFs to reach a converged solution and that the mesh density was not artificially stiffening the model, a finer mesh was constructed. This fine mesh contained 139,866 DOF, a 39% increase from the 100,428 DOF in the original model. This model was solved for a loading case of 10 psi internal pressure and an upward bending tip load of 11.24 lbf (50 N). For both linear and nonlinear material models, the finer mesh showed no change in the deflection results, thus the original mesh was determined to be sufficient for obtaining static solutions.

Once it was seen that increasing the mesh density had no effect on the solution, a more coarse mesh was considered in an effort to reduce solution computation time. This coarse model contained 69,750 DOF after all constraints were applied. When this mesh was considered along with the linear material model, the solver failed to converge to a solution, even after increasing the number of solution iteration substeps. However, the nonlinear material model did converge with this coarse mesh to the same result as seen

with denser meshes. In fact, using the nonlinear material model, an even coarser mesh with only 35,538 DOF was found to converge to the same displacement solution as the 100,428 DOF mesh, resulting in greatly reduced solution times. All meshes considered can be seen in Figure 4.6.

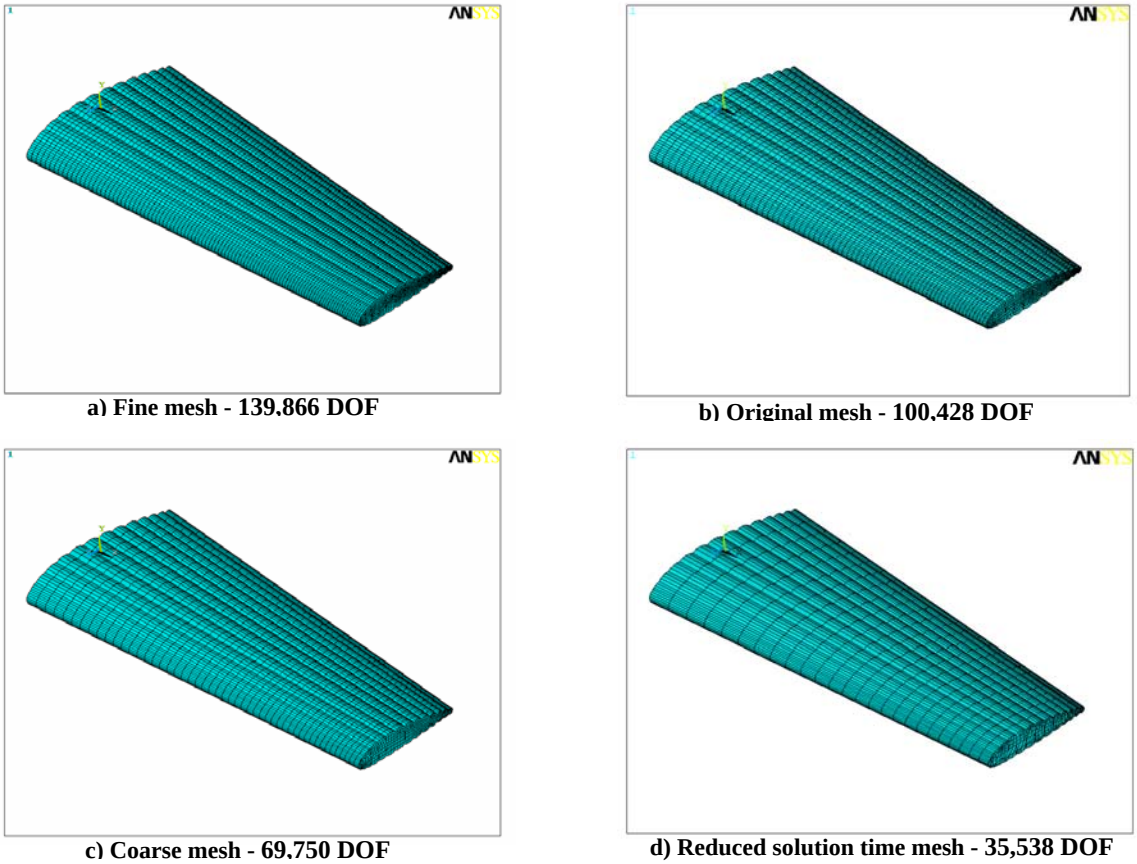

a) Fine mesh - 139,866 DOF

b) Original mesh - 100,428 DOF

c) Coarse mesh - 69,750 DOF

d) Reduced solution time mesh - 35,538 DOF

Figure 4.6 – Mesh densities

4.2.3 Material Models

Two different material models were considered during this effort. The first model incorporated a linear orthotropic material model developed using data supplied by ILC Dover. Initial material properties used are listed in Table 4.2, and correlate to testing performed on urethane-coated Vectran. Note that for the wing, the warp direction of the

fabric restraint is oriented parallel to the wing span and the fill direction is oriented parallel to the wing chord. The fabric of the internal spars is also oriented with the warp direction parallel to the wing span. At the time of initial model creation, the urethane coating material properties were the only data available, though it was later determined that the wings were actually constructed of silicone-coated Vectran, and that the different coatings can have a large effect on the material properties. Using the urethane material properties, the model initially proved too stiff, and effective moduli were determined through FE bending load simulations. This process, including determination of effective moduli, is discussed in detail in Section 4.3.1.1.

Table 4.2 – Initial material properties used in FE model

Material Property	Value
Fill Modulus	1.22e3 ksi
Warp Modulus	1.36e3 ksi
Shear Modulus	200 ksi

Upon revisiting the tensile test data of the Vectran material, it was seen that the full stress-strain curves for the warp and fill directions of the fabric are nonlinear, so a second material model was developed for use in the FE model. Figure 4.7 shows the full stress strain curves obtained from tensile testing, with five strips of Vectran being tested in each of the warp and fill directions. Because the stress-strain curves in Figure 4.7 are similar (neglecting outlier fill sample 1), the nonlinear isotropic material model shown in Figure 4.8 was developed for use in the FE model. The multilinear curve shown was used to allow for ease of input into the FE model.

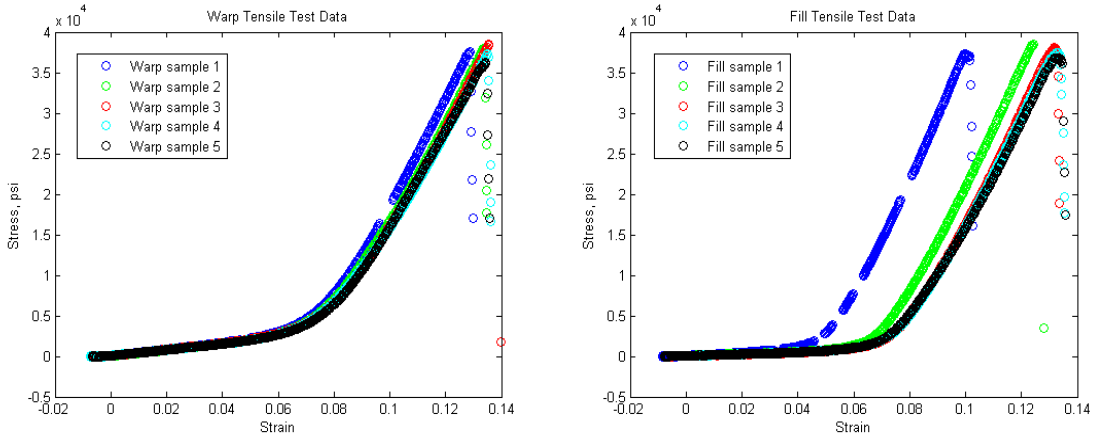

Figure 4.7 – Tensile test stress-strain diagrams for both material directions.

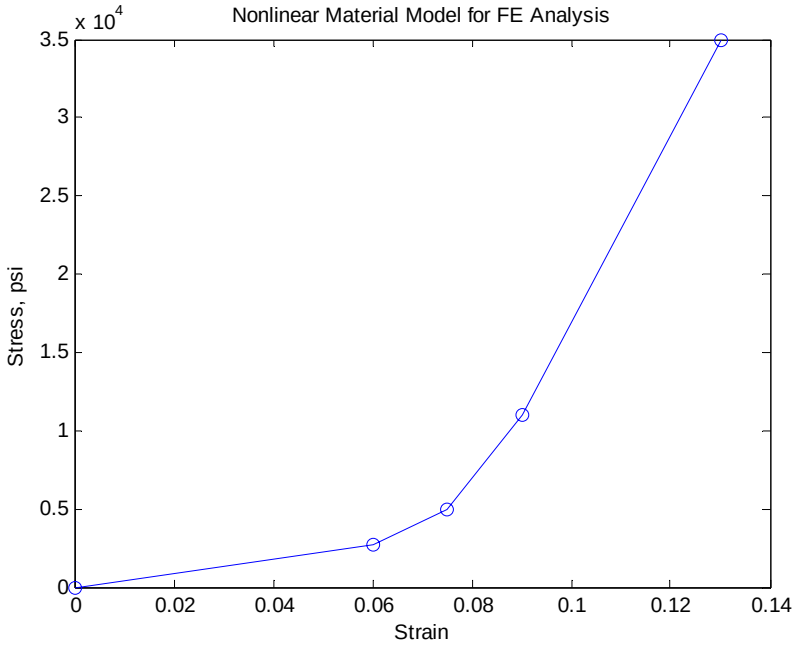

Figure 4.8 – Material model used in the FE model.

4.2.4 Application of Loads

The model solution process consisted of two steps. First, before applying external loads to the wing model, internal pressure was applied. All nodes at the wing root were constrained in all DOF, and pressure loading was applied outward to the elements

comprising the external surfaces to simulate the pressurization of the wings. This includes the wing tip area. Initially, four different cases were to be considered: 10, 15, 20 and 25 psi. The Newton-Raphson nonlinear solver was used to compute static response to account for large deflections and stress stiffening. For pressures higher than 15 psi, this pressure solution failed to converge, even after increasing the number of iteration substeps used.

Once the internal pressure loading solution was obtained, external loadings were applied and subsequent solutions were computed, for both external bending loads and external twisting loads.

4.3 FE Simulations of Static Loads

4.3.1 Wing Bending

After the initial pressurization analysis converged, an upward vertical force was applied at the node corresponding to the location of the applied force in the experimental bending test, and vertical deflection results were obtained at nodes corresponding to measurement locations from the experimental bending test. Application of the internal pressure loading caused initial deflections to the wing, and these positions were subtracted from the final loading deflections to determine the calculated displacements for comparison to experimental results.

4.3.1.1 Linear Orthotropic Material Model

In Figure 4.9, applied load vs. vertical deflection is plotted for an internal pressure of 10 psi. Data from two experimental tests was available for initial comparisons. Due to the lengthy solution time of each FE analysis, in the following sequence, material properties were adjusted to obtain correlation of the model for the lowest wing tip loading case

before the model solution was computed for higher tip loadings. The initial finite element model used a linear orthotropic material model, with urethane-coated warp and fill moduli and shear modulus as determined from experimental testing. Loads were applied, and this model did not converge to a solution. The large difference between E = 1.36e3 ksi and G = 15 ksi was thought to be a problem, so a temporary shear modulus of G = 200 ksi was used in the FE model to achieve initial convergence. This adjusted shear model proved to be more stiff than the wing was seen to be through experimental testing, so a reduction factor was applied to the material properties to obtain “effective” moduli for the model. Because the Young’s moduli would affect the stiffness of the wing in bending more than the shear modulus, the Young’s moduli were reduced while shear modulus was initially kept constant at 200 ksi.

Results of various modulus factors are also shown in Figure 4.9 for 10 psi internal wing pressure and 2.25 lbf loading, highlighted in the plot. It was found that a value of 25% of the original Young’s modulus still proved too stiff, while 5% was too soft. Correlation to experimental results was achieved for this load case with a modulus reduced to 8% of the urethane test value. After results matched well for this case, the model solution was computed for higher tip loadings using the same 8% reduced modulus. Finally, with converging solutions at this lower Young’s moduli, the shear modulus was reduced from 200 ksi to 20 ksi, much closer to the value found from material testing. However, as can be seen in Figure 4.9, this change had only a minimal effect on the final calculated deflections. In examining Figure 4.9 it can be seen that for an internal wing pressure of 10 psi, FE and experimental results matched well only for tip loadings below 4.5 lbf and diverged significantly after that.

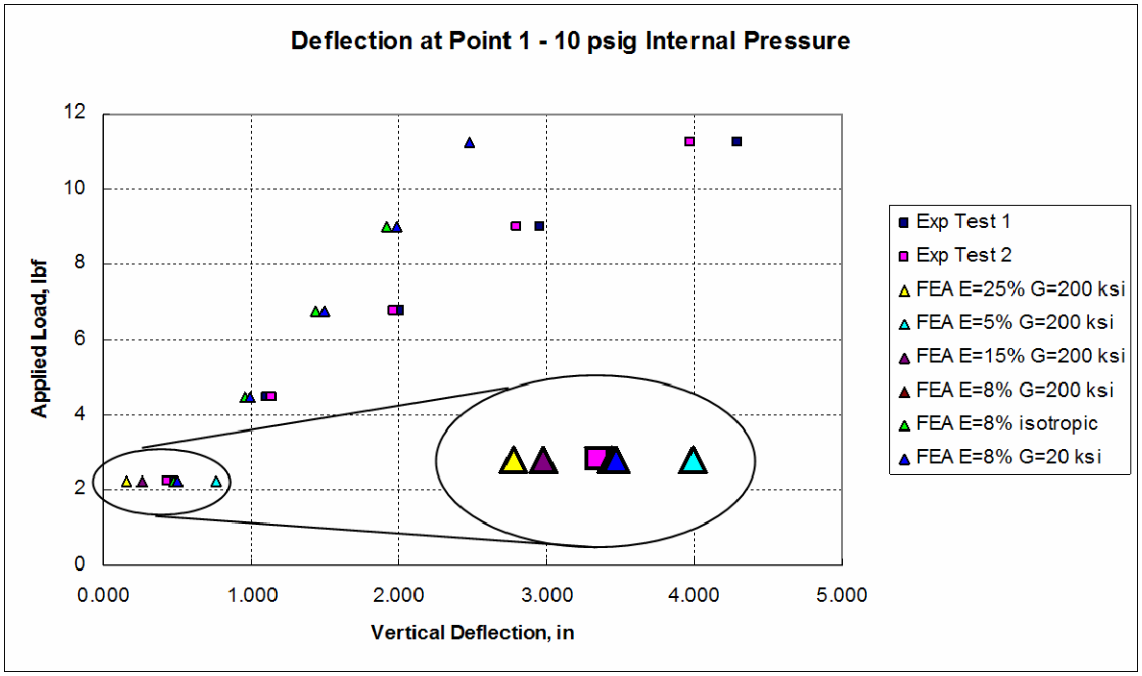

Figure 4.9 – Comparison of experimental and FE wing deflection results

In Figure 4.10, results for bending deflections of a wing with internal pressure 15 psi are shown. It is seen that for this case, FE results actually match well with experimental results. However, it should be noted that FE results for 10 psi and 15 psi are nearly equivalent. Thus, it is seen that the bending stiffness of the wing model does not increase with pressure as the actual wing does. A shear modulus of 50 ksi was used for the 15 psi case to enable convergence of the solution, but as noted previously, varying the shear modulus has only a minimal effect on the deflection results. Also, higher pressures of 20 and 25 psi did not converge to a solution, even after using larger shear modulus values and applying a higher number of solution iterations. However, it should be noted that wing warping strategies being investigated are most effective at lower wing inflation pressures, so modeling capability in this achievable pressure range is preferred for research on this topic.

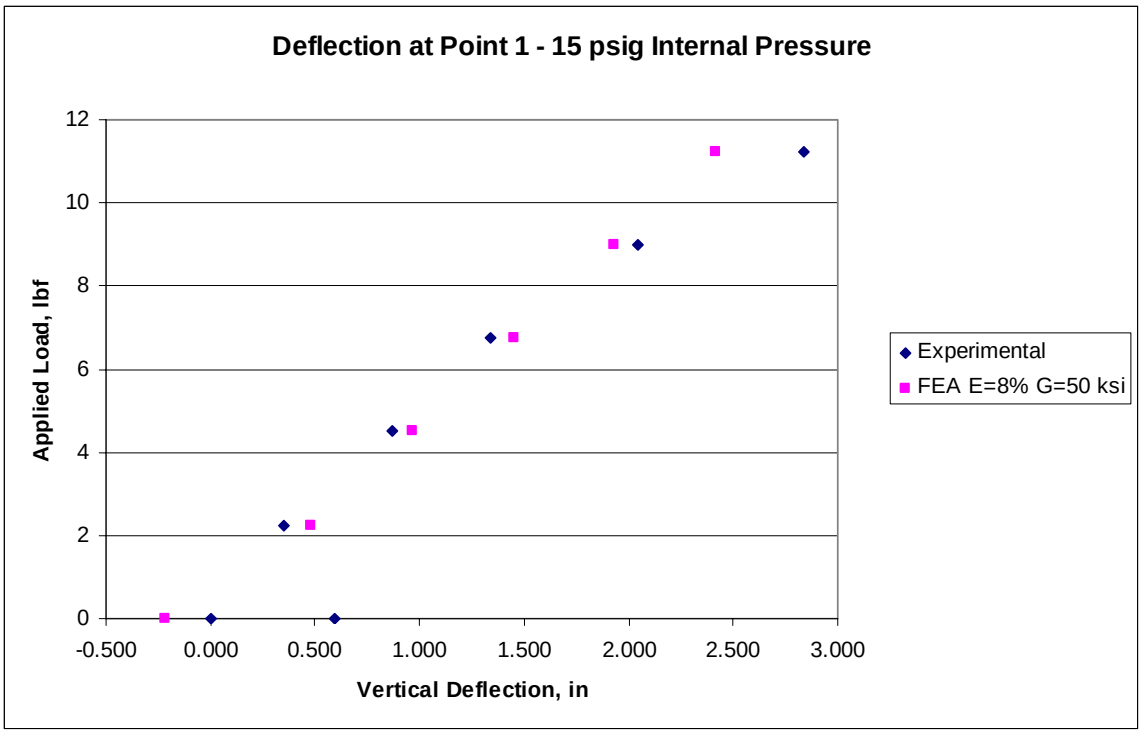

Figure 4.10 – Comparison of experimental and FE wing deflection results.

Although results were mixed for correlation of the FE model of the inflated wing to experimental results, important characteristics were accurately modeled. For example, Figure 4.11 is the resulting deflected shape with 15 psi inflation pressure and 11.2 lbf tip force. As expected, the maximum deflection occurs at the tip with a characteristic beam-bending profile along the span. As with the experiment, no twisting is seen in the deflected result.

Note also that at the time of the initial modeling effort, only urethane-coated Vectran moduli were available, so a reduced modulus was determined for the wing. After this was completed, Young's moduli for the silicone-coated material became available and were seen to be 20% of that of the urethane-coated material. The reduced moduli determined through the validation effort ranged from 5% – 25% of the urethane-coated moduli, with 8% providing the best correlation for 10 psi internal pressure and 2.25 tip loading.

Therefore, correlation of the model and experiment yielded material properties consistent with those for the correct coating.

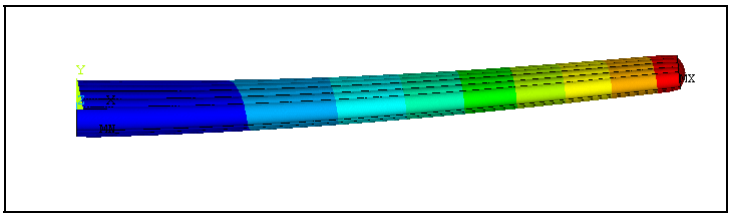

Figure 4.11 – Deflected wing shape for 15-psi pressurization and 11.2-lbf tip load.

4.3.1.2 Nonlinear Isotropic Material Model

The nonlinear material model described earlier in Section 4.2.3 was incorporated into the FE model using the hyperelastic material option in ANSYS. Comparison of bending deflections due to applied tip loadings using the nonlinear material model and experimental results for an internal pressure of 10 psi are shown in Figure 4.12. From Figure 4.12, it is seen that this nonlinear material model resulted in a model that was again stiffer than the wing was seen to be during experimental testing, and is in fact stiffer than the previous model using a linear orthotropic material model. When linear fit lines for both data sets are compared, the nonlinear material model is 67% stiffer. Note that the experimental test data plotted here is from the original wing bending test, not the revised test discussed in Section 3.4.

The nonlinear material model resulted in a stiffer FE model than the linear orthotropic model, but this nonlinear material model has not been adjusted from material testing, while the linear orthotropic model presented uses “effective” modulus properties that are much reduced from that corresponding to experimental data. As such, the next step in the process was to consider an “effective” nonlinear material model. First, the slope of each linear segment of the nonlinear material model was decreased to 75% of the original, and

10 psi internal pressure and bending loads were simulated. To reduce solution processing time, the coarse FE mesh containing 69,750 DOF was used for these analyses. The reduced solution time 35,538 DOF mesh failed to converge to a solution when this adjusted material model was used. The results for this material model are also plotted in Figure 4.12. From this plot it can be seen that this material model more closely models the response of the wing compared with the original nonlinear material model, but still proves 18% stiffer than the linear orthotropic model over the range of pressures considered. However, this difference in the adjusted and original nonlinear models is less than the difference between the original and "effective" linear material models, so the nonlinear model more closely correlates to what was seen during material testing.

Figure 4.13 shows a comparison of bending deflections due to applied tip loadings using the nonlinear material model and experimental results for an internal pressure of 15 psi. Of important note for this pressure case is that the modified nonlinear material model resulted in a FE model that actually deflected farther than the wing deflected experimentally, and in fact deflected farther than the FE model under 10 psi internal pressure. It should be noted that the 10 psi cases were computed using a coarser mesh than the 15 psi case because the 15 psi case failed to converge to a solution using a mesh coarser than the original mesh. Initially, this was thought to be the cause of the modified material model causing these larger deflections. However, when the 10 psi case was re-computed with the original mesh, the results did not change, so the mesh density is not the reason for this softening effect in the 15 psi case. With this result, no further adjustment of the nonlinear material model was considered.

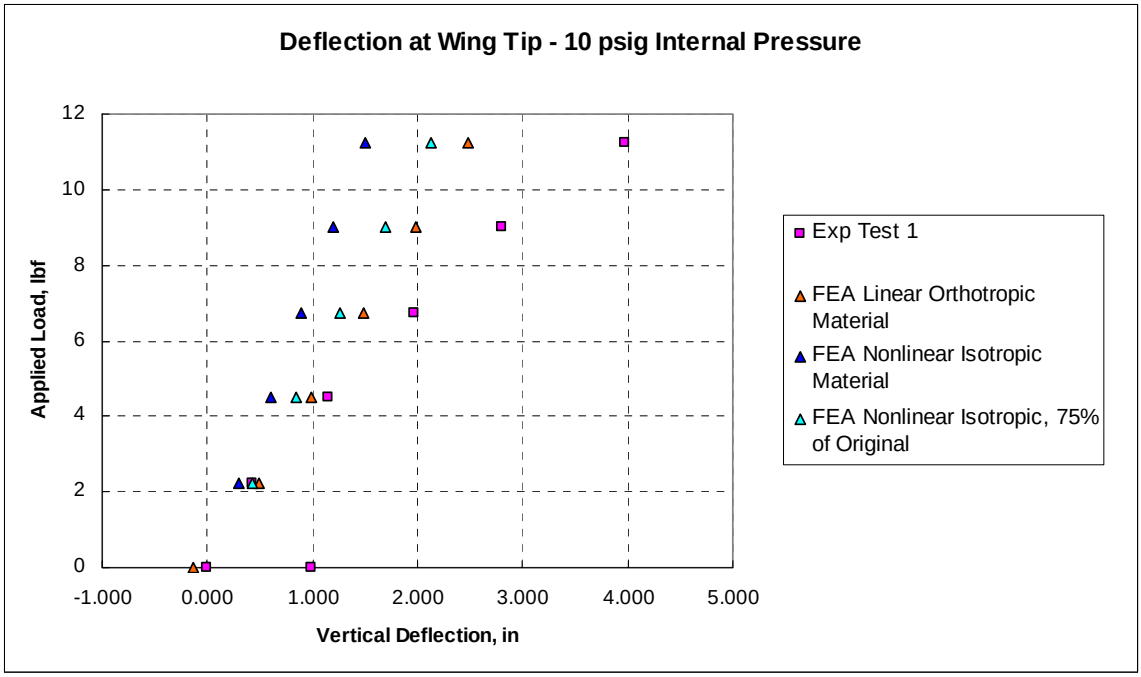

Figure 4.12 – Comparison of experimental and FE wing bending results for 10 psi, deflection at wing tip shown.

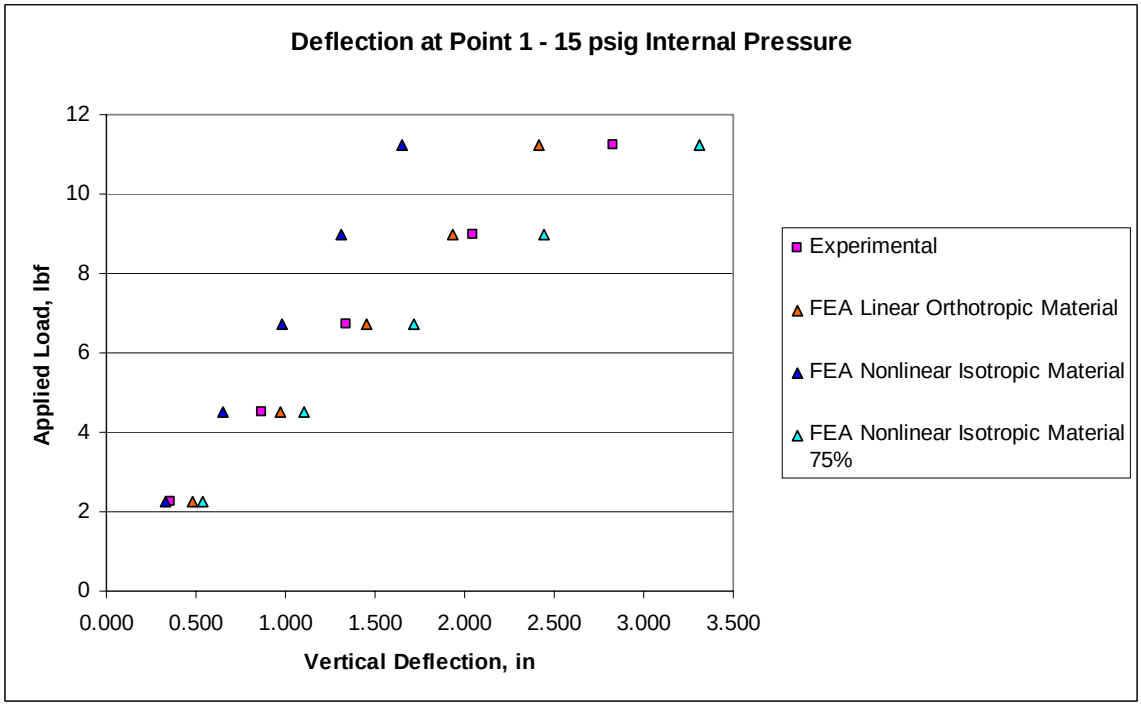

Figure 4.13 – Comparison of experimental and FE wing bending results for 15 psi, deflection at wing tip shown

4.3.2 Wing Twist

Starting with the correlated wing models from the previous section, computed FE model deflections were compared to experimental results for torsion loading. Similarly to the case of modeling wing bending, the process of modeling an inflatable wing under a wing tip torsion load began with applying internal pressure to the FE model. After the internal pressure loading converged to a solution, vertical loads were applied to nodes at the leading and trailing edges of the FE model in opposite vertical directions to create the torsion load applied in laboratory testing. Vertical forces of 2.52, 4.77, and 7.01 lbf were analyzed in separate cases. Vertical deflection results were obtained for nodes along the leading and trailing edges of the FE model, at semi-span stations corresponding to measurement points from the experimental torsion test.

4.3.2.1 Linear Orthotropic Material Model

Figure 4.14 shows a comparison between experimental measurements and FE predictions of the angle of twist at the wing tip due to an applied torque Both 10 psi and 15 psi results are included, for both experimental data and FE results. The angle of twist was computed using the calculated deflections of the leading and trailing edge points. The results show that the inflatable wing FE model is also too stiff in torsion. While for the wing bending case, at 15 psi internal pressure, FE and experimental models correlated well, this is not the case for torsion loading at the same internal pressure. FE models of both 10 and 15 psi cases were found to deflect much less than expected from experimental testing. For 10 psi internal pressure, computed angle of twist at the wing tip was on average only 16% of experimentally determined angle of twist. For 15 psi, computed results on average were 29% of experimental.

While the deflection magnitudes from the FE analysis are less than those seen in the experimental testing of the wing, the deformed plot in Figure 4.15 shows that the FE model deflected shape does generally match the deflected shape seen in laboratory testing. Most notably, it can be seen in Figure 4.15 that the trailing edge deflects more than the leading edge, which, can clearly be seen from Figure 3.14 to be the case for the actual wing under load as well.

The same material model and material properties used in the FE model for the bending test were used for the torsion loading case, with one exception: when a positive (trailing edge upward, leading edge downward) torsion load was applied to the wing, at 10 psi, using a shear modulus of 20 ksi, the model failed to converge to a solution. As such, the shear modulus was increased to 50 ksi for this loading case. Just as for the wing bending case, internal pressures higher than 15 psi failed to converge to a solution.

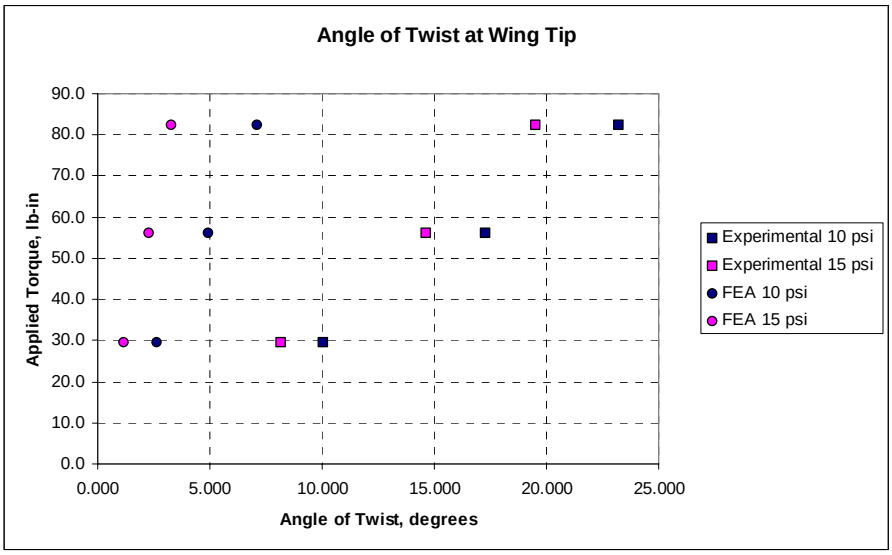

Figure 4.14 – Comparison of angle of twist at wing tip, negative twist applied.

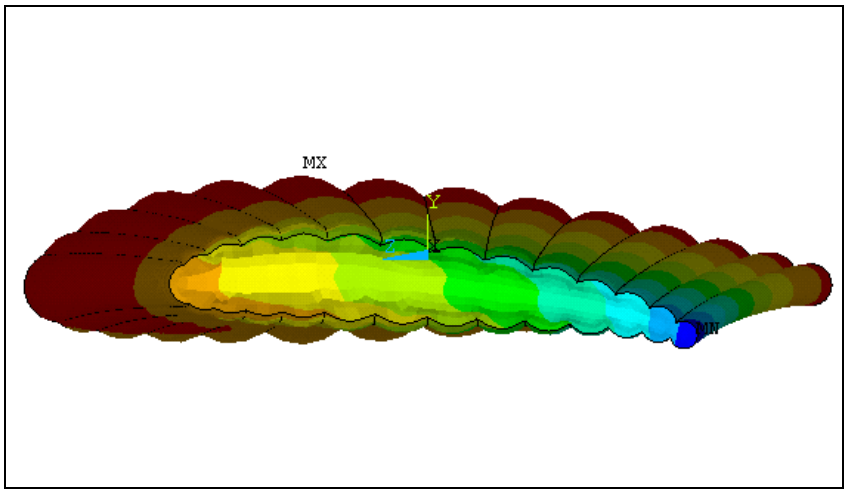

Figure 4.15 – Deflected wing shape for 15-psi pressurization and 82.4-lb-in tip load.
**results scaled X 2 for clarity.*

4.3.2.2 Nonlinear Isotropic Material Model

Torque loadings were also modeled using the two nonlinear isotropic models. Figure 4.16 shows the resulting angle of twist at the wing tip due to applied torques of 29.6 and 82.4 lb-in, at a wing inflation pressure of 10 psi. Similarly to the bending cases, the linear orthotropic model most closely estimates the experimental results, and the adjusted nonlinear isotropic model is more accurate than the original nonlinear isotropic model.

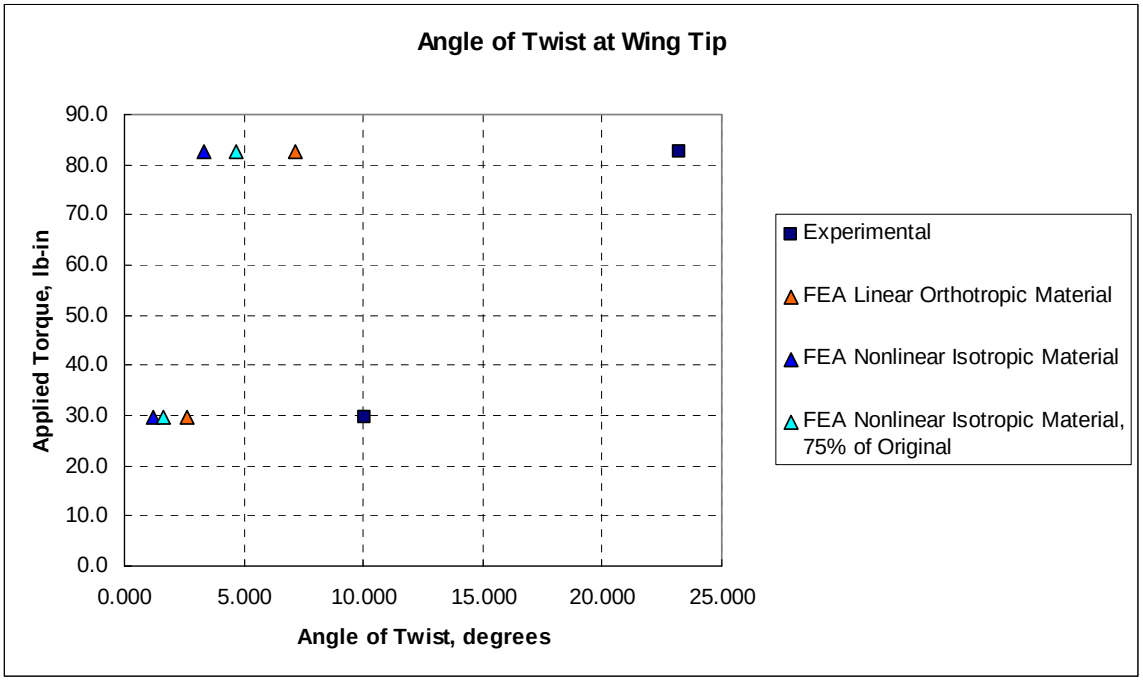

Figure 4.16 – Comparison of experimental and FE angle of twist at wing tip due to applied torques

4.4 Simulation of Wing Warping

One objective of this effort is to develop a model which can be used to evaluate wing warping actuation designs. Figure 2.8 shows an example of a wing warping technique applied to a low pressure inflatable wing. One or more servos are mounted to the wing in a manner to actuate motion of the trailing edge. Warping designs and associated wind tunnel studies are included in the research conducted by Simpson [29]. Rather than applying a moment to an aileron for roll control, the moment is applied directly to the wing, changing the wing profile as seen in Figure 2.8. Inspired by this method of wing warping, the FE model was used to simulate wing response to moment loadings applied by multiple servos along the span of the wing.

For this simulation, the reduced solution time mesh containing 35,538 DOF was used in order to keep solution computation time to a minimum. The nonlinear isotropic

material model was used. As in previous simulations, two load steps were considered, the first step was two apply internal pressure, and the second step was to apply the moment loadings. Figure 4.17 presents the locations of the applied moments. Note that area normals for the elements are reversed here only for ease of visualization, and in the analysis, the element area normals were oriented similarly to the other elements on the wing. Each “patch” area contains 30 elements, and 48 nodes. Moments of 8 lb-in were applied to the areas by applying moments of 0.167 lb-in to each node.

The load patterns considered are listed in Table 4.3. Moments are applied in the global X-direction, with the global X-axis being perpendicular to the wing cross section with positive orientation being the direction from the wing root toward the wing tip. As such, a negative moment acts as a servo “pulling” the trailing edge downward similar to the deformation shown in Figure 2.8, while a positive moment acts as a servo “pushing” the trailing edge upward.

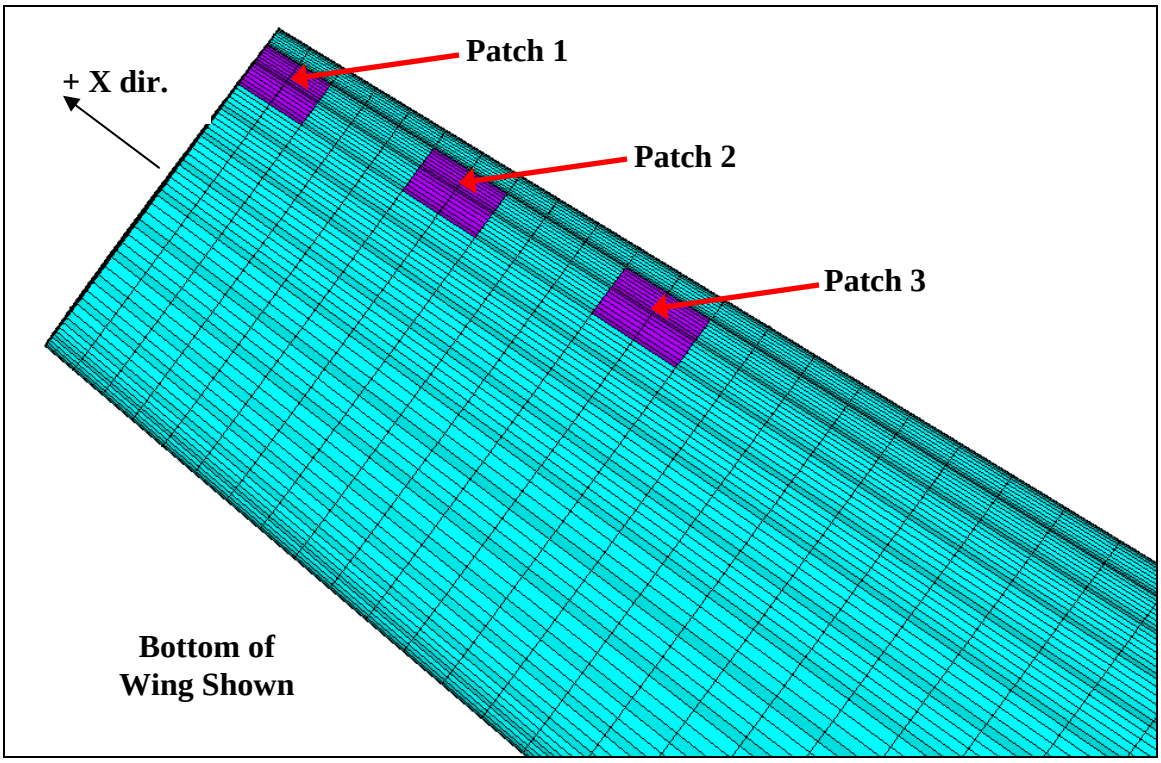

Figure 4.17 – Locations of applied moments on underside of wing

Table 4.3 – Loadings applied for each wing warping analysis

Analysis	Patch 1	Patch 2	Patch 3
1	- 8 lb-in	0	0
2	- 8 lb-in	- 8 lb-in	0
3	- 8 lb-in	- 8 lb-in	- 8 lb-in
4	+ 8 lb-in	+ 8 lb-in	+ 8 lb-in
5	- 8 lb-in	+ 8 lb-in	- 8 lb-in

The analyses are intended as a qualitative demonstration of how the wing model can be used to predict response to warping forces. Further modification of the model is needed to accurately predict wing deflections, as the model as is proves too stiff in response to static loads. Figure 4.18 shows the resulting deflected shape of the wing from a negative moment applied at Patch 1 only. As expected, the resulting shape shows the wing tip trailing edge deflecting downward, much like the example in Figure 2.8. The

results shown here have been scaled up by 5X to effectively show the deflection at the trailing edge, due to the over-stiffness of the model and the relative scale of the deflection with respect to the overall dimensions of the wing. Figure 4.19 shows the resulting deflection of the wing with negative moments applied at Patch 1 and Patch 2, while Figure 4.20 shows the same for negative moments applied at all three Patches. The resulting deflection at the wing tip trailing edge is plotted vs. the number of servos considered in Figure 4.21.

Resulting wing deflection from Analysis 4, with positive moments applied at all three Patch locations, is shown in Figure 4.22.

Figure 4.23 shows the deflected wing trailing edge shape resulting from Analysis 5 with negative moments applied at Patches 1 and 3 and a positive moment applied at Patch 2. Note the curvature of the trailing edge that can be obtained by using three servos to apply loadings to the wing simultaneously.

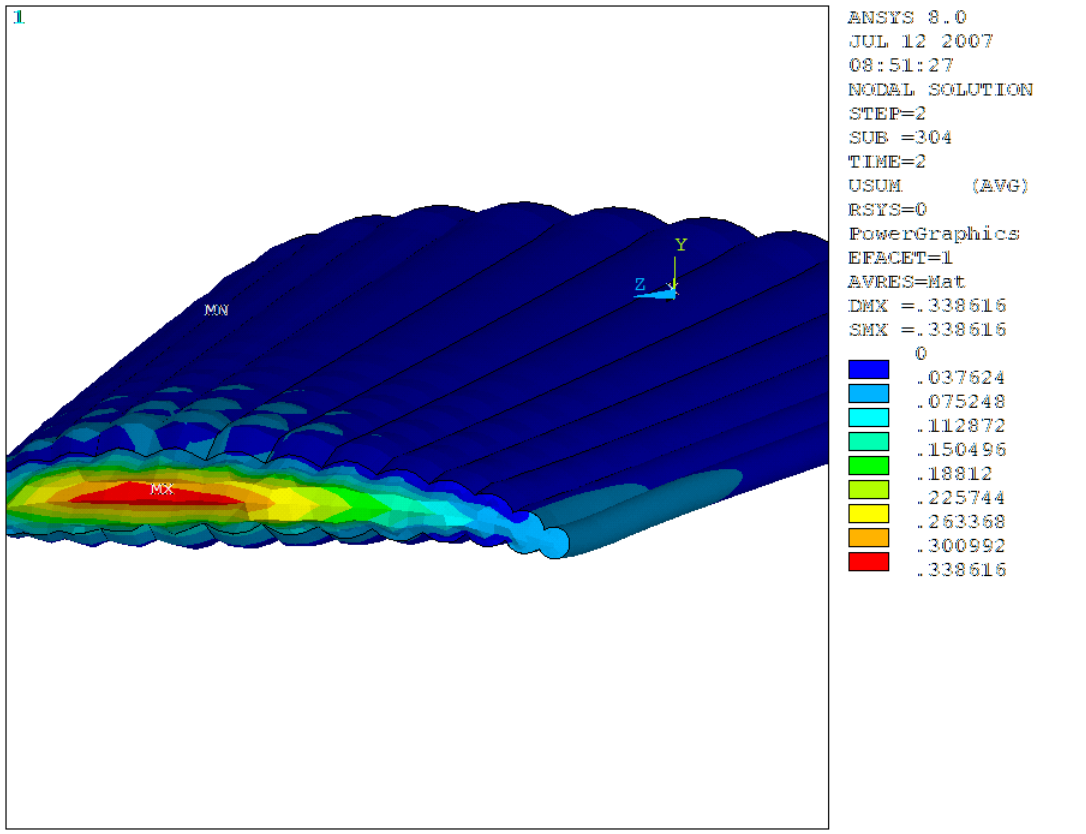

Figure 4.18 – Analysis 1 resulting deflections. Scale increased by 5X.

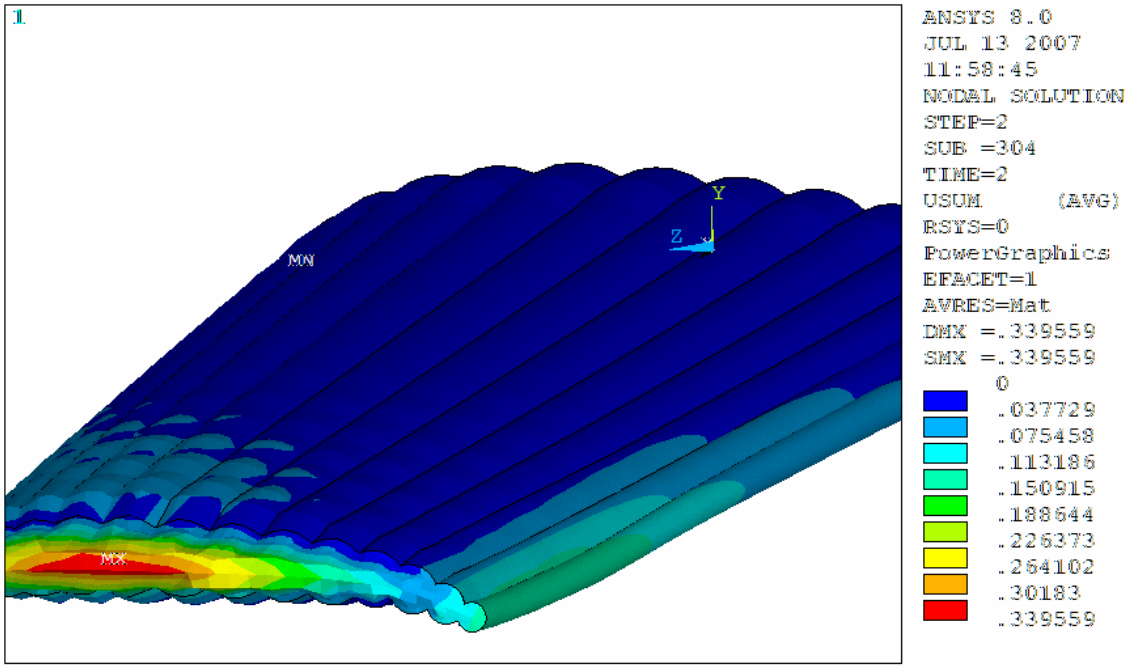

Figure 4.19 – Analysis 2 resulting deflections. Scale increased by 5X.

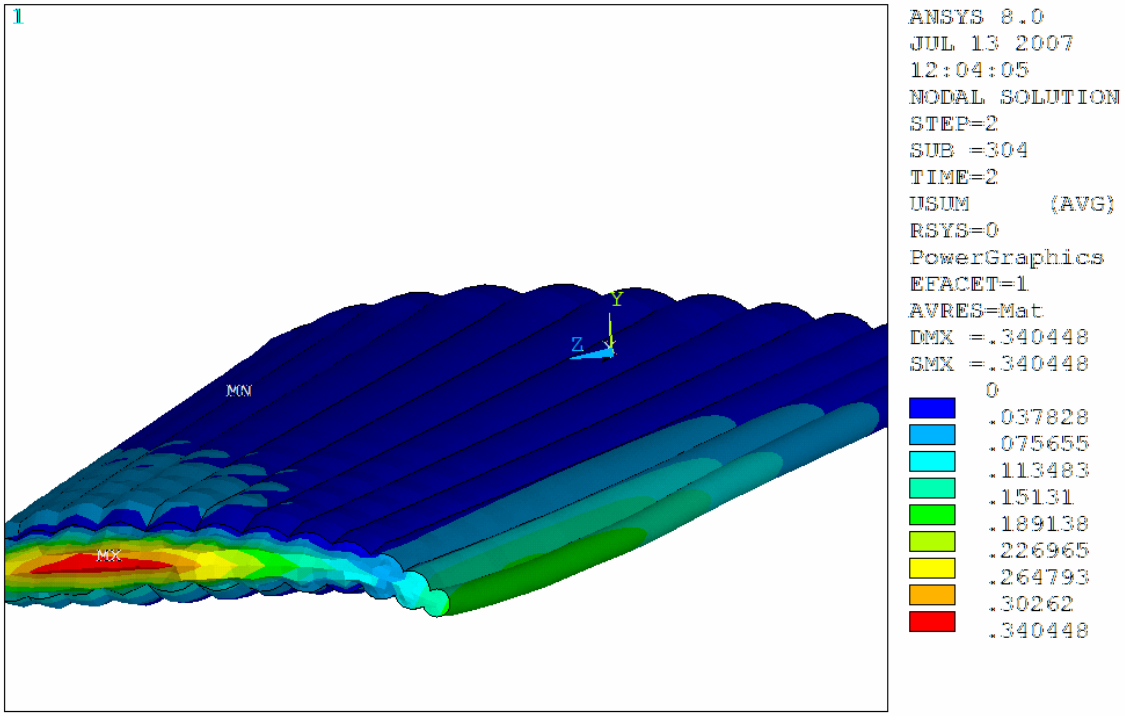

Figure 4.20 – Analysis 3 resulting deflections. Scale increased by 5X.

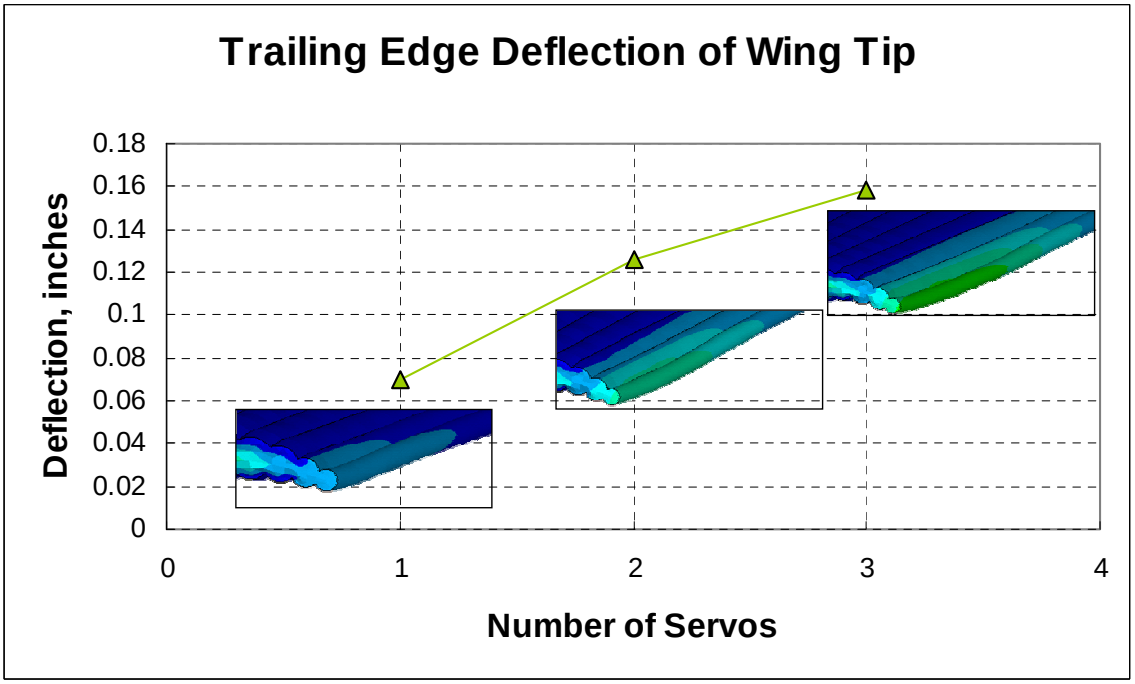

Figure 4.21 – Predicted wing deflections vs. number of servos

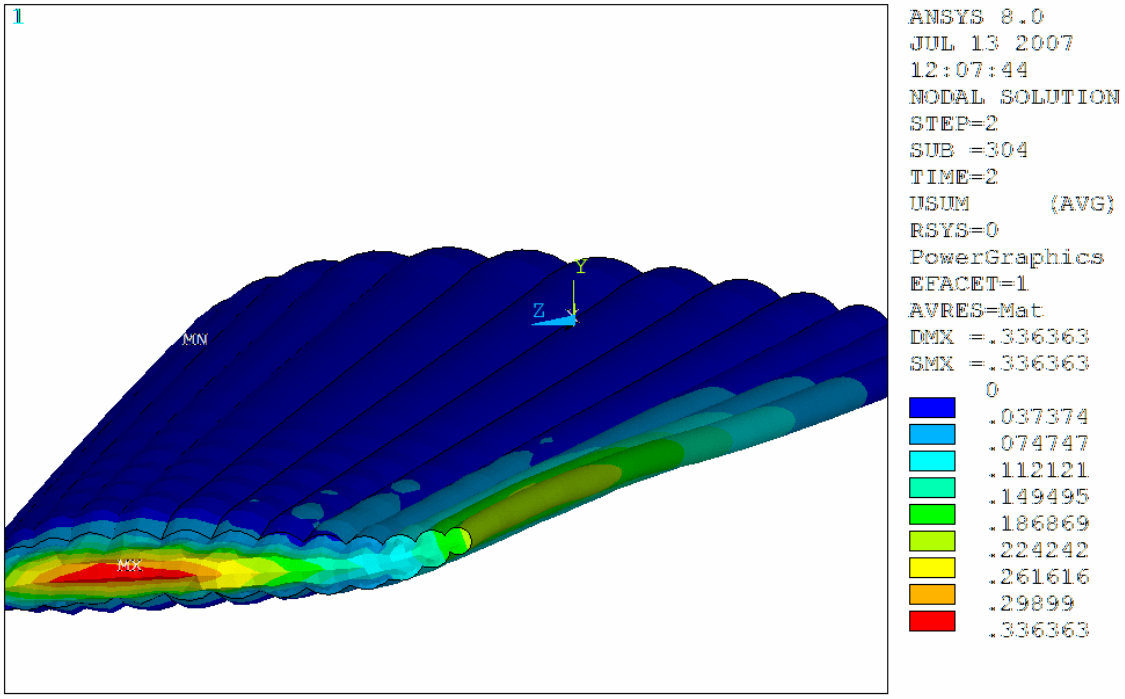

Figure 4.22 – Analysis 4 resulting deflections. Scale increased by 5X.

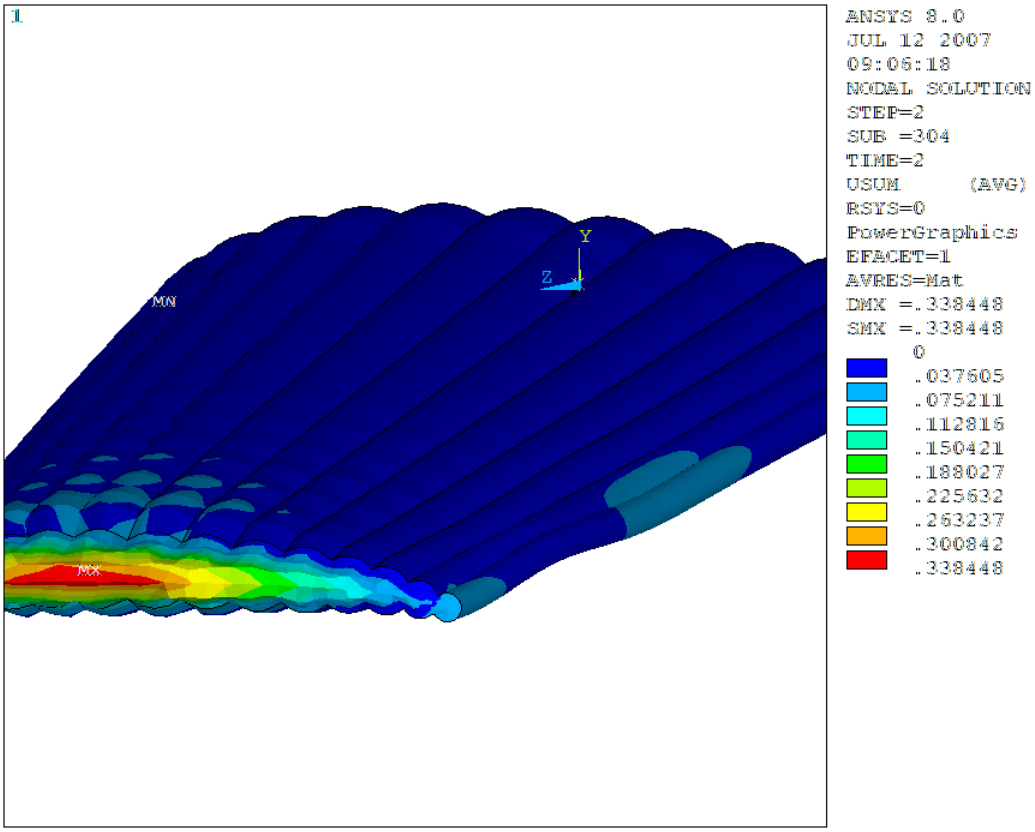

Figure 4.23 – Analysis 5 resulting deflections. Scale increased by 5X.

CHAPTER 5: EXPERIMENTAL AND FE MODAL ANALYSES

As inflatable wings do not have any rigid structural components, internal pressure is required to maintain the airfoil profile. Thus, aeroelasticity of inflatable wings is of great interest due to the wings flexibility. A major research area in the field of aeroelasticity is flutter. Aeroplane Monthly defines flutter as "…the unstable oscillation caused by interaction between aerodynamic forces, elastic reactions in the structure and the force of inertia [41]." Flutter has the potential to increase without bounds given the right conditions. In order to create a model that can be used to investigate these aeroelastic phenomena the wing finite element model was adapted and vibrational testing was conducted on the inflatable wings for model validation of structural dynamic response.

In this chapter, a verified finite element method modal analysis of an inflatable wing is presented, beginning with experimental determination of vibrational characteristics of the wing. Additionally, a discussion of the finite element model and solution processes is presented, including both linear and non-linear applications of internal pressure loadings. Finally, finite element results are compared to results of the experimental testing to evaluate the model.

5.1 Experimental Modal Analysis

5.1.1 Test Setup

Even though the test article is a unique structural system, a standard experimental modal analysis was conducted at first to determine if alternate testing approaches would be required. A schematic of the test set-up is shown in Figure 5.1. A series of cantilevered modal tests were performed to determine the vibrational characteristics of

the inflated wing under various internal pressures. The wing semi-span was mounted at the root to a rigid test stand as shown in Figure 5.2. Small, lightweight uniaxial accelerometers were secured to the Vectran restraint surface with silicone rubber adhesive. These were located at the wing tip at two locations as shown in Figure 5.2: 1) near the mid-chord of the wing and 2) near the trailing edge. These accelerometer locations were chosen so that both bending and torsional vibrations could be recorded. Impulse excitation was used for the modal testing by striking the wing with an impact hammer. Inputs were applied at 10 locations on the wing as indicated in Figure 5.3, including at the locations of the two accelerometers for driving-point measurements. The test was repeated at wing pressures of 5, 10, 15, 20, and 25 psig.

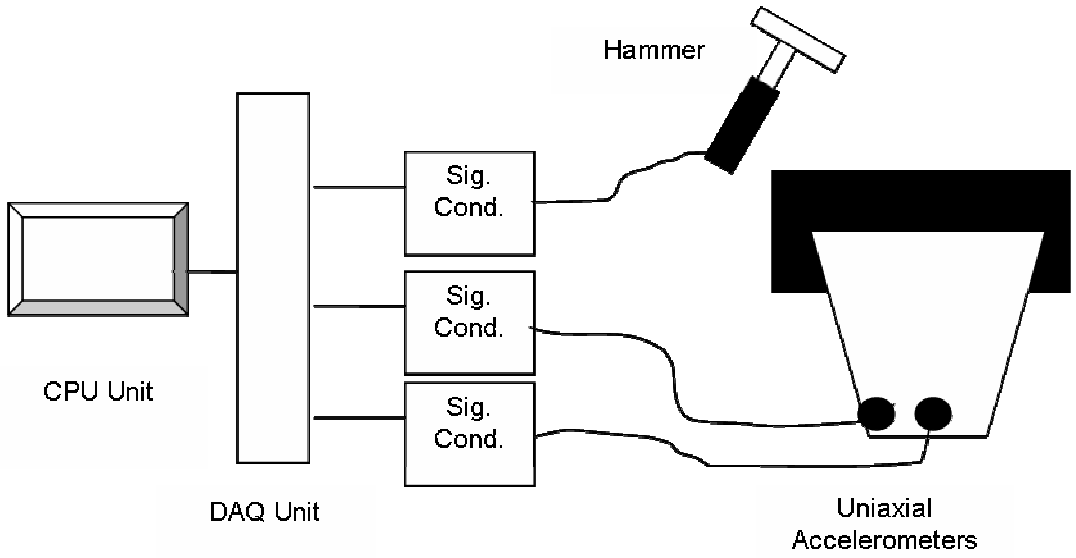

Figure 5.1 – Block diagram of experimental test setup

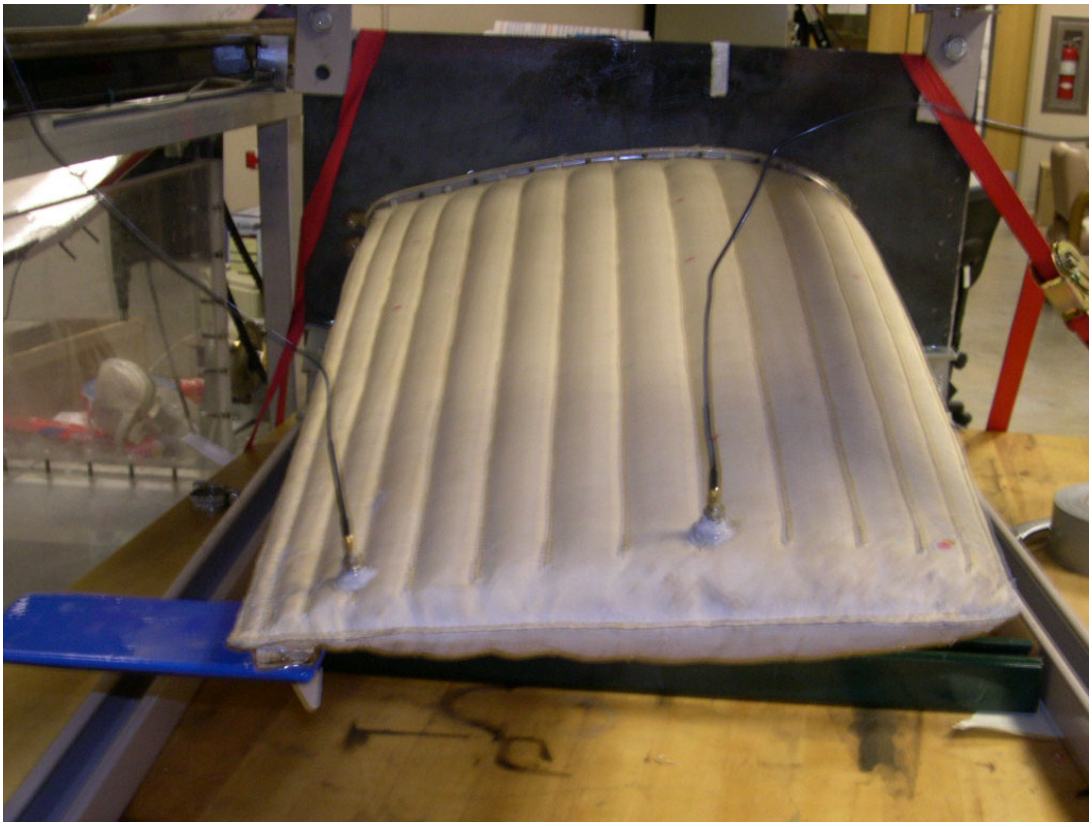

Figure 5.2 – Photo of test setup showing placement of accelerometers

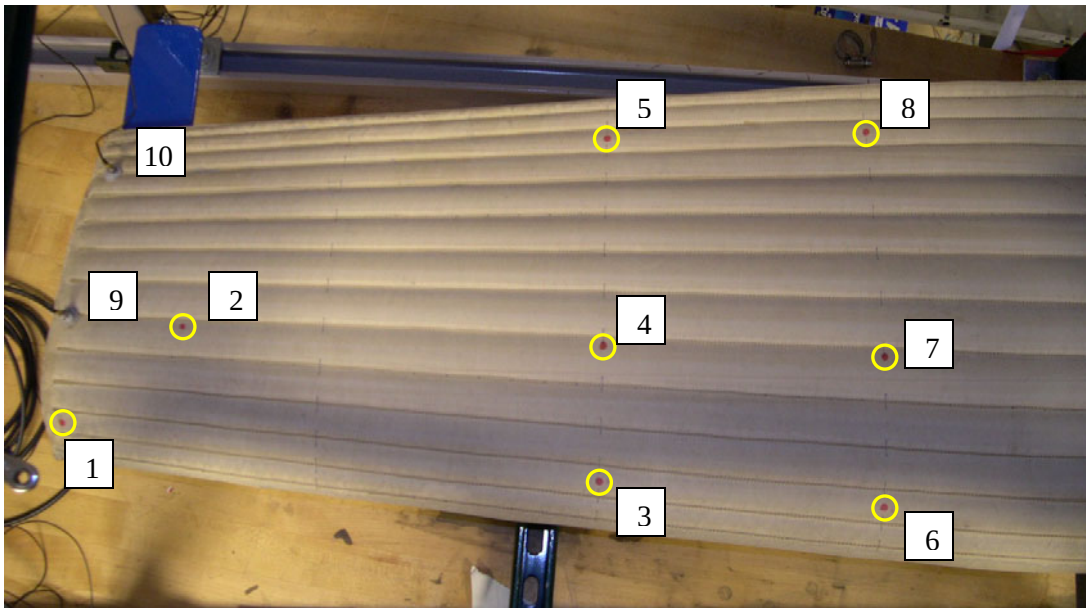

Figure 5.3 – Locations of excitation test points on the wing. Note that excitation points 9 and 10 are also measurement locations of accelerometers

Frequency Response Functions (FRFs), including magnitude and phase, and the coherence of each input/output pair were calculated and recorded in universal file format data files using a Zonic Medallion multichannel data acquisition system and signal analyzer software. For the data acquisition and signal processing, a sampling frame size of 2048 was used, along with a bandwidth frequency of 500 Hz, resulting in a frame period of 1.6 seconds, with a frequency resolution of 0.625 Hz. Ten averages were used at each measurement point. An exponential window was also used for processing of the Fast Fourier Transforms (FFTs) used to compute the FRFs.

Typical FRF and coherence results for two simultaneous response measurements are presented in Figure 5.4. This result is for a wing pressure of 15 psi, impulsive input at Point 4 and measured acceleration response at both locations. The two sensors are located so as to identify different modes of response, including bending and torsional modes. Therefore, these FRFs are not expected to be identical. In the coherence plots, results above 200 Hz are seen to degrade, while results below 200 Hz are good. For the remainder of this chapter, results will be presented for the range 0 to 200 Hz, rather than the full data range of 0 to 500 Hz.

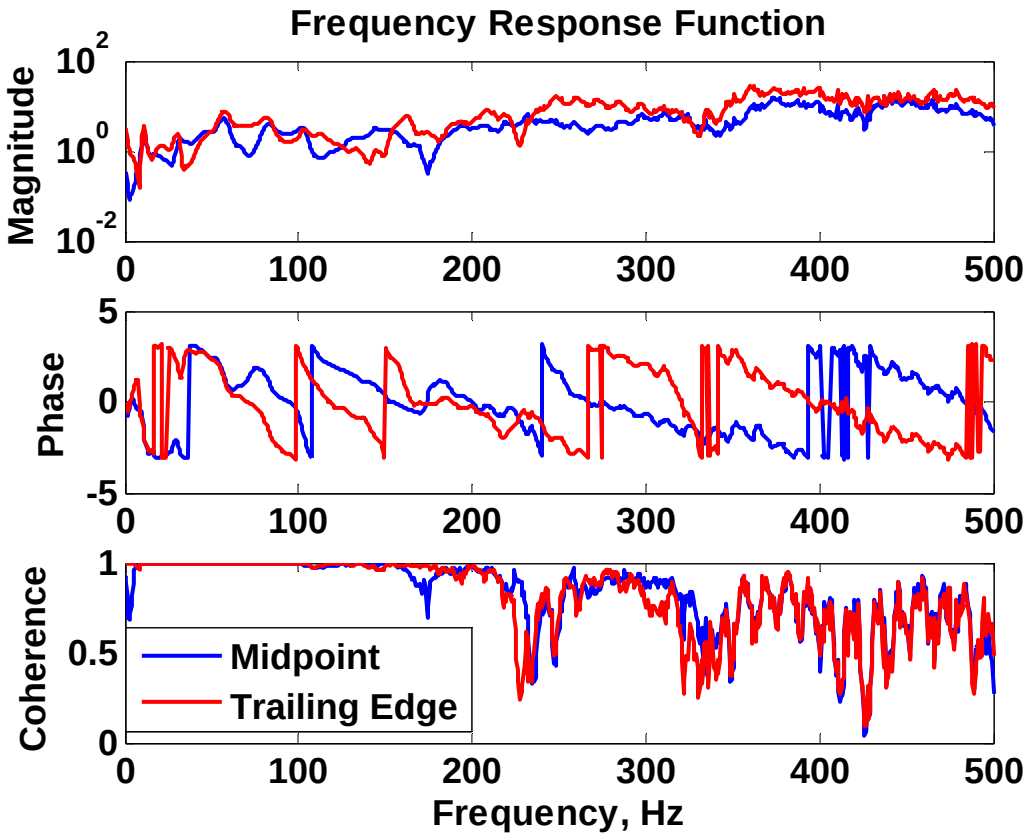

Figure 5.4 – FRFs of wing at both measurement points due to excitation at point 4, with wing internal pressure of 15 psi

5.1.2 Signal Processing and Typical Results

In order to determine the appropriate number of averages to use, tests were conducted using thirty averages with results compared to those of tests using ten averages. Figure 5.5 and Figure 5.6 show the FRFs and coherances of the wing inflated to 20 psig with impulsive input applied at test location 2. In Figure 5.5 and Figure 5.6, the blue data represents the test using ten averages, while the red data represents the test using thirty averages. For the frequency range of interest, (0 to ~200 Hz), there is essentially no difference between the two results. The results shown in Figure 5.5 and Figure 5.6 are representative of results for other input points and all wing pressures. From this study, it

was determined that the average of ten impulse responses is sufficient for testing the inflated wing.

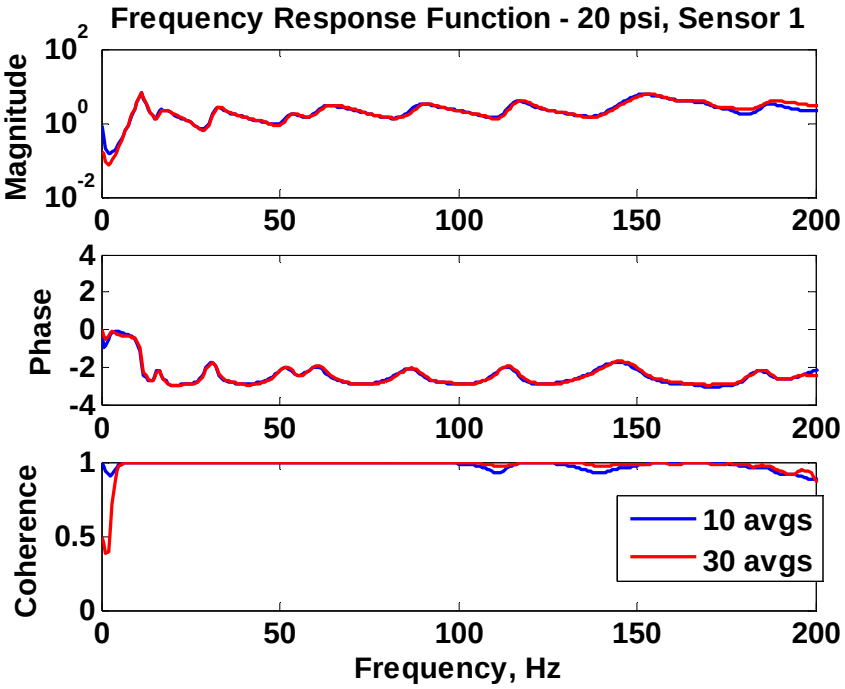

Figure 5.5 – FRF plots comparing 10 and 30 average tests, 20 psig, Sensor 1

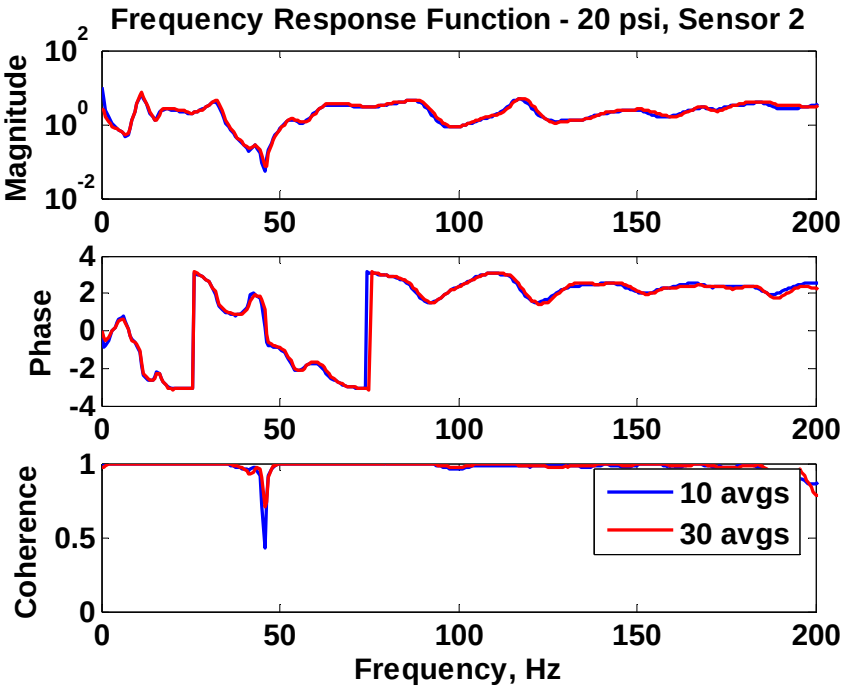

Figure 5.6 – FRF plots comparing 10 and 30 average tests, 20 psig, Sensor 1

In conducting the test, when driving point measurements were recorded, the bottom of the wing was struck with the impulse hammer beneath the sensors. With this data, reciprocity can be examined to evaluate the linearity of the wing response. Figure 5.7 shows the FRF measurements recorded at each measurement point due to an input at the other measurement point for an internal pressure of 5 psig, while Figure 5.8 shows the same for an internal pressure of 25 psig. In each of these Figures, the blue plot represents the accelerometer located at the midpoint of the wing chord and the red plot represents the accelerometer located near the trailing edge. It can be seen that the FRFs correlate reasonably well for the 5 psig case at frequencies up to approximately 120 Hz, at which point the magnitude and phase show slight differences. The coherence, however, shows distinct differences above 120 Hz.

Figure 5.8 shows that for the case of an internal wing pressure of 25 psig, the reciprocal FRFs match nearly exactly up to approximately 150 Hz, and reasonably well from 150 Hz - 200 Hz, the end of the frequency range of interest. This evaluation showed that reciprocity of the wing response is maintained at all pressures, with only slight differences at the higher end of the frequency range of interest. Especially for low pressures, expectations from modal tests of other inflated structures were that reciprocity would not hold.

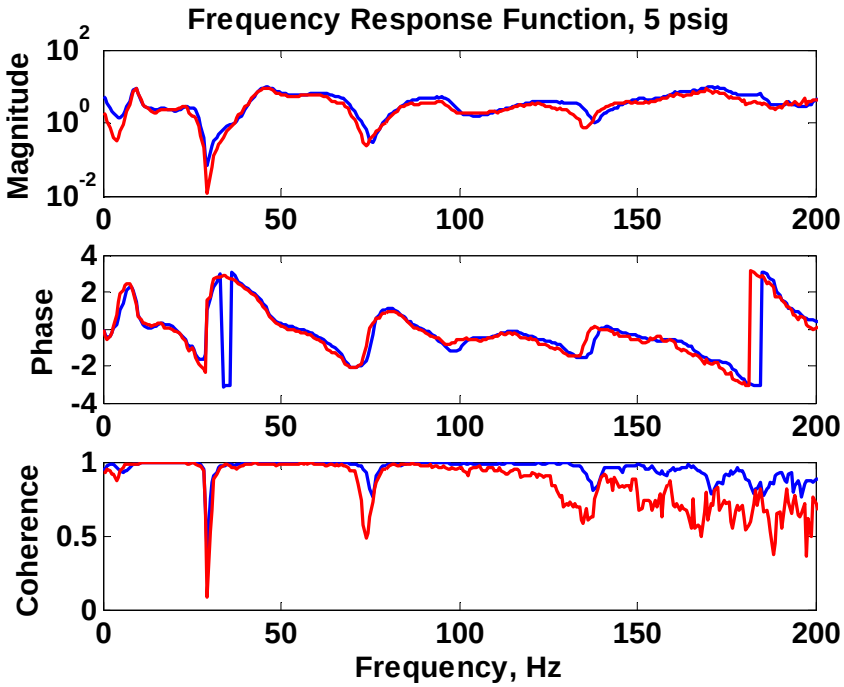

Figure 5.7 – FRF plots demonstrating reciprocity, 5 psig

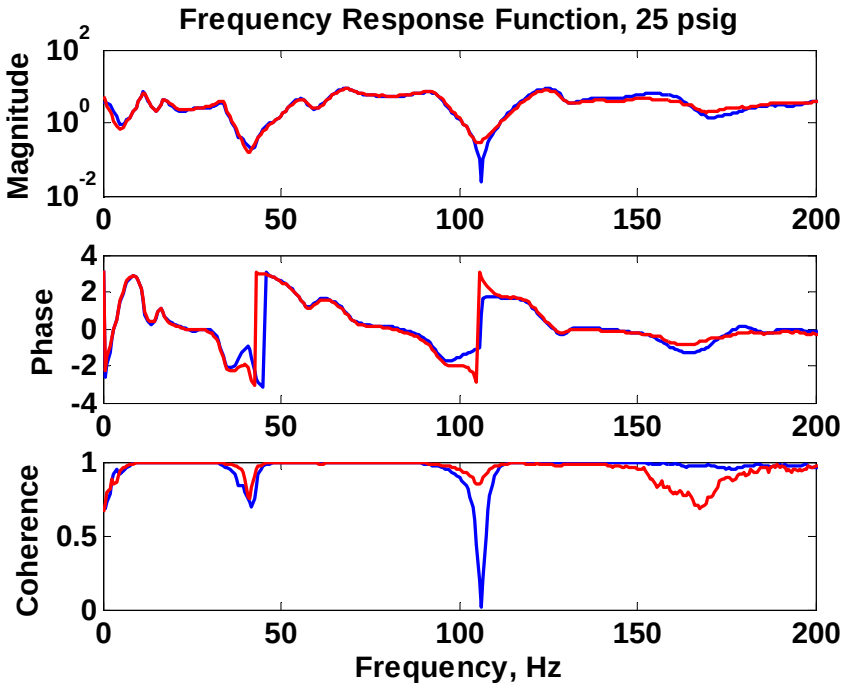

Figure 5.8 – FRF plots demonstrating reciprocity, 25 psig

5.1.3 Modal Parameter Identification

Modal parameter analysis software, X-Modal, developed at the University of Cincinnati Structural Dynamics Research Lab (UC-SDRL), was used with the experimental FRFs to identify resonant frequencies, damping, and mode shapes of the wing for 0-200 Hz. For each pressure case, twenty FRFs were recorded. Eighteen FRFs were combined (excitation Point 2 was excluded for better visualization of mode shapes) and the modal parameter estimation was performed with X-Modal. The polyreference-time-domain (PTD) algorithm was used for this analysis. In determining the resonant frequencies and damping from the FRF data, X-modal creates a consistency diagram. An example of a typical consistency diagram for this effort is shown in Figure 5.9.

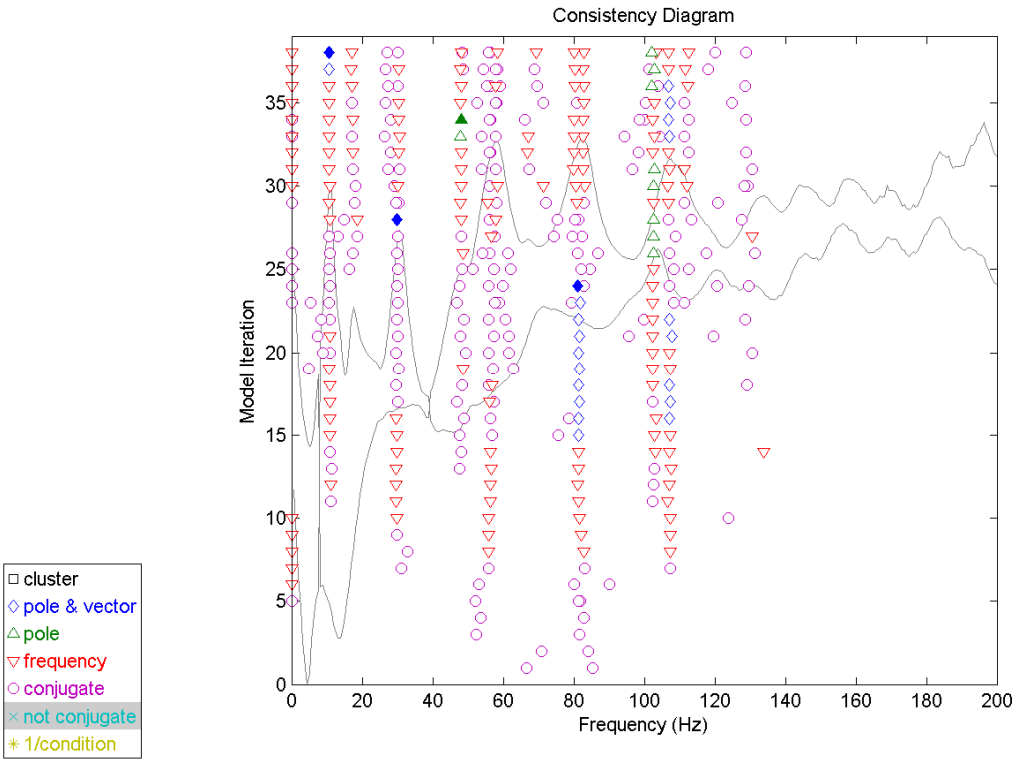

Figure 5.9 – Consistency diagram for modal testing using PTD method

In this analysis, four modes of the cantilevered wing were extracted, which include the first and second bending modes and the first and second torsional modes. Figure 5.10 shows the residue results for a measurement sensor at Point 9 and excitation at Point 3 comparing the PTD results using the estimated modes to the experimental data. Note that other peak frequencies are seen in the consistency diagram but are not selected for identification in Figure 5.9. The frequencies and mode shapes for all modes in the frequency range are included in Table 5.1. The FE model only predicts the first and second bending and torsion modes of the wing, and does not predict the modes between which are combination modes including both bending and torsion. Because of this, only the first and second bending and torsion mode shapes are considered further.

Table 5.1 - Natural frequencies and mode shapes seen in frequency range, 15 psi internal pressure

Mode	Frequency	Description
1	10.6 Hz	1st bending
2	17.3 Hz	Combination mode
3	30.0 Hz	1st torsion
4	48.1 Hz	2nd bending
5	58.3 Hz	Combination mode
6	71.3 Hz	"Tail-flapping" mode
7	81.2 Hz	2nd torsion
8	106.8 Hz	High-order combination mode

For inflation at 15 psig, Figure 5.11 shows four mode shapes correlating to the four bending and torsion frequencies. Note that the mode shapes seen are classical cantilevered beam first and second bending and first and second torsional modes.

Table 5.2 summarizes the damped resonant frequencies and percent of critical damping for each of the pressure cases considered. In reviewing these frequencies, it is seen that for all modes, the frequencies increase with pressure, with the exception of the second bending mode. The frequency of the second bending mode at 10 psi was 52.8 Hz, slightly larger than for the 15psi and 20 psi cases, 48.1 Hz and 51.9 Hz, respectively.

As seen in Figure 5.9, modal identification is user-dependent. All results herein were processed in a consistent manner by the author, but as is typical of all modal identification, some variation in results is expected. In general, however, the identified frequencies follow expected trends, with the wing stiffening with increased pressure. Also, note that for all pressure cases, the first torsional mode occurs at a lower frequency than the second bending mode. The modes are listed out of order of occurrence in Table 5.2 for ease of comparison with FE results.

Note also that high damping percentages were identified for all modes. In each case, identified damping fell in the range of 4% to 10% modal damping. This is not unexpected for an inflatable structure.[37]

Table 5.3 lists the undamped natural frequencies of the system. These were calculated from the damped natural frequencies and damping ratios extracted from the X-Modal analysis by rearranging and using Equation (5-1). While the difference between the undamped and damped natural frequencies is not large, the FE models presented below do not include damping, so it is important to use undamped natural frequencies for model correlation.

$$\omega_d = \omega_n \sqrt{1-\zeta^2} \tag{5-1}$$

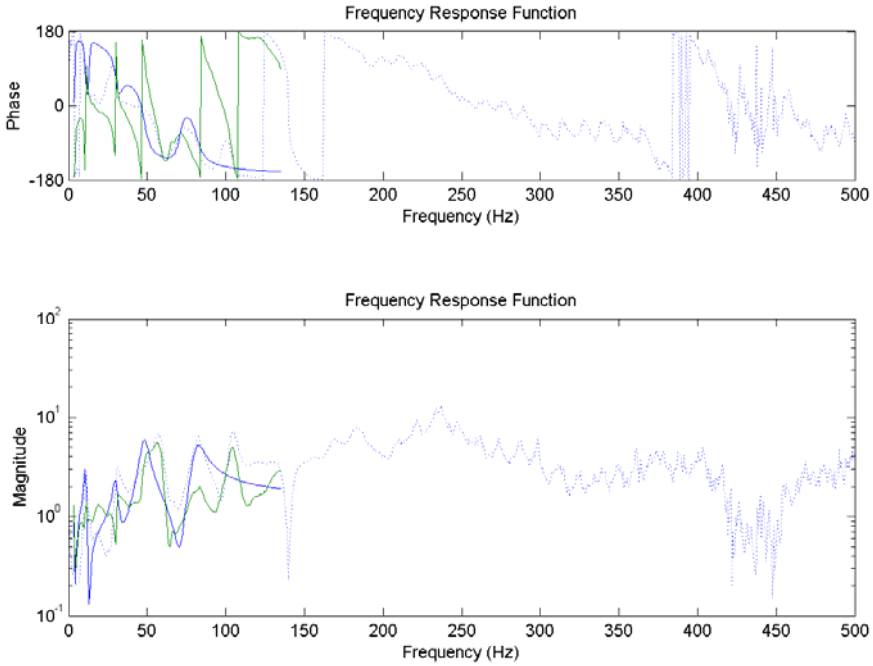

Figure 5.10 – Residue results for the FRF at measurement Point 9 and excitation Point 3

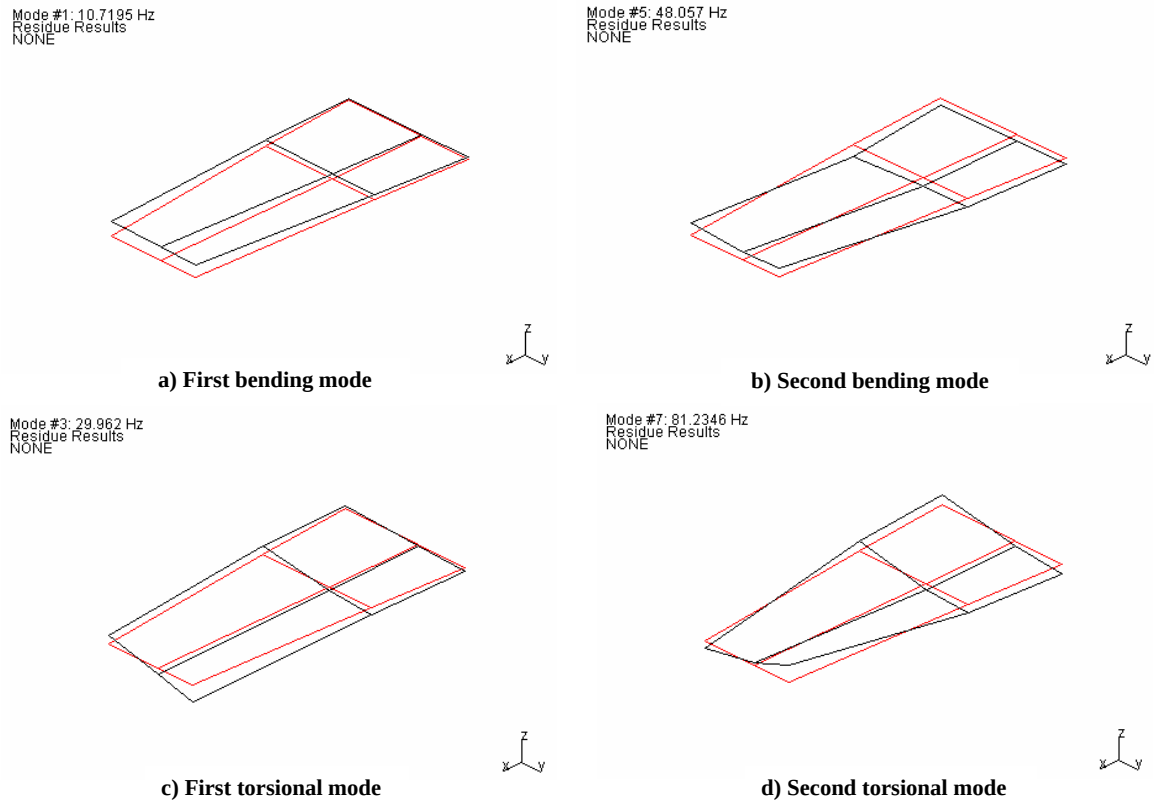

a) First bending mode

b) Second bending mode

c) First torsional mode

d) Second torsional mode

Figure 5.11 – Experimentally determined mode shapes, 15 psig internal pressure

Table 5.2 – Estimated wing damped natural frequencies and damping

	5 psi		10 psi		15 psi		20 psi		25 psi	
Mode	Frequency/Damping		Frequency/Damping		Frequency/Damping		Frequency/Damping		Frequency/Damping	
1st Bending	9.1 Hz	8.1 %	10.2 Hz	6.9 %	10.7 Hz	6.3 %	11.1 Hz	6.4 %	11.2 Hz	6.7 %
2nd Bending	44.4 Hz	6.1 %	52.8 Hz	5.6 %	48.1 Hz	5.9 %	51.9 Hz	5.7 %	54.8 Hz	4.9 %
1st Torsion	23.6 Hz	9.8 %	28.8 Hz	5.7 %	29.9 Hz	5.5 %	31.8 Hz	5.8 %	33.0 Hz	4.9 %
2nd Torsion	62.5 Hz	7.1 %	76.8 Hz	4.6 %	81.3 Hz	5.2 %	86.5 Hz	6.0 %	91.0 Hz	4.5 %

Table 5.3 – Wing undamped natural frequencies and damping

	5 psi		10 psi		15 psi		20 psi		25 psi	
Mode	Frequency/Damping		Frequency/Damping		Frequency/Damping		Frequency/Damping		Frequency/Damping	
1st Bending	9.1 Hz	8.1 %	10.2 Hz	6.9 %	10.7 Hz	6.3 %	11.1 Hz	6.4 %	11.2 Hz	6.7 %
2nd Bending	44.5 Hz	6.1 %	52.9 Hz	5.6 %	48.2 Hz	5.9 %	52.0 Hz	5.7 %	54.9 Hz	4.9 %
1st Torsion	23.7 Hz	9.8 %	28.8 Hz	5.7 %	29.9 Hz	5.5 %	31.9 Hz	5.8 %	33.0 Hz	4.9 %
2nd Torsion	62.7 Hz	7.1 %	76.9 Hz	4.6 %	81.4 Hz	5.2 %	86.7 Hz	6.0 %	91.1 Hz	4.5 %

5.2 FE Modal Analysis

5.2.1 Model Description and Solution Process

The FE model described in Section 4.2 was used to perform a modal analysis of the inflatable wing. Mass was not previously included in the model for simulation of static loadings, but for dynamic response, mass properties are needed. Density for the model was determined by dividing the weight of the wing by the element volume of the model. The resulting density used for the analysis was 2.65e-4 $lb*s^2/in^4$. Note that the weight of the wing includes material clamped at the root for wing mounting. This material is not included in the FE model, so this density is slightly higher than the combined-material areal density for the wing. Damping was not included in the model.

Two solution processes were considered when conducting the FE modal analysis. In the first analysis, internal pressure loadings were applied, a static solution was computed using a linear solver, and a subsequent modal analysis was performed including prestress effects from the pressure loading. The Block-Lanczos solver in ANSYS was used for the modal analysis. In this first analysis, only the “effective” linear orthotropic material model was considered, because inclusion of the nonlinear material model requires the use of a nonlinear solver.

In the second analysis, a nonlinear solver was used to compute the internal pressure solution, and a modal analysis was computed using the prestress effects from the internal pressurization. Again, the modal solution was computed using the Block-Lanczos solver. Both the “effective” linear orthotropic and the modified nonlinear isotropic material models were considered using this analysis process.

5.2.2 Linear Pressurization Results

For the initial FE modal analysis, internal pressure load was applied to all elements making up the external areas of the wing. This static pressure loading solution was then computed using a linear solver. Next, a subsequent modal analysis was computed including the prestress effects from the static pressure solution. The analysis was conducted for pressure loadings of 5, 10, 15, 20, and 25 psi. The initial FE mesh density was used for this analysis, and contained 100,428 DOF.

Table 5.4 lists the resulting natural frequencies of the first five modes predicted from this analysis for all pressure cases considered. Figure 5.12 plots experimental natural frequencies and FE predictions from this analysis. Note that results for the second torsional mode, second bending mode, and, with the exception of the 15 psi case, the first bending mode results compare relatively well. However, the FE predictions of the first torsional mode natural frequencies are much higher than those seen from experimental testing, and are in fact predicted to be higher than the second bending mode natural frequencies for all pressure cases other than 5 psi. Note that for static torsion loading, the FE model also proved much stiffer than the actual wing. Table 5.5 lists the percent error in the natural frequencies predicted by the FE model and those obtained from experimental testing. Note that the chord direction mode listed in Table 5.4 and plotted in Figure 5.12 is only predicted by the FE model, since 1-D accelerometers were used in the experimental modal analysis. This linear pressurization solution was only performed using the linear orthotropic material model, because the nonlinear material model requires the use of a nonlinear solver for solution computation.

Table 5.4 – FE predictions of wing natural frequencies, linear pressure solution

Mode	5 psi	10 psi	15 psi	20 psi	25 psi
1st Bending	13.0 Hz	21.7 Hz	31.0 Hz	20.0 Hz	22.1 Hz
*Mode in chord direction	33.1 Hz	34.1 Hz	34.6 Hz	34.8 Hz	35.5 Hz
2nd Bending	49.8 Hz	55.6 Hz	61.1 Hz	63.3 Hz	69.2 Hz
1st Torsion	44.4 Hz	60.2 Hz	70.4 Hz	73.3 Hz	77.2 Hz
2nd Torsion	71.9 Hz	84.6 Hz	94.1 Hz	105.5 Hz	112.2 Hz

Table 5.5 – Percent error from experimental in linearly applied pressure FE resonant frequencies

Mode	5 psi	10 psi	15 psi	20 psi	25 psi
1st Bending	42.9%	112.7%	189.7%	80.2%	97.3%
2nd Bending	11.9%	5.1%	26.8%	21.7%	26.0%
1st Torsion	87.3%	109.0%	135.5%	129.8%	133.9%
2nd Torsion	14.7%	10.0%	15.6%	21.7%	23.2%

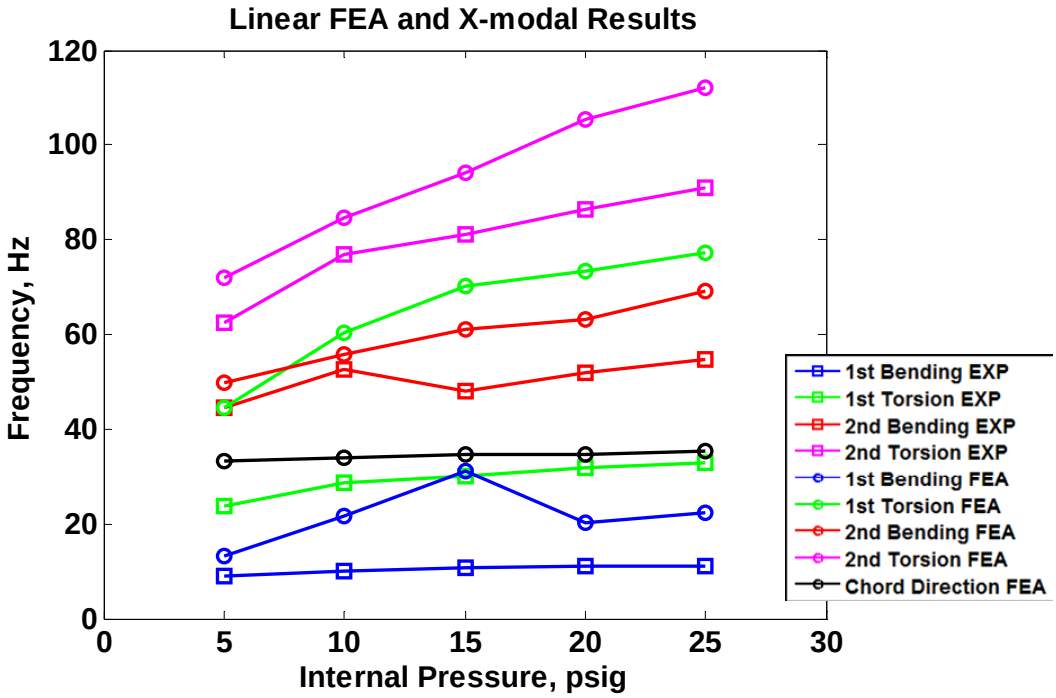

Figure 5.12 – Comparison between estimated wing natural frequencies from experimental modal testing and predicted natural frequencies from FE modal analysis with linear pressurization solution

5.2.3 Nonlinear Pressurization Results

Next, the modal analysis was performed using a nonlinear solver to compute the static pressure preloading. Internal pressure loading was again applied to the external areas of

the wing model, with a nonlinear solver being used to compute this static pressure solution. The initial FE mesh density was used for this analysis, and contained 100,428 DOF. When including prestress effects from a nonlinear static solution in an ANSYS modal analysis, the standard commands cannot be used. Instead of using the standard SOLVE command to perform the modal analysis, the following string of commands must be used [40].

```
/SOLU
ANTYPE,MODAL
PSTRESS,ON
MODOPT,LANB,10
MXPAND,10
PSOLVE,EIGLANB
FINISH

/SOLU
EXPASS,ON
PSOLVE,EIGEXP

FINISH
```

Table 5.6 lists the resulting natural frequency predictions for the 10 and 15 psi cases, along with the percent error in the predicted frequencies from those seen in experimental testing, for a model incorporating the linear orthotropic material model. Higher pressure loading solutions failed to converge. For all cases, the nonlinear pressurization solution predicts the experimental natural frequencies more accurately than the linear pressurization solution. The largest error seen is 40.8%, for the 15 psi first torsion mode, whereas the linear pressurization solution had an error of 109.0% for this case. It is interesting to note that for the 10 psi case, the first torsional frequency is under-predicted by only 1%, but for the 15 psi case, the first torsional frequency is over-predicted by 40.8%. For the 10 psi case, this mode is the most accurately predicted, but for the 15 psi

case it is the prediction with the highest error. It is also of note that for the 10 psi case, the model underpredicts all natural frequencies, indicating a model that is too soft. This is in contrast to static loading cases, where the model continually proved too stiff.

Finally, the same nonlinear pressurization solution process was used with a model incorporating the adjusted nonlinear isotropic material model for 10 psi, and these results along with the percent error from experimental results, are listed in Table 5.7. The intermediate FE mesh density was used for this analysis, and contained 69,750 DOF. Note that when compared with the linear orthotropic material model results, the nonlinear material model more accurately predicts all modes except for the 1st torsion mode. This is an interesting result, since static loadings were more accurately modeled using the linear orthotropic material model. The wing mode shapes predicted from this analysis are seen in Figure 5.13. These mode shapes match those extracted from the experimental modal analysis shown in Figure 5.11. Only 10 psi results are available using this analysis process. When this analysis process was implemented with an internal pressure case of 15 psi, the modal analysis did not return natural frequency predictions.

When the results for the two material models are compared for the 10 psi case, the first and second bending and second torsional frequencies are more accurately predicted by the adjusted nonlinear material model, and are all predicted to within 10% of the experimental values. Only the first torsional frequency is more accurately predicted by the “effective” linear material model, and this is in fact the most accurate prediction out of all FE cases. It is interesting to note that for static loadings, the “effective” linear orthotropic material model was more accurate, while here for the modal analysis, the nonlinear isotropic material model was generally more accurate.

Table 5.6 – FE predictions of wing modes and natural frequencies calculated using non-linear pressure solution, linear orthotropic material model

Mode	10 psi	15 psi	% Error, 10 psi	% Error, 15 psi
1st Bending	9.1 Hz	9.2 Hz	-10.8%	-14.0%
1st Torsion	28.5 Hz	42.1 Hz	-1.0%	40.8%
*Mode in chord direction	32.6 Hz	36.8 Hz	N/A	N/A
2nd Bending	42.7 Hz	46.3 Hz	-19.3%	-3.9%
2nd Torsion	69.2 Hz	92.2 Hz	-10.0%	13.3%

Table 5.7 – FE predictions of wing modes and natural frequencies calculated using, non-linear pressure solution, nonlinear isotropic material model

Mode	FEA 10 psi	% Error, 10 psi
1st Bending	9.9 Hz	-2.9%
1st Torsion	34.1 Hz	18.4%
*Mode in chord direction	38.7 Hz	N/A
2nd Bending	48.0 Hz	-9.3%
2nd Torsion	81.5 Hz	6.0%

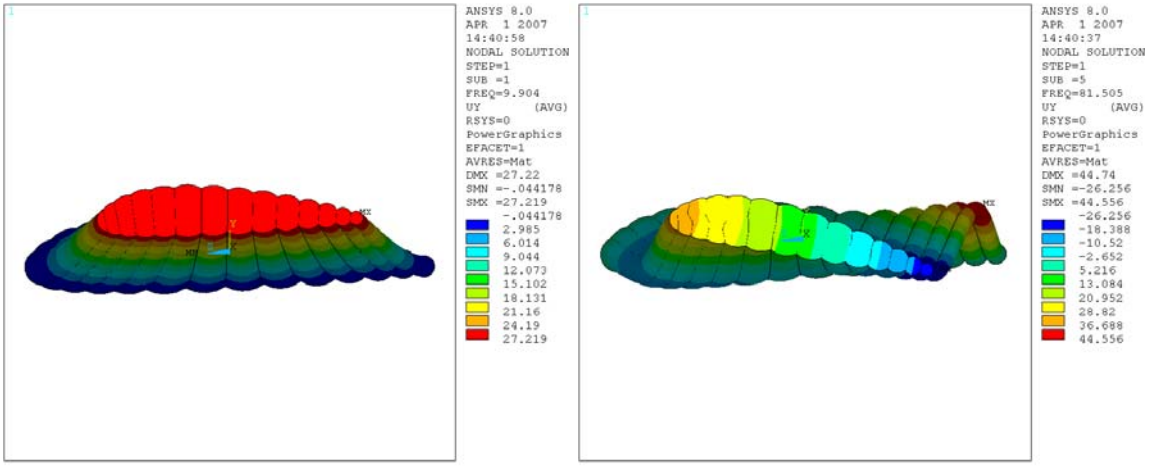

a) First bending mode **b) First torsional mode**

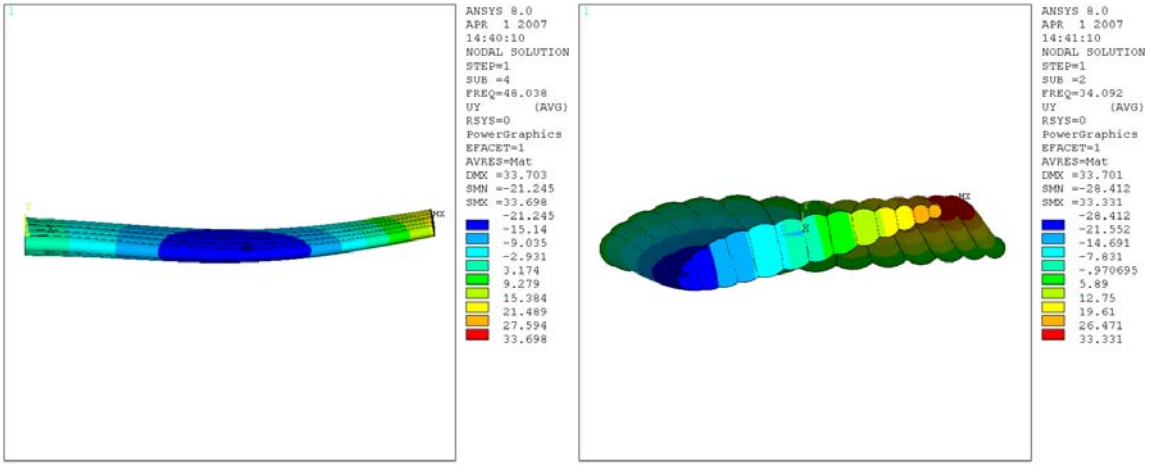

c) Second bending mode **d) Second torsional mode**

Figure 5.13 – FE predicted mode shapes using adjusted nonlinear isotropic material model and mesh density of 69,750 DOF

CHAPTER 6: SUMMARY

6.1 Detailed Summary

Initial material properties were determined from testing performed by ILC Dover, and these tests and resulting material properties were presented. Additionally, static testing was performed on the wing to determine wing response to bending and twisting loads and provide a means to validate a FE model. Bending tests were performed, and it was found that nominally equivalent wings respond with wide variation. In addition, responses to torsion loads at the wing tip were investigated. In all static tests, a high level of hysteresis was evident in the wing.

A finite element model of an inflatable wing was developed using ANSYS FE software. Modeling concepts were validated by first creating FE models of inflatable Vectran cylinders and simulating a shear modulus test. The FE model of the inflatable wing included nonlinear solutions to internal pressure loading and external force loading. A two-step analysis procedure was implemented in the wing model, with internal pressurization being applied in one solution, and a subsequent solution step where external loadings were applied.

Both linear orthotropic and nonlinear isotropic material models were considered. An “effective” linear orthotropic material model was found to correlate well to low tip force bending loads at 10 psi internal pressure, and for tip loads up to 11.24 lbf for internal pressure of 15 psi. Little difference was seen between resulting bending deflections between the 10 psi and 15 psi solutions. An adjusted nonlinear isotropic material model proved stiffer than the “effective” linear orthotropic model for the 10 psi case. However, when an internal pressure of 15 psi was considered, the resulting bending deflections in

the model were actually greater than those seen in laboratory testing. The linear orthotropic material model showed little difference between two pressure solutions, underpredicting deflections compared to experimental results. The nonlinear isotropic material model provided substantially different deflections for different pressures, but overpredicted deflections compared with 15 psi experimental values.

Mesh density studies were conducted and it was found that when using the nonlinear isotropic material model, a much more coarse mesh could be used to obtain solutions for an internal pressure of 10 psi. This mesh resulted in greatly reduced solution times.

Dynamic response of the wing was investigated through an experimental modal analysis. A standard impact hammer test was conducted with two output accelerometers and nine input locations. Unexpected results from this experimental test were the clean FRF's from an inflatable structure, and the fact that the reciprocity of the system was good. Previous inflatable programs suggested that neither of these would be true. From this test, wing natural frequencies and mode shapes were identified.

Two types of FE modal analyses were considered, with one obtaining the pressure preloading solution using a linear solver, while the second used a nonlinear solver. It was found that the linear pressurization solution predicted the second bending and second torsion natural frequencies relatively well, but errors in predicting the first bending and especially the first torsion mode were much higher. The nonlinear pressurization solution generally predicted all four natural frequencies, first and second bending and first and second torsion more accurately, though only low internal pressure solutions converged. The fundamental frequency of the wing was most accurately predicted using the

nonlinear pressurization solution process and the nonlinear isotropic material model, with and error less than 3%.

6.2 Contributions

Contributions to the community from this work are:

- Static wing response to bending and torsion loads has been documented from experimental testing
- Natural frequencies and mode shapes of an inflatable wing have been determined through an experimental modal analysis. Impact hammer testing was shown to be an effective method for conducting such tests.
- A finite element model of an inflatable wing was created
    - Material properties were explored, and reduction factors were determined and applied to experimental tensile test material data.
    - Wing warping forces were modeled qualitatively.
    - FE predictions of natural frequencies and mode shapes shows promise that the model can be used to effectively model dynamic wing response.
- Overall, the FE modeling processes documented herein provide a valuable reference for future modeling of inflatable wings.

6.3 Future Work

An area for further studies is adjustment of the FE model to include properties of the internal bladder. Current material properties are based on the Vectran material only. It may be possible to develop a hybrid material model that more accurately models the

response of the wing. Related to this, testing of other wings constructed of only one layer of urethane-coated nylon would provide data for a system comparable to the bladder. Comparisons of the response of such a wing to the Vectran wings would lead to determining whether the bladder or the Vectran restraint dominates wing response.

An alternative option would be to apply the FE methodology herein to wings constructed of urethane-coated nylon. This would also lead to a determination of the level that the bladder dominates the wing response.

Another possible area for future work is conducting tests to determine modulus properties of the fabric while inflated. Perhaps the reason that the model continually proves too stiff for static loading is the reliance on material properties of Vectran strips. It may be that the restraint stiffness does not dominate wing response.

Investigation into other element types that would better model the stress-stiffening effects of the internal pressurization is also recommended. The current model does not effectively stiffen with increasing pressure. This could also lead to possible ways to include hysteresis and creep in the model.

Other forms of wing warping in addition to modeling servo moments could also be considered. Modeling wing response to application of smart materials would be beneficial, though work to increase the model's accuracy is recommended first.

APPENDIX A: ANSYS BATCH FILE COMMANDS

The following batch commands were used to create the finite element model of the inflatable wing. Three material models are included. For linear orthotropic material properties, the parameters defined at the beginning of the file are used. Nonlinear isotropic material models are also included, but as printed are commented out. To use either nonlinear material model, the comments from that section must be removed and the linear orthotropic section should be commented out. Commands for three mesh densities are included, with the two coarser meshes currently commented out. When changing the mesh density, the load application nodes must also be changed, and these changes are also included as comments. Three solution files are included, separated below by lines of "#######," and each is clearly labeled at the beginning.

Also included is a sample batch input file for simulating wing warping. This file begins on Page 107.

```
! This file creates the geometry and mesh for the inflatable wing model.

 /filname, FILENAME
 /prep7

! define parameters
        e_fill=         1.22e6*.08
        e_warp=         1.36e6*.08
        shear_mod=      20e3
        int_press=      10
        tip_load=       2.2481


! change view for interactive mode
 /VIEW,1,1

! create root keypoints
        K, 1, 0.000000,         -0.5595000,             8.500500,
        K, 2, 0.000000,          0.9758637E-01,         8.100849,
```

K, 3, 0.000000, -1.296945, 7.821943,
K, 4, 0.000000, 0.5779612, 7.401153,
K, 5, 0.000000, -1.471254, 6.991310,
K, 6, 0.000000, 1.033980, 6.337101,
K, 7, 0.000000, -1.538836, 5.970979,
K, 8, 0.000000, 1.346173, 5.036847,
K, 9, 0.000000, -1.552504, 4.796735,
K,10, 0.000000, 1.444189, 3.545226,
K,11, 0.000000, -1.491011, 3.460233,
K,12, 0.000000, 1.407859, 1.817772,
K,13, 0.000000, -1.416350, 1.829688,
K,14, 0.000000, 1.294533, 0.1071999,
K,15, 0.000000, -1.354123, 0.1718821,
K,16, 0.000000, 1.096033, -1.502466,
K,17, 0.000000, -1.254139, -1.418965,
K,18, 0.000000, 0.8318012, -3.047054,
K,19, 0.000000, -1.127290, -2.946888,
K,20, 0.000000, 0.5584566, -4.482636,
K,21, 0.000000, -1.022033, -4.381605,
K,22, 0.000000, 0.2928351, -5.730581,
K,23, 0.000000, -0.9289871, -5.642207,
K,24, 0.000000, 0.1400362E-01, -6.823949,
K,25, 0.000000, -0.8221342, -6.755400,
K,26, 0.000000, -0.2273438, -7.744520,
K,27, 0.000000, -0.7510242, -7.692574,
K,28, 0.000000, -0.5235000, -8.500500,
K,29, 0.000000, -0.1749602, 8.392741,
K,30, 0.000000, 0.4109251, 7.801201,
K,31, 0.000000, 0.9285751, 6.921547,
K,32, 0.000000, 1.340398, 5.723125,
K,33, 0.000000, 1.577005, 4.302984,
K,34, 0.000000, 1.667131, 2.676428,
K,35, 0.000000, 1.597981, 0.9461363,
K,36, 0.000000, 1.433291, -0.7269837,
K,37, 0.000000, 1.214384, -2.317608,
K,38, 0.000000, 0.9521861, -3.813790,
K,39, 0.000000, 0.6656415, -5.157691,
K,40, 0.000000, 0.3926820, -6.338282,
K,41, 0.000000, 0.1293430, -7.346110,
K,42, 0.000000, -0.1175397, -8.223535,
K,43, 0.000000, -0.9431758, -8.182687,
K,44, 0.000000, -1.021820, -7.241836,
K,45, 0.000000, -1.115986, -6.221881,
K,46, 0.000000, -1.214917, -5.029577,
K,47, 0.000000, -1.326415, -3.682717,
K,48, 0.000000, -1.431923, -2.202952,

```
        K,49, 0.000000,     -1.534564,     -0.6380242,
        K,50, 0.000000,     -1.615368,     0.9921470,
        K,51, 0.000000,     -1.666754,     2.635204,
        K,52, 0.000000,     -1.665784,     4.121857,
        K,53, 0.000000,     -1.663397,     5.385171,
        K,54, 0.000000,     -1.607600,     6.488050,
        K,55, 0.000000,     -1.470940,     7.424868,
        K,56, 0.000000,     -1.060565,     8.305049,

! create root lines
        LARC,  1,  2, 29
        LARC,  2,  4, 30
        LARC,  4,  6, 31
        LARC,  6,  8, 32
        LARC,  8, 10, 33
        LARC, 10, 12, 34
        LARC, 12, 14, 35
        LARC, 14, 16, 36
        LARC, 16, 18, 37
        LARC, 18, 20, 38
        LARC, 20, 22, 39
        LARC, 22, 24, 40
        LARC, 24, 26, 41
        LARC, 26, 28, 42
        LARC, 28, 27, 43
        LARC, 27, 25, 44
        LARC, 25, 23, 45
        LARC, 23, 21, 46
        LARC, 21, 19, 47
        LARC, 19, 17, 48
        LARC, 17, 15, 49
        LARC, 15, 13, 50
        LARC, 13, 11, 51
        LARC, 11,  9, 52
        LARC,  9,  7, 53
        LARC,  7,  5, 54
        LARC,  5,  3, 55
        LARC,  3,  1, 56

! create component of constrained lines
        CM,l_root_constr,LINE

! create spar lines
        LSTR,  2,  3
        LSTR,  4,  5
        LSTR,  6,  7
```

```
        LSTR,  8,  9
        LSTR, 10, 11
        LSTR, 12, 13
        LSTR, 14, 15
        LSTR, 16, 17
        LSTR, 18, 19
        LSTR, 20, 21
        LSTR, 22, 23
        LSTR, 24, 25
        LSTR, 26, 27

! create component of all root lines
        CM,l_root,LINE

! create tip profile by scaling down root lines
        LSSCALE,all,,,.65,.65,.65,,0,0

! unselect root lines
        CMSEL,U,l_root


! move tip profile to proper location
        LGEN,,all,,,36,0,0,,,1
        CM,l_tip,LINE

        ALLSEL,all

! create restraint/spar lines
        LSTR,  1, 57
        LSTR,  2, 58
        LSTR,  4, 59
        LSTR,  6, 60
        LSTR,  8, 61
        LSTR, 10, 62
        LSTR, 12, 63
        LSTR, 14, 64
        LSTR, 16, 65
        LSTR, 18, 66
        LSTR, 20, 67
        LSTR, 22, 68
        LSTR, 24, 69
        LSTR, 26, 70
        LSTR, 28, 71
        LSTR, 27, 72
        LSTR, 25, 73
        LSTR, 23, 74
```

```
LSTR, 21, 75
LSTR, 19, 76
LSTR, 17, 77
LSTR, 15, 78
LSTR, 13, 79
LSTR, 11, 80
LSTR,  9, 81
LSTR,  7, 82
LSTR,  5, 83
LSTR,  3, 84

! create restraint areas
AL,  1,  84, 42, 83
AL,  2,  85, 43, 84
AL,  3,  86, 44, 85
AL,  4,  87, 45, 86
AL,  5,  88, 46, 87
AL,  6,  89, 47, 88
AL,  7,  90, 48, 89
AL,  8,  91, 49, 90
AL,  9,  92, 50, 91
AL, 10,  93, 51, 92
AL, 11,  94, 52, 93
AL, 12,  95, 53, 94
AL, 13,  96, 54, 95
AL, 14,  97, 55, 96
AL, 15,  98, 56, 97
AL, 16,  99, 57, 98
AL, 17, 100, 58, 99
AL, 18, 101, 59, 100
AL, 19, 102, 60, 101
AL, 20, 103, 61, 102
AL, 21, 104, 62, 103
AL, 22, 105, 63, 104
AL, 23, 106, 64, 105
AL, 24, 107, 65, 106
AL, 25, 108, 66, 107
AL, 26, 109, 67, 108
AL, 27, 110, 68, 109
AL, 28,  83, 69, 110

! create spar areas
AL, 29, 84, 70, 110
AL, 30, 85, 71, 109
AL, 31, 86, 72, 108
AL, 32, 87, 73, 107
```

```
AL, 33, 88, 74, 106
AL, 34, 89, 75, 105
AL, 35, 90, 76, 104
AL, 36, 91, 77, 103
AL, 37, 92, 78, 102
AL, 38, 93, 79, 101
AL, 39, 94, 80, 100
AL, 40, 95, 81, 99
AL, 41, 96, 82, 98


! create keypoints for tip spline
KL, 70, .5,,
KL, 71, .5,,
KL, 72, .5,,
KL, 73, .5,,
KL, 74, .5,,
KL, 75, .5,,
KL, 76, .5,,
KL, 77, .5,,
KL, 78, .5,,
KL, 79, .5,,
KL, 80, .5,,
KL, 81, .5,,
KL, 82, .5,,

! create tip spline
KSEL,S,KP,,57
KSEL,A,KP,,71
KSEL,A,KP,,86,97,1

BSPLIN,all,
ALLSEL,all

! create wing tip areas
LSEL,S,LINE,,42,55,1
LSEL,A,LINE,,111
AL,all

LSEL,S,LINE,,56,69,1
LSEL,A,LINE,,111
AL,all

ALLSEL, all
```

```
! create components

  !wing endcap
    ASEL,S,AREA,,42,43,1
    CM,a_endcap,AREA

  !wing restraint
    ASEL,S,AREA,,1,28,1
    CM,a_restraint,AREA

  !internal spars
    ASEL,S,AREA,,29,41,1
    CM,a_spars,AREA

  !endseam line
        LSEL,S,LINE,,111
    CM,l_endseam,LINE

  !lines at wing tip
        CMSEL,S,l_tip
        CMSEL,A,l_endseam
        CM,l_tip,LINE

! Reverse area normals
        CMSEL,S,a_endcap
        CMSEL,A,a_restraint
        AREVERSE,all,0

        ALLSEL, all

! Define Element type and real constants
        ET,1,SHELL181
        R,1,.013,,,,,,
        RMORE,,,,,,,

! define linear orthotropic material properties
        MPTEMP,,,,,,,,
        MPTEMP,1,0
        MPDATA,EX,1,,e_warp
        MPDATA,EY,1,,e_fill
        MPDATA,EZ,1,,e_fill
        MPDATA,PRXY,1,,
        MPDATA,PRYZ,1,,
        MPDATA,PRXZ,1,,
        MPDATA,GXY,1,,shear_mod
        MPDATA,GYZ,1,,shear_mod
```

```
        MPDATA,GXZ,1,,shear_mod

! define nonlinear isotropic material properties (100% of testing)
!       MPTEMP,,,,,,,,
!       MPTEMP,1,0
!       MPDATA,EX,1,,e_fill
!       *CREATE,file1.UNIA
!       0 0
!       0.058268908 2915
!       0.072320662 5375
!       0.086177696 11990
!       0.122217633 39550
!       *END
!       TBFT,EADD,1,UNIA,file1.UNIA
!       /DELETE,file1.UNIA
!       TBFT,FADD,1,HYPER,MOON,3
!       TBFT,SOLVE,1,HYPER,MOON,3,1
!       TBFT,FSET,1,HYPER,MOON,3

! define nonlinear isotropic material properties (75% of testing)
!       MPTEMP,,,,,,,,
!       MPTEMP,1,0
!       MPDATA,EX,1,,e_fill
!       *CREATE,file1.UNIA
!       0 0
!       0.058268908 2186.25
!       0.072320662 4031.25
!       0.086177696 8992.5
!       0.122217633 29662.5
!       *END
!       TBFT,EADD,1,UNIA,file1.UNIA
!       /DELETE,file1.UNIA
!       TBFT,FADD,1,HYPER,MOON,3
!       TBFT,SOLVE,1,HYPER,MOON,3,1
!       TBFT,FSET,1,HYPER,MOON,3



! Set mesh sizing for warp direction
        CMSEL,U,L_ROOT
        CMSEL,U,L_TIP
        LESIZE,all,,,72,0.5,1,,,0                   ! original mesh
!       LESIZE,all,,,50,.5,1 , , ,0                 !coarse mesh
!       LESIZE,all,,,25,.5,1 , , ,0                 !reduced solution time mesh

        ALLSEL,ALL
```

```
! mesh restraint and spars
        CMSEL,U,A_ENDCAP
        amesh, all

! mesh endcap
        CMSEL,S,l_endseam
        LESIZE,all, , ,70,.5,1 , , ,0          ! original mesh
!       LESIZE,all, , ,50,.5,1 , , ,0          ! coarse mesh
!       LESIZE,all, , ,30,.5,1 , , ,0          ! reduced solution time mesh
        ALLSEL,ALL
        CMSEL,S,A_ENDCAP
        amesh, all


        ALLSEL, ALL

! create bending tip force component on bottom
        NSEL,S,NODE,,9053                      ! original mesh
!       NSEL,S,NODE,,6326                      ! coarse mesh
!       NSEL,S,NODE,,3227                      ! reduced solution time mesh
        CM,n_tip_load_up,NODE

        ALLSEL,ALL

! Save database as certain filename
        SAVE

!#########################################################
! Solution commands for bending loads

! set solution options
        /SOLU

        NLGEOM,ON
        NSUBST,1000,7500,150
        LNSRCH,ON
!       OUTRES,ERASE
!       OUTRES,ALL,10

! apply constraints on root
        CMSEL,S,l_root_constr
        DL,all, ,ALL,

! apply internal pressure
        CMSEL,S,a_restraint
```

```
        CMSEL,A,a_endcap
        SFA,all,1,PRES,int_press
        ALLSEL,ALL

        SSTIF,ON
        SOLVE

! apply tip load
        CMSEL,S,n_tip_load_up
        F,all,FY,tip_load

        ALLSEL,ALL

        SSTIF,ON
        SOLVE

FINISH
!/exit, nosave




!#########################################################
! Solution commands for linear pressurization modal analysis

! assign results file
!       /ASSIGN,RST,

! set solution options
        /SOLU

! apply constraints on root
        CMSEL,S,l_root_constr
        DL,all, ,ALL,

! apply internal pressure
        CMSEL,S,a_restraint
        CMSEL,A,a_endcap
        SFA,all,1,PRES,int_press
        ALLSEL,ALL
        PSTRES,ON
        SOLVE
        FINISH
```

```
        /SOLU
        ANTYPE,MODAL
        MODOPT,LANB,10
        PSTRES,ON
        SOLVE

FINISH
!/exit, nosave









!#########################################################
! Solution commands for nonlinear pressurization modal analysis
! set solution options
        /SOLU
        NLGEOM,ON
        NSUBST,1500,10000,150
        LNSRCH,ON
!       OUTRES,ERASE
!       OUTRES,ALL,25

        PSTRESS,ON


! apply constraints on root

        CMSEL,S,l_root_constr
        DL,all, ,ALL,
```

```
! apply internal pressure
        CMSEL,S,a_restraint
        CMSEL,A,a_endcap
        SFA,all,1,PRES,int_press
        ALLSEL,ALL

        SOLVE

        FINISH

        /SOLU
        ANTYPE,MODAL
        PSTRESS,ON
        MODOPT,LANB,10
        MXPAND,10
        PSOLVE,EIGLANB
        FINISH

        /SOLU
        EXPASS,ON
        PSOLVE,EIGEXP

FINISH
!/exit, nosave
```

```
! The following file creates and solves the FE model of the FASM wing with applied
wing warping forces.

 /filname, warp_1
 /prep7

! define parameters
        int_press=      10
        warp_mom=   8

! change view for interactive mode
 /VIEW,1,1

! create root keypoints
        K, 1, 0.000000, -0.5595000,             8.500500,
        K, 2, 0.000000,  0.9758637E-01, 8.100849,
        K, 3, 0.000000, -1.296945,              7.821943,
        K, 4, 0.000000,  0.5779612,             7.401153,
        K, 5, 0.000000, -1.471254,              6.991310,
        K, 6, 0.000000,  1.033980,              6.337101,
        K, 7, 0.000000, -1.538836,              5.970979,
        K, 8, 0.000000,  1.346173,              5.036847,
        K, 9, 0.000000, -1.552504,              4.796735,
        K,10, 0.000000,  1.444189,              3.545226,
        K,11, 0.000000, -1.491011,              3.460233,
        K,12, 0.000000,  1.407859,              1.817772,
        K,13, 0.000000, -1.416350,              1.829688,
        K,14, 0.000000,  1.294533,              0.1071999,
        K,15, 0.000000, -1.354123,              0.1718821,
        K,16, 0.000000,  1.096033,              -1.502466,
        K,17, 0.000000, -1.254139,              -1.418965,
        K,18, 0.000000,  0.8318012,             -3.047054,
        K,19, 0.000000, -1.127290,              -2.946888,
        K,20, 0.000000,  0.5584566,             -4.482636,
        K,21, 0.000000, -1.022033,              -4.381605,
        K,22, 0.000000,  0.2928351,             -5.730581,
        K,23, 0.000000, -0.9289871,             -5.642207,
        K,24, 0.000000,  0.1400362E-01,         -6.823949,
        K,25, 0.000000, -0.8221342,             -6.755400,
        K,26, 0.000000, -0.2273438,             -7.744520,
        K,27, 0.000000, -0.7510242,             -7.692574,
        K,28, 0.000000, -0.5235000,             -8.500500,
        K,29, 0.000000, -0.1749602,             8.392741,
        K,30, 0.000000,  0.4109251,             7.801201,
        K,31, 0.000000,  0.9285751,             6.921547,
        K,32, 0.000000,  1.340398,              5.723125,
```

```
K,33, 0.000000,  1.577005,        4.302984,
K,34, 0.000000,  1.667131,        2.676428,
K,35, 0.000000,  1.597981,        0.9461363,
K,36, 0.000000,  1.433291,        -0.7269837,
K,37, 0.000000,  1.214384,        -2.317608,
K,38, 0.000000,  0.9521861,       -3.813790,
K,39, 0.000000,  0.6656415,       -5.157691,
K,40, 0.000000,  0.3926820,       -6.338282,
K,41, 0.000000,  0.1293430,       -7.346110,
K,42, 0.000000, -0.1175397,       -8.223535,
K,43, 0.000000, -0.9431758,       -8.182687,
K,44, 0.000000, -1.021820,        -7.241836,
K,45, 0.000000, -1.115986,        -6.221881,
K,46, 0.000000, -1.214917,        -5.029577,
K,47, 0.000000, -1.326415,        -3.682717,
K,48, 0.000000, -1.431923,        -2.202952,
K,49, 0.000000, -1.534564,        -0.6380242,
K,50, 0.000000, -1.615368,        0.9921470,
K,51, 0.000000, -1.666754,        2.635204,
K,52, 0.000000, -1.665784,        4.121857,
K,53, 0.000000, -1.663397,        5.385171,
K,54, 0.000000, -1.607600,        6.488050,
K,55, 0.000000, -1.470940,        7.424868,
K,56, 0.000000, -1.060565,        8.305049,

! create root lines
    LARC,  1,  2, 29
    LARC,  2,  4, 30
    LARC,  4,  6, 31
    LARC,  6,  8, 32
    LARC,  8, 10, 33
    LARC, 10, 12, 34
    LARC, 12, 14, 35
    LARC, 14, 16, 36
    LARC, 16, 18, 37
    LARC, 18, 20, 38
    LARC, 20, 22, 39
    LARC, 22, 24, 40
    LARC, 24, 26, 41
    LARC, 26, 28, 42
    LARC, 28, 27, 43
    LARC, 27, 25, 44
    LARC, 25, 23, 45
    LARC, 23, 21, 46
    LARC, 21, 19, 47
    LARC, 19, 17, 48
```

```
        LARC, 17, 15, 49
        LARC, 15, 13, 50
        LARC, 13, 11, 51
        LARC, 11,  9, 52
        LARC,  9,  7, 53
        LARC,  7,  5, 54
        LARC,  5,  3, 55
        LARC,  3,  1, 56

! create component of constrained lines
        CM,l_root_constr,LINE

! create spar lines
        LSTR,  2,  3
        LSTR,  4,  5
        LSTR,  6,  7
        LSTR,  8,  9
        LSTR, 10, 11
        LSTR, 12, 13
        LSTR, 14, 15
        LSTR, 16, 17
        LSTR, 18, 19
        LSTR, 20, 21
        LSTR, 22, 23
        LSTR, 24, 25
        LSTR, 26, 27

! create component of all root lines
        CM,l_root,LINE

! create tip profile by scaling down root lines
        LSSCALE,all,,,.65,.65,.65,,0,0

! unselect root lines
        CMSEL,U,l_root


! move tip profile to proper location
        LGEN,,all,,,36,0,0,,,1
        CM,l_tip,LINE

        ALLSEL,all

! create restraint/spar lines
        LSTR,  1, 57
        LSTR,  2, 58
```

```
LSTR,  4, 59
LSTR,  6, 60
LSTR,  8, 61
LSTR, 10, 62
LSTR, 12, 63
LSTR, 14, 64
LSTR, 16, 65
LSTR, 18, 66
LSTR, 20, 67
LSTR, 22, 68
LSTR, 24, 69
LSTR, 26, 70
LSTR, 28, 71
LSTR, 27, 72
LSTR, 25, 73
LSTR, 23, 74
LSTR, 21, 75
LSTR, 19, 76
LSTR, 17, 77
LSTR, 15, 78
LSTR, 13, 79
LSTR, 11, 80
LSTR,  9, 81
LSTR,  7, 82
LSTR,  5, 83
LSTR,  3, 84

! create restraint areas
AL,  1,  84, 42, 83
AL,  2,  85, 43, 84
AL,  3,  86, 44, 85
AL,  4,  87, 45, 86
AL,  5,  88, 46, 87
AL,  6,  89, 47, 88
AL,  7,  90, 48, 89
AL,  8,  91, 49, 90
AL,  9,  92, 50, 91
AL, 10,  93, 51, 92
AL, 11,  94, 52, 93
AL, 12,  95, 53, 94
AL, 13,  96, 54, 95
AL, 14,  97, 55, 96
AL, 15,  98, 56, 97
AL, 16,  99, 57, 98
AL, 17, 100, 58, 99
AL, 18, 101, 59, 100
```

```
        AL, 19, 102, 60, 101
        AL, 20, 103, 61, 102
        AL, 21, 104, 62, 103
        AL, 22, 105, 63, 104
        AL, 23, 106, 64, 105
        AL, 24, 107, 65, 106
        AL, 25, 108, 66, 107
        AL, 26, 109, 67, 108
        AL, 27, 110, 68, 109
        AL, 28,  83, 69, 110

! create spar areas
        AL, 29, 84, 70, 110
        AL, 30, 85, 71, 109
        AL, 31, 86, 72, 108
        AL, 32, 87, 73, 107
        AL, 33, 88, 74, 106
        AL, 34, 89, 75, 105
        AL, 35, 90, 76, 104
        AL, 36, 91, 77, 103
        AL, 37, 92, 78, 102
        AL, 38, 93, 79, 101
        AL, 39, 94, 80, 100
        AL, 40, 95, 81, 99
        AL, 41, 96, 82, 98



! create keypoints for tip spline
        KL, 70, .5,,
        KL, 71, .5,,
        KL, 72, .5,,
        KL, 73, .5,,
        KL, 74, .5,,
        KL, 75, .5,,
        KL, 76, .5,,
        KL, 77, .5,,
        KL, 78, .5,,
        KL, 79, .5,,
        KL, 80, .5,,
        KL, 81, .5,,
        KL, 82, .5,,

! create tip spline
        KSEL,S,KP,,57
        KSEL,A,KP,,71
```

```
        KSEL,A,KP,,86,97,1

        BSPLIN,all,
        ALLSEL,all

! create wing tip areas
        LSEL,S,LINE,,42,55,1
        LSEL,A,LINE,,111
        AL,all

        LSEL,S,LINE,,56,69,1
        LSEL,A,LINE,,111
        AL,all

        ALLSEL, all

! create components

  !a_endcap
   ASEL,S,AREA,,42,43,1
   CM,a_endcap,AREA

  !A_RESTRAINT
   ASEL,S,AREA,,1,28,1
   CM,a_restraint,AREA

  !A_SPARS
   ASEL,S,AREA,,29,41,1
   CM,a_spars,AREA

  !L_ENDSEAM
        LSEL,S,LINE,,111
   CM,l_endseam,LINE

  !L_TIP
        CMSEL,S,l_tip
        CMSEL,A,l_endseam
        CM,l_tip,LINE

! Reverse area normals
        CMSEL,S,a_endcap
        CMSEL,A,a_restraint
        AREVERSE,all,0

        ALLSEL, all
```

```
! Define Element type and real constants
        ET,1,SHELL181
        R,1,.013,,,,,,
        RMORE,,,,,,,

! define material properties

        *CREATE,file1.UNIA
    0 0
    0.058268908 2915
    0.072320662 5375
    0.086177696 11990
    0.122217633 39550
        *END
        TBFT,EADD,1,UNIA,file1.UNIA
        /DELETE,file1.UNIA
        TBFT,FADD,1,HYPER,MOON,3
        TBFT,SOLVE,1,HYPER,MOON,3,1
        TBFT,FSET,1,HYPER,MOON,3

! Set mesh sizing for warp direction
        CMSEL,U,L_ROOT
        CMSEL,U,L_TIP
        LESIZE,all,,,25,0.5,1,,,0
        ALLSEL,ALL

! mesh
        CMSEL,U,A_ENDCAP
        amesh, all

! mesh endcap
        CMSEL,S,l_endseam
        LESIZE,all, , ,30,.5,1 , , ,0
        ALLSEL,ALL
        CMSEL,S,A_ENDCAP
        amesh, all

!create "servo" patches
!patch 1

        NSEL,S,NODE,,1977
    NSEL,A,NODE,,2010
    NSEL,A,NODE,,2011
    NSEL,A,NODE,,2237
    NSEL,A,NODE,,2238
    NSEL,A,NODE,,2239
```

NSEL,A,NODE,,2240
NSEL,A,NODE,,2241
NSEL,A,NODE,,2242
NSEL,A,NODE,,2243
NSEL,A,NODE,,2244
NSEL,A,NODE,,2268
NSEL,A,NODE,,2269
NSEL,A,NODE,,2431
NSEL,A,NODE,,2432
NSEL,A,NODE,,2433
NSEL,A,NODE,,2434
NSEL,A,NODE,,2435
NSEL,A,NODE,,2436
NSEL,A,NODE,,2437
NSEL,A,NODE,,2438
NSEL,A,NODE,,2439
NSEL,A,NODE,,2440
NSEL,A,NODE,,2441
NSEL,A,NODE,,2442
NSEL,A,NODE,,2443
NSEL,A,NODE,,2444
NSEL,A,NODE,,2445
NSEL,A,NODE,,2446
NSEL,A,NODE,,2447
NSEL,A,NODE,,2448
NSEL,A,NODE,,2449
NSEL,A,NODE,,2450
NSEL,A,NODE,,2451
NSEL,A,NODE,,2475
NSEL,A,NODE,,2476
NSEL,A,NODE,,2615
NSEL,A,NODE,,2616
NSEL,A,NODE,,2617
NSEL,A,NODE,,2618
NSEL,A,NODE,,2619
NSEL,A,NODE,,2620
NSEL,A,NODE,,2621
NSEL,A,NODE,,2622
NSEL,A,NODE,,2623
NSEL,A,NODE,,2624
NSEL,A,NODE,,2625
NSEL,A,NODE,,2626
CM,patch_1,NODE

ALLSEL, ALL

!patch 2

NSEL,S,NODE,,2005
NSEL,A,NODE,,2006
NSEL,A,NODE,,2007
NSEL,A,NODE,,2263
NSEL,A,NODE,,2264
NSEL,A,NODE,,2265
NSEL,A,NODE,,2396
NSEL,A,NODE,,2397
NSEL,A,NODE,,2398
NSEL,A,NODE,,2399
NSEL,A,NODE,,2400
NSEL,A,NODE,,2401
NSEL,A,NODE,,2402
NSEL,A,NODE,,2403
NSEL,A,NODE,,2404
NSEL,A,NODE,,2405
NSEL,A,NODE,,2406
NSEL,A,NODE,,2407
NSEL,A,NODE,,2408
NSEL,A,NODE,,2409
NSEL,A,NODE,,2410
NSEL,A,NODE,,2411
NSEL,A,NODE,,2412
NSEL,A,NODE,,2413
NSEL,A,NODE,,2414
NSEL,A,NODE,,2415
NSEL,A,NODE,,2416
NSEL,A,NODE,,2470
NSEL,A,NODE,,2471
NSEL,A,NODE,,2472
NSEL,A,NODE,,2585
NSEL,A,NODE,,2586
NSEL,A,NODE,,2587
NSEL,A,NODE,,2588
NSEL,A,NODE,,2589
NSEL,A,NODE,,2590
NSEL,A,NODE,,2591
NSEL,A,NODE,,2592
NSEL,A,NODE,,2593
NSEL,A,NODE,,2594
NSEL,A,NODE,,2595
NSEL,A,NODE,,2596
NSEL,A,NODE,,2597
NSEL,A,NODE,,2598

```
NSEL,A,NODE,,2599
NSEL,A,NODE,,2600
NSEL,A,NODE,,2601
NSEL,A,NODE,,2602
CM,patch_2,NODE

ALLSEL, ALL

!patch 3

      NSEL,S,NODE,,2000
NSEL,A,NODE,,2001
NSEL,A,NODE,,2002
NSEL,A,NODE,,2258
NSEL,A,NODE,,2259
NSEL,A,NODE,,2260
NSEL,A,NODE,,2361
NSEL,A,NODE,,2362
NSEL,A,NODE,,2363
NSEL,A,NODE,,2364
NSEL,A,NODE,,2365
NSEL,A,NODE,,2366
NSEL,A,NODE,,2367
NSEL,A,NODE,,2368
NSEL,A,NODE,,2369
NSEL,A,NODE,,2370
NSEL,A,NODE,,2371
NSEL,A,NODE,,2372
NSEL,A,NODE,,2373
NSEL,A,NODE,,2374
NSEL,A,NODE,,2375
NSEL,A,NODE,,2376
NSEL,A,NODE,,2377
NSEL,A,NODE,,2378
NSEL,A,NODE,,2379
NSEL,A,NODE,,2380
NSEL,A,NODE,,2381
NSEL,A,NODE,,2465
NSEL,A,NODE,,2466
NSEL,A,NODE,,2467
NSEL,A,NODE,,2555
NSEL,A,NODE,,2556
NSEL,A,NODE,,2557
NSEL,A,NODE,,2558
NSEL,A,NODE,,2559
NSEL,A,NODE,,2560
```

```
   NSEL,A,NODE,,2561
   NSEL,A,NODE,,2562
   NSEL,A,NODE,,2563
   NSEL,A,NODE,,2564
   NSEL,A,NODE,,2565
   NSEL,A,NODE,,2566
   NSEL,A,NODE,,2567
   NSEL,A,NODE,,2568
   NSEL,A,NODE,,2569
   NSEL,A,NODE,,2570
   NSEL,A,NODE,,2571
   NSEL,A,NODE,,2572
   CM,patch_3,NODE

   ALLSEL, ALL


! create tip force component on bottom
        NSEL,S,NODE,,3227
        CM,n_tip_load_up,NODE

        ALLSEL,ALL

! Save database
        SAVE

!#########################################################
! Solution

! set solution options
        /SOLU

        NLGEOM,ON
        NSUBST,2000,20000,300
        LNSRCH,ON

! apply constraints on root
        CMSEL,S,l_root_constr
        DL,all,,ALL,


! apply internal pressure
        CMSEL,S,a_restraint
        CMSEL,A,a_endcap
        SFA,all,1,PRES,int_press
        ALLSEL,ALL
```

```
        SSTIF,ON
        SOLVE

        SAVE,nonlin_matl_10psi_soln,db

!! apply patch 1 load
        CMSEL,S,patch_1
        F,all,MX,-warp_mom/48

        ALLSEL,ALL

!! apply patch 1 load
!       CMSEL,S,patch_2
!       F,all,MX,-warp_mom/48

!       ALLSEL,ALL

!! apply patch 1 load
!       CMSEL,S,patch_3
!       F,all,MX,-warp_mom/48

!       ALLSEL,ALL

        SSTIF,ON
        SOLVE

FINISH
!/exit, nosave
```

APPENDIX B: ADDITIONAL EXPERIMENTAL TEST DATA

This appendix includes experimental data of multiple wings. Each wing is labeled by its serial number.

Bending Data, Internal pressure of 10 psi:

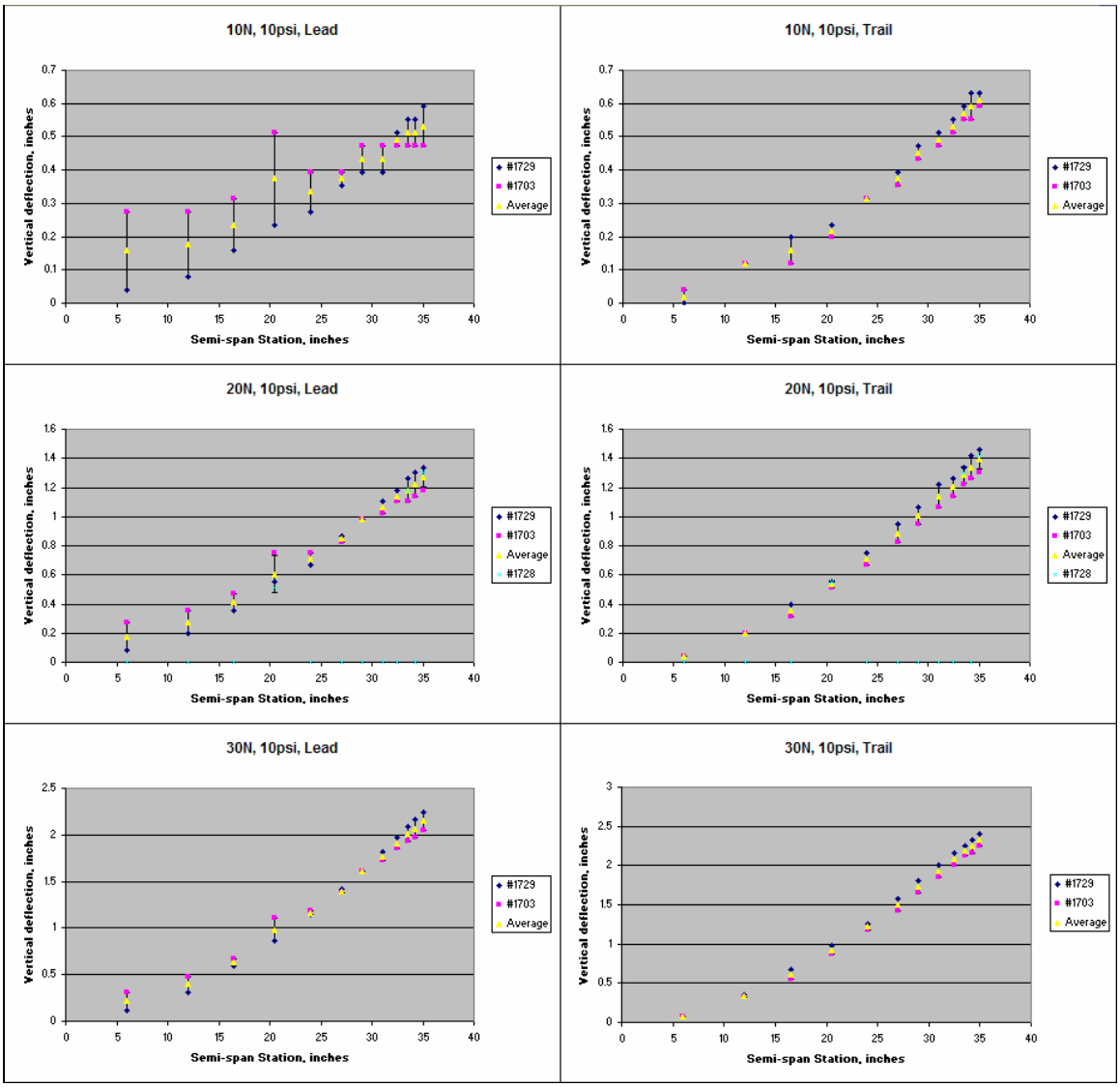

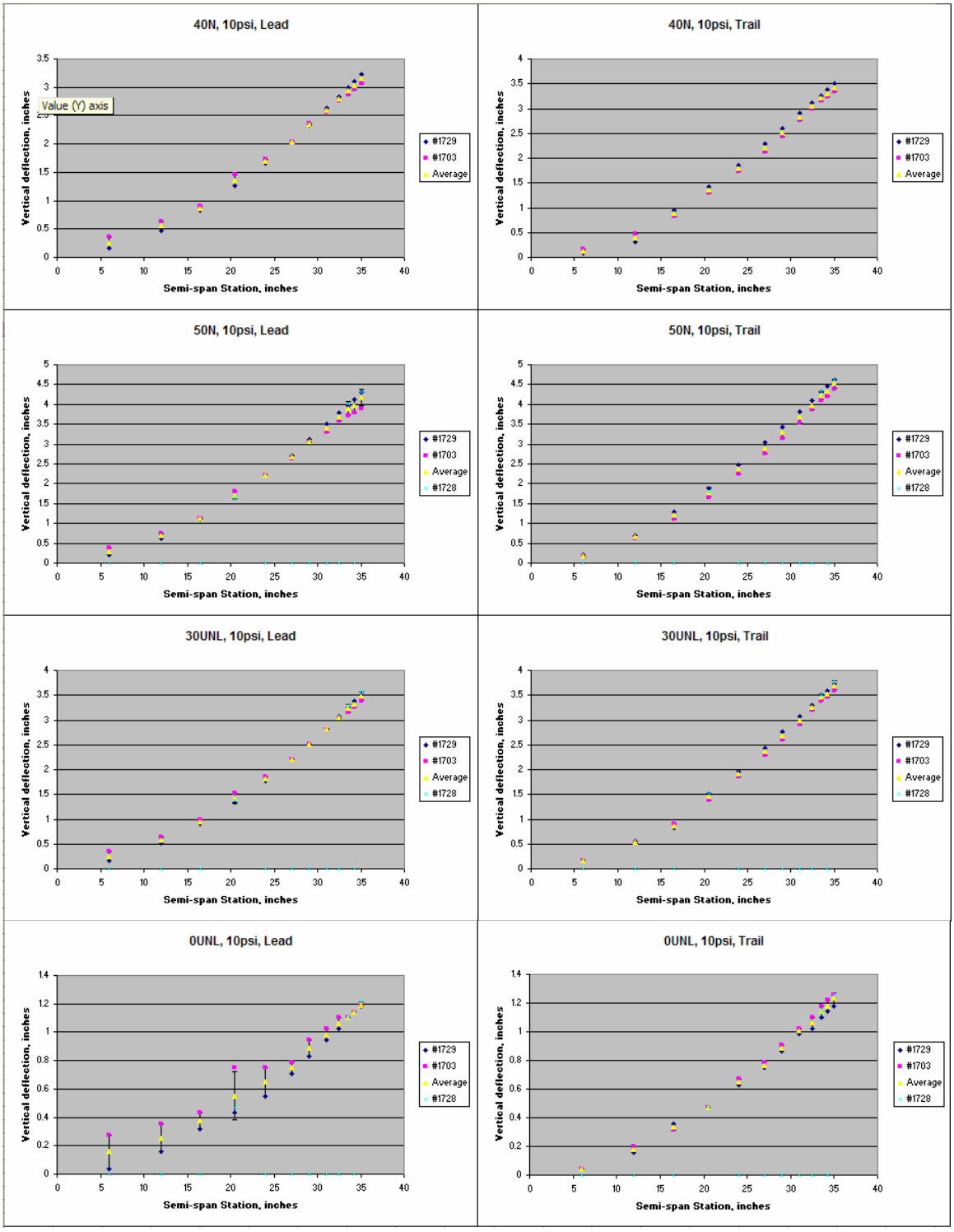
40N, 10psi, Lead
Value (Y) axis
Vertical deflection, inches
Semi-span Station, inches
#1729
#1703
Average
40N, 10psi, Trail
Vertical deflection, inches
Semi-span Station, inches
#1729
#1703
Average
50N, 10psi, Lead
Vertical deflection, inches
Semi-span Station, inches
#1729
#1703
Average
#1728
50N, 10psi, Trail
Vertical deflection, inches
Semi-span Station, inches
#1729
#1703
Average
#1728
30UNL, 10psi, Lead
Vertical deflection, inches
Semi-span Station, inches
#1729
#1703
Average
#1728
30UNL, 10psi, Trail
Vertical deflection, inches
Semi-span Station, inches
#1729
#1703
Average
#1728
0UNL, 10psi, Lead
Vertical deflection, inches
Semi-span Station, inches
#1729
#1703
Average
#1728
0UNL, 10psi, Trail
Vertical deflection, inches
Semi-span Station, inches
#1729
#1703
Average
#1728

Bending Data, Internal pressure of 15 psi:

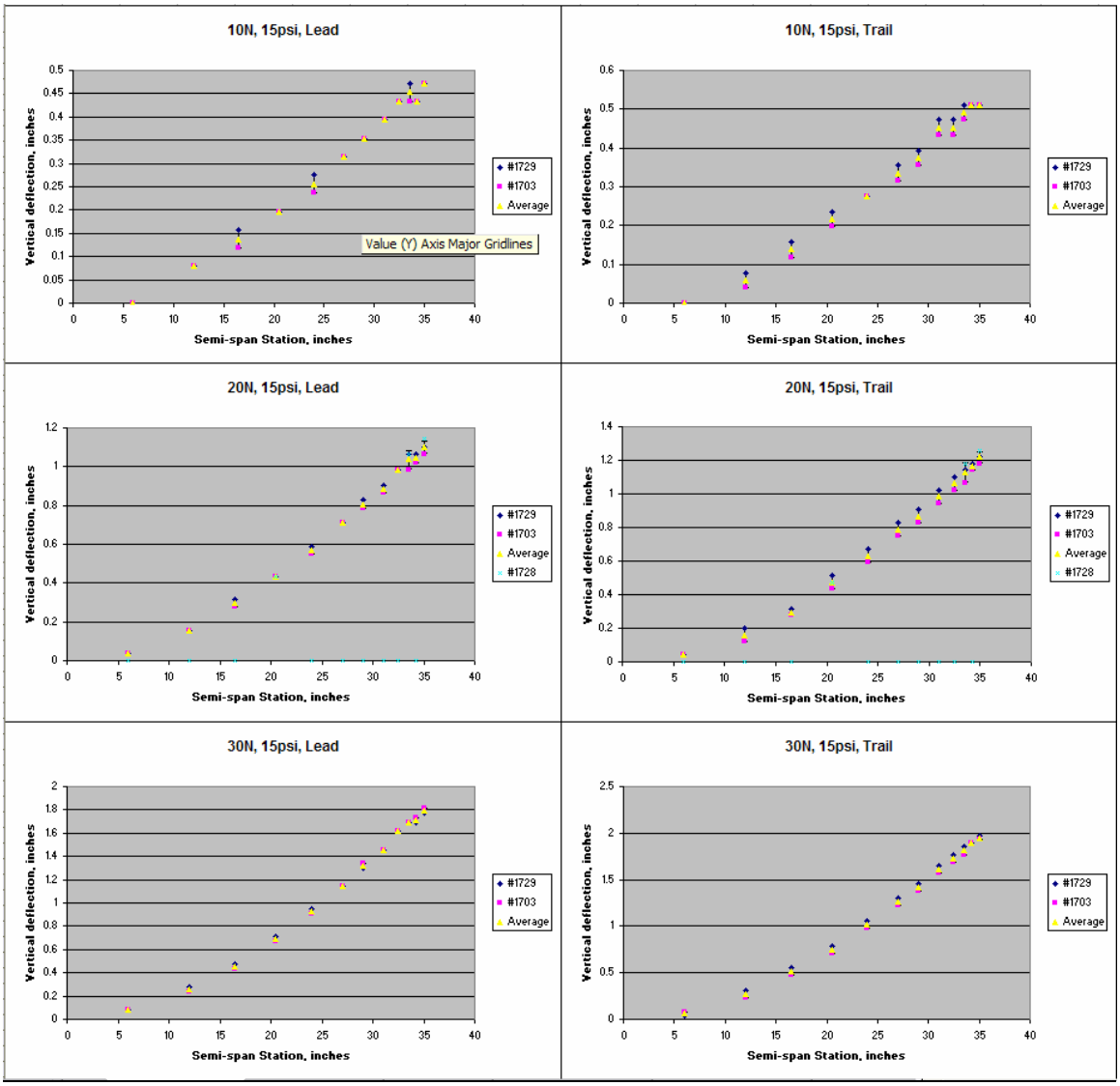

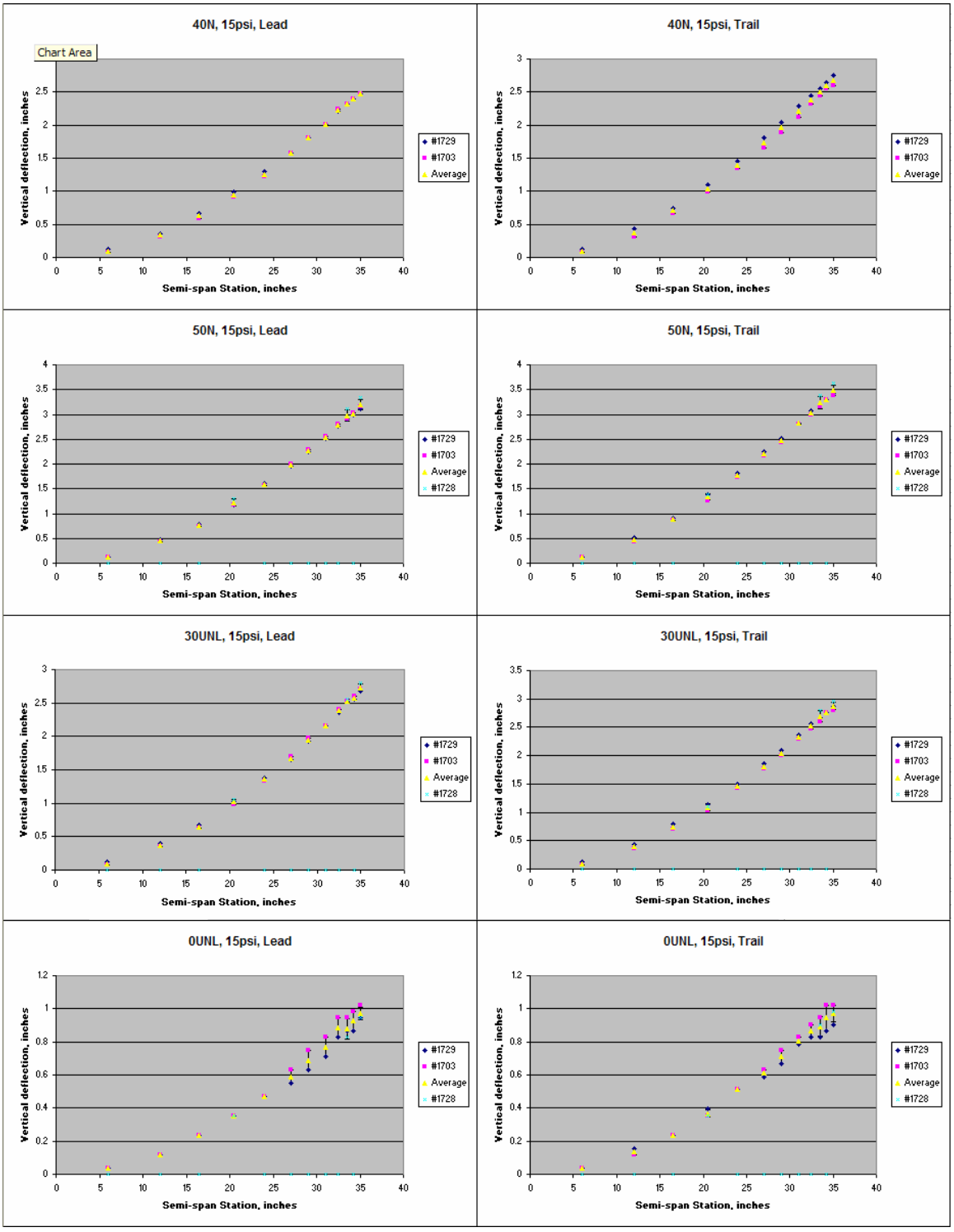
40N, 15psi, Lead
Chart Area
Vertical deflection, inches
Semi-span Station, inches
#1729
#1703
Average
40N, 15psi, Trail
Vertical deflection, inches
Semi-span Station, inches
#1729
#1703
Average
50N, 15psi, Lead
Vertical deflection, inches
Semi-span Station, inches
#1729
#1703
Average
#1728
50N, 15psi, Trail
Vertical deflection, inches
Semi-span Station, inches
#1729
#1703
Average
#1728
30UNL, 15psi, Lead
Vertical deflection, inches
Semi-span Station, inches
#1729
#1703
Average
#1728
30UNL, 15psi, Trail
Vertical deflection, inches
Semi-span Station, inches
#1729
#1703
Average
#1728
0UNL, 15psi, Lead
Vertical deflection, inches
Semi-span Station, inches
#1729
#1703
Average
#1728
0UNL, 15psi, Trail
Vertical deflection, inches
Semi-span Station, inches
#1729
#1703
Average
#1728

Bending Data, Internal pressure of 20 psi:

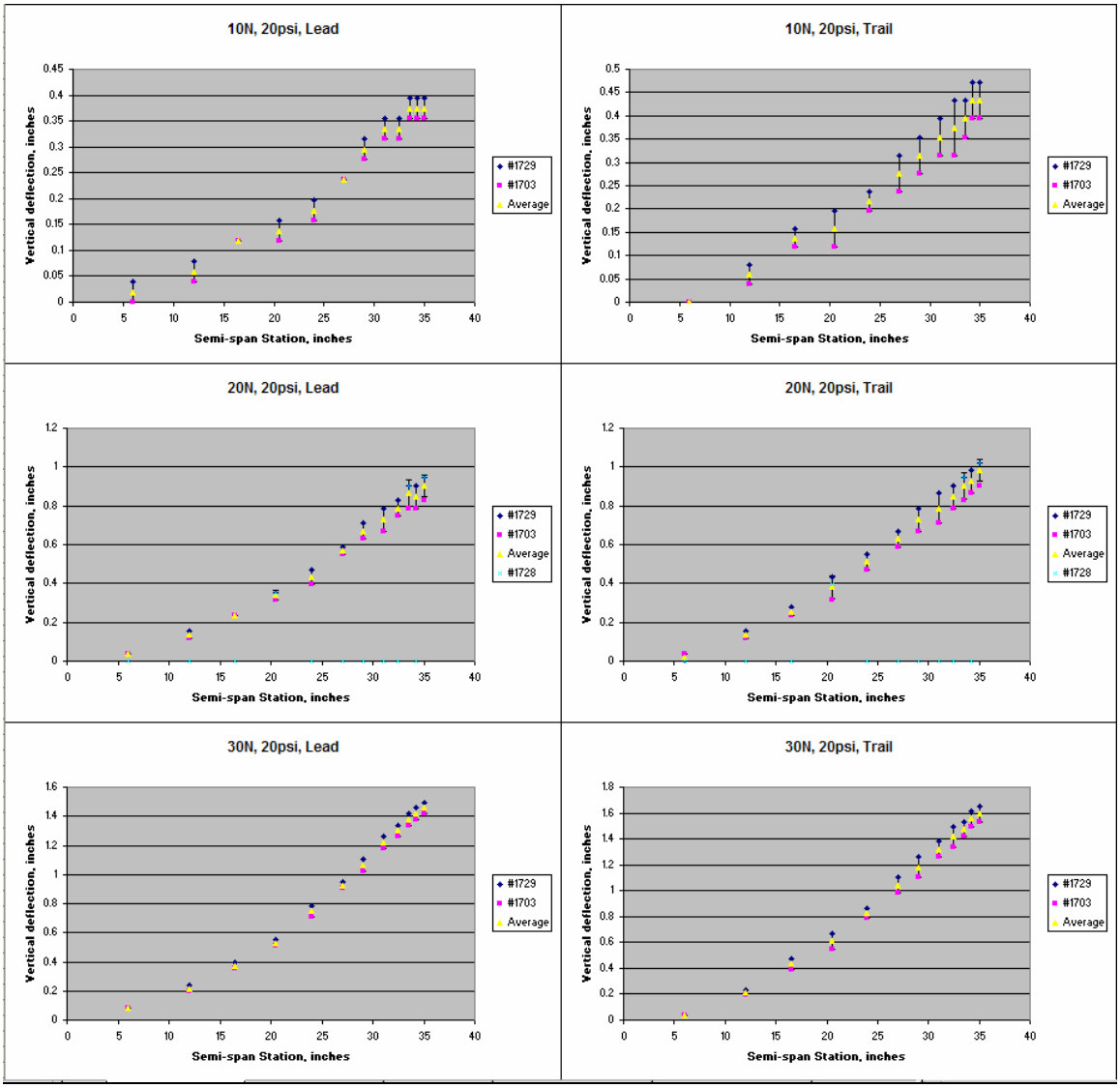

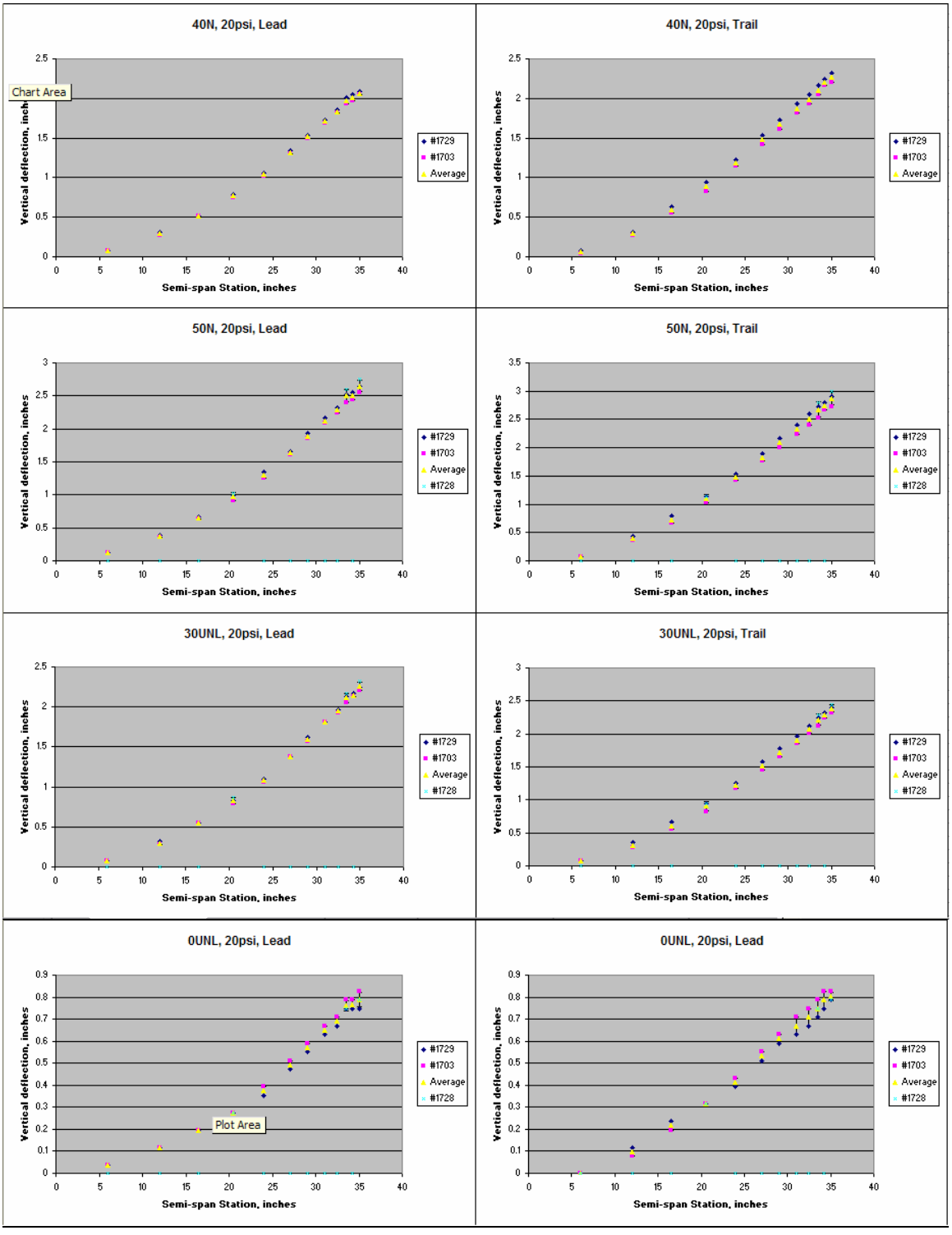
40N, 20psi, Lead
Chart Area
Vertical deflection, inches
Semi-span Station, inches
#1729
#1703
Average
40N, 20psi, Trail
Vertical deflection, inches
Semi-span Station, inches
#1729
#1703
Average
50N, 20psi, Lead
Vertical deflection, inches
Semi-span Station, inches
#1729
#1703
Average
#1728
50N, 20psi, Trail
Vertical deflection, inches
Semi-span Station, inches
#1729
#1703
Average
#1728
30UNL, 20psi, Lead
Vertical deflection, inches
Semi-span Station, inches
#1729
#1703
Average
#1728
30UNL, 20psi, Trail
Vertical deflection, inches
Semi-span Station, inches
#1729
#1703
Average
#1728
0UNL, 20psi, Lead
Plot Area
Vertical deflection, inches
Semi-span Station, inches
#1729
#1703
Average
#1728
0UNL, 20psi, Lead
Vertical deflection, inches
Semi-span Station, inches
#1729
#1703
Average
#1728

Torsion Data, Internal pressure of 10 psi:

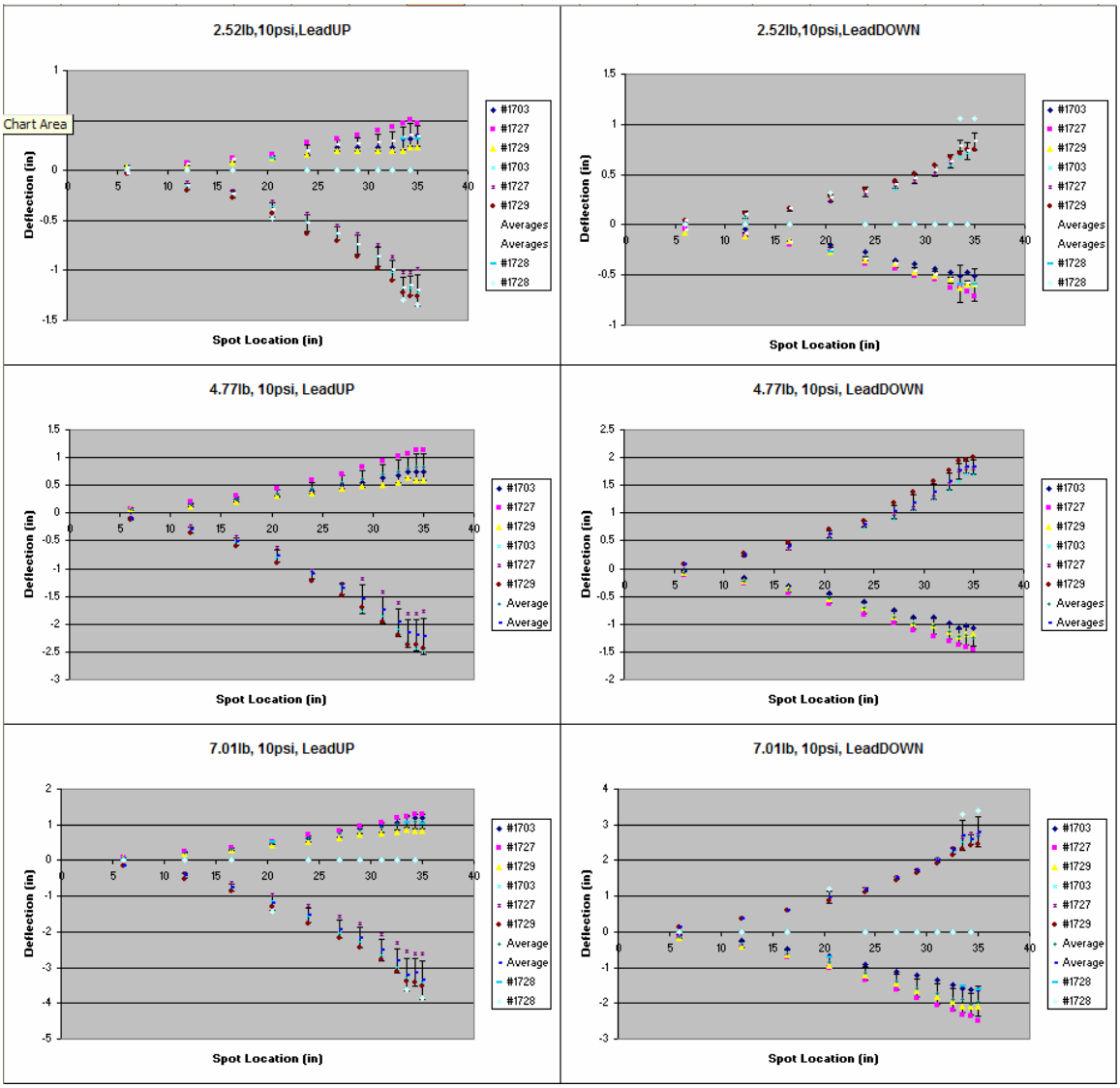

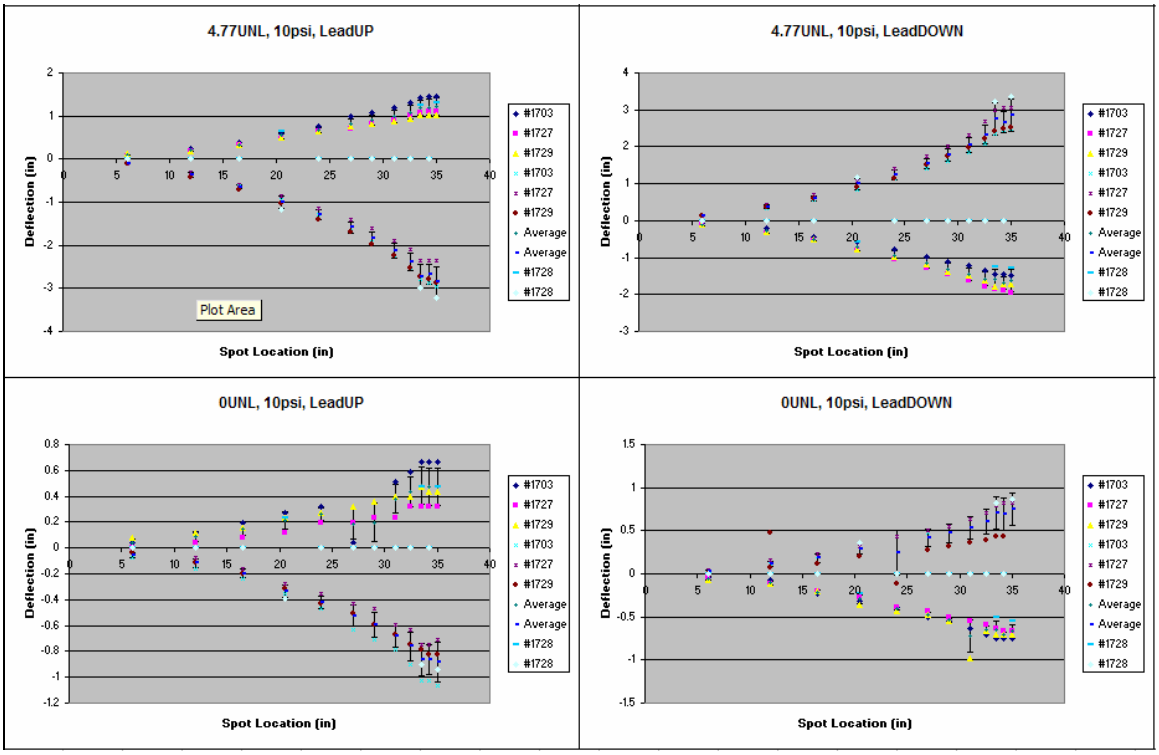
4.77UNL, 10psi, LeadUP
Deflection (in)
Spot Location (in)
Plot Area
#1703
#1727
#1729
#1703
#1727
#1729
Average
Average
#1728
#1728
4.77UNL, 10psi, LeadDOWN
Deflection (in)
Spot Location (in)
#1703
#1727
#1729
#1703
#1727
#1729
Average
Average
#1728
#1728
0UNL, 10psi, LeadUP
Deflection (in)
Spot Location (in)
#1703
#1727
#1729
#1703
#1727
#1729
Average
Average
#1728
#1728
0UNL, 10psi, LeadDOWN
Deflection (in)
Spot Location (in)
#1703
#1727
#1729
#1703
#1727
#1729
Average
Average
#1728
#1728

Torsion Data, Internal pressure of 15 psi:

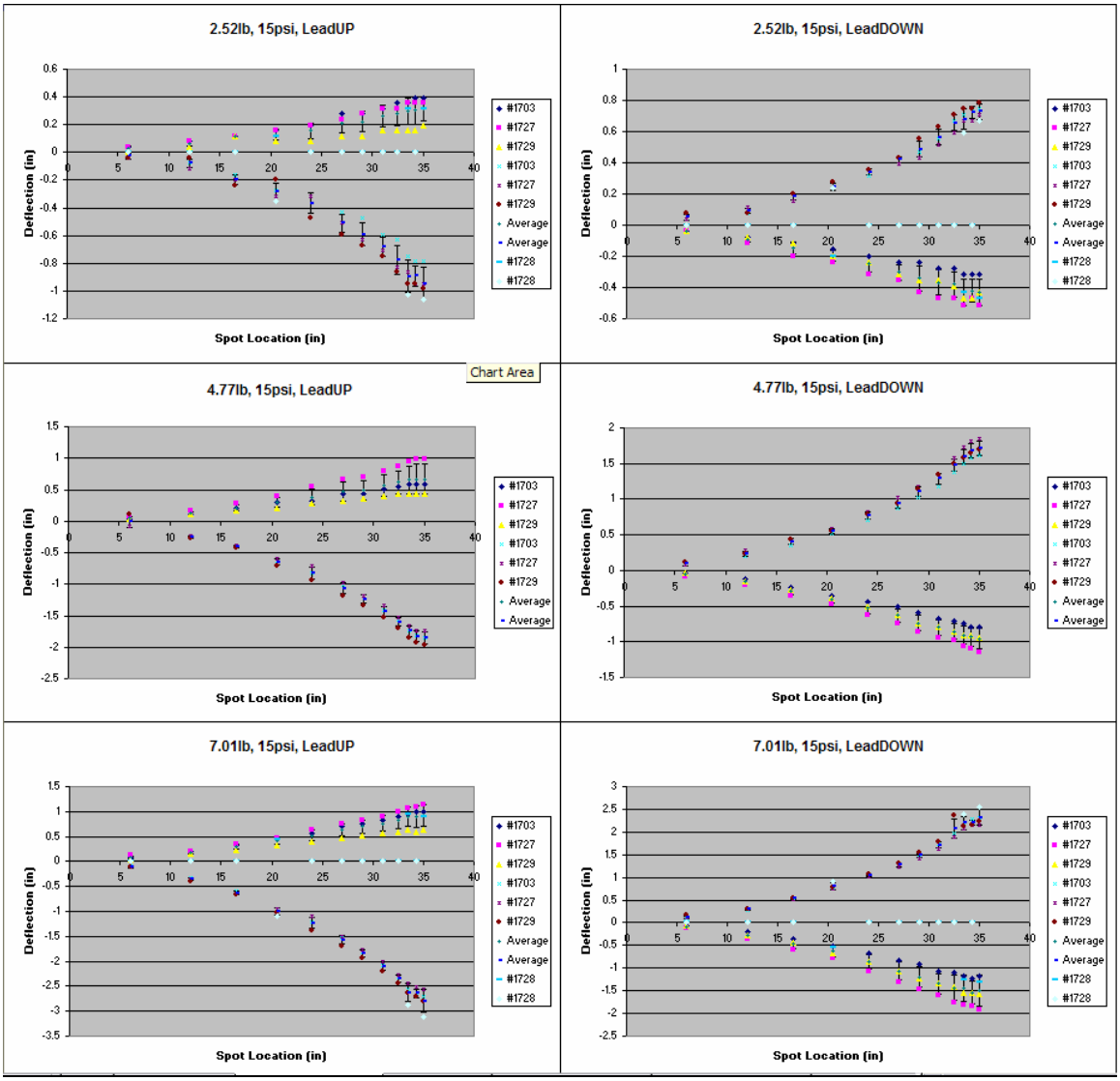

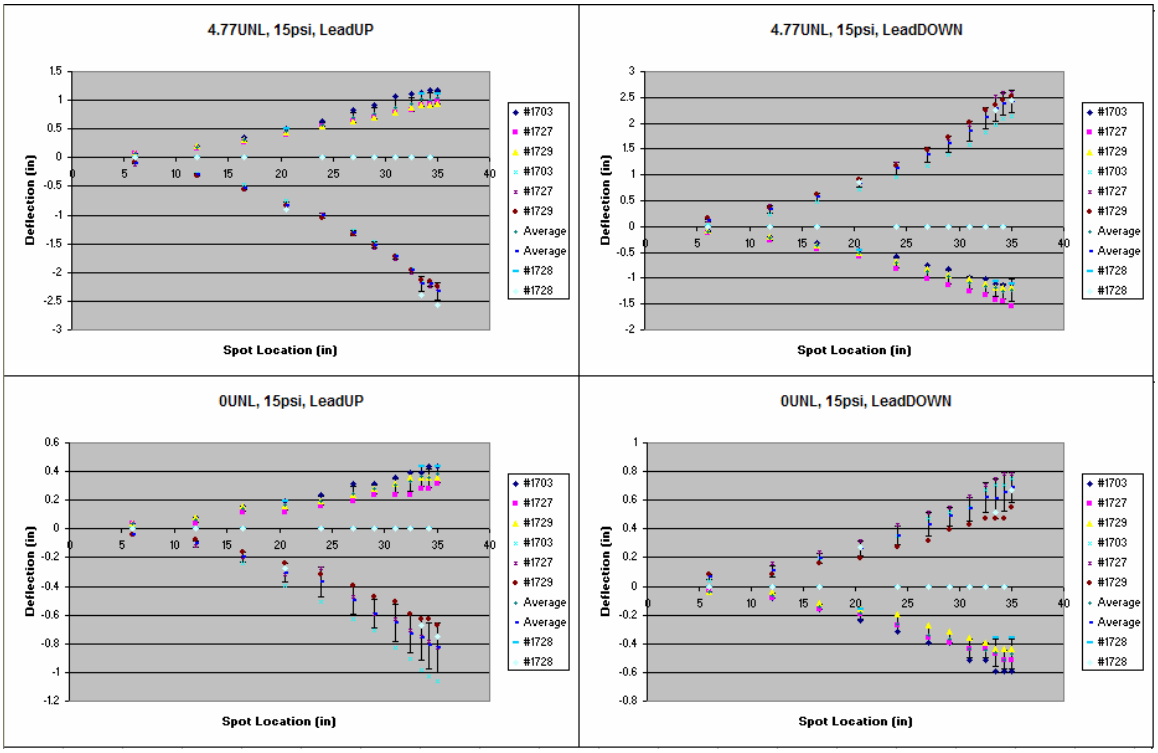
4.77UNL, 15psi, LeadUP
Deflection (in)
Spot Location (in)
#1703
#1727
#1729
#1703
#1727
#1729
Average
Average
#1728
#1728
4.77UNL, 15psi, LeadDOWN
Deflection (in)
Spot Location (in)
#1703
#1727
#1729
#1703
#1727
#1729
Average
Average
#1728
#1728
0UNL, 15psi, LeadUP
Deflection (in)
Spot Location (in)
#1703
#1727
#1729
#1703
#1727
#1729
Average
Average
#1728
#1728
0UNL, 15psi, LeadDOWN
Deflection (in)
Spot Location (in)
#1703
#1727
#1729
#1703
#1727
#1729
Average
Average
#1728
#1728

Torsion Data, Internal pressure of 20 psi:

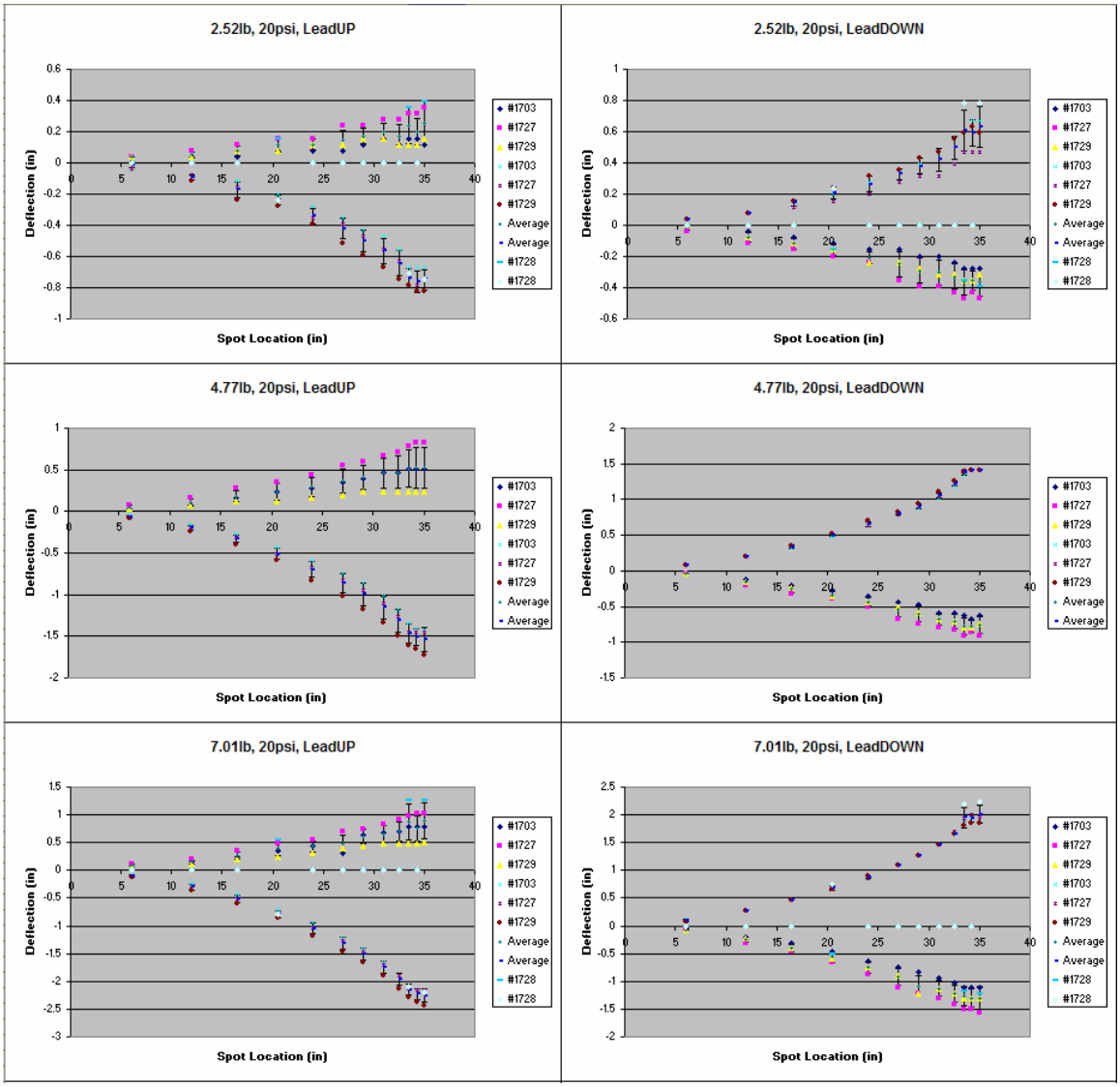

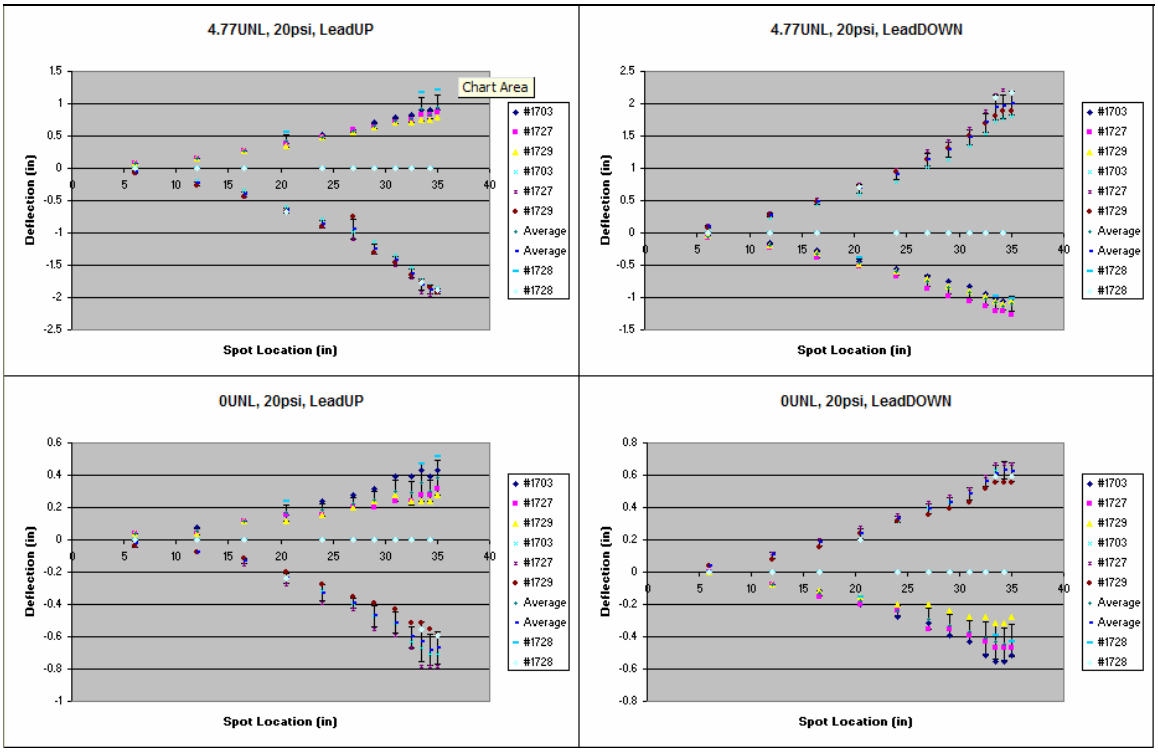
4.77UNL, 20psi, LeadUP
Chart Area
Deflection (in)
Spot Location (in)
#1703
#1727
#1729
#1703
#1727
#1729
Average
Average
#1728
#1728
4.77UNL, 20psi, LeadDOWN
Deflection (in)
Spot Location (in)
#1703
#1727
#1729
#1703
#1727
#1729
Average
Average
#1728
#1728
0UNL, 20psi, LeadUP
Deflection (in)
Spot Location (in)
#1703
#1727
#1729
#1703
#1727
#1729
Average
Average
#1728
#1728
0UNL, 20psi, LeadDOWN
Deflection (in)
Spot Location (in)
#1703
#1727
#1729
#1703
#1727
#1729
Average
Average
#1728
#1728

REFERENCES

1. *2007 Worldwide UAV Roundup,* in *Supplement to Aerospace America*. 2007.

2. Jacob, J.D., A.D. Simpson, and S. Smith, *Design and Flight Testing of Inflatable Wings with Wing Warping.* SAE Transactions Journal of Aerospace, 2005: p. pp. 1306-1315.

3. Simpson, A., A. Santhanakrishnan, J. Jacob, and S. Smith, *Flying on Air: UAV Flight Testing with Inflatable Wing Technology*, in *3rd "Unmanned Unlimited" Technical Conference, Workshop and Exhibit*. 2004, AIAA: Chicago, Illinois.

4. Murray, J., et al., *Ground and Flight Evaluation of a Small-Scale Inflatable-Winged Aircraft*, in *40th Aerospace Sciences Meeting & Exhibit*. 2002, AIAA: Reno, NV.

5. Cadogan, D., T. Smith, F. Uhelsky, M. MacKusick, *Morphing Inflatable Wing Development for Compact Package Unmanned Aerial Vehicles*, in *45th AIAA/ASME/ASCE/AHS/ASC Structures, Structural Dynamics and Materials Conference*. 2004, AIAA: Palm Springs, California.

6. Simpson, A., M. Usui, S. Smith, and J.D. Jacob, *Aeromechanics of Inflatable Wings*, in *AIAA 34th Fluid Dynamics Conference*. 2004, AIAA: Portland, OR.

7. Simpson, A.D., M. Usui, S.W. Smith, J.D. Jacob, *Development and Flight Testing of a UAV with Inflatable-Rigidizable Wings*, in *42nd AIAA Aerospace Sciences Meeting and Exhibit*. 2004, AIAA: Reno, NV.

8. Cadogan, D., T. Smith, R. Lee, S. Scarborough, D. Graziosi, *Inflatable and Rigidizable Wing Components for Unmanned Aerial Vehicles*, in *44th AIAA/ASME/ASCE/AHS/ASC Structures, Structural Dynamics and Materials Conference*. 2003, AIAA Norfolk, VA.

9. Allred, R., A. Hoyt, L. Harrah, P. McElroy, S. Scarborough, D. Cadogan, *Light Curing Rigidizable Inflatable Wing*, in *45th AIAA/ASME/ASCE/AHS/ASC Structures, Structural Dynamics and Materials Conference*. 2004, AIAA: Palm Springs, CA.

10. Smith, S.C., et. al., *The Design of the Canyon Flyer, an Airplane for Mars Exploration*, in *42nd AIAA Aerospace Sciences Meeting and Exhibit*. 2000, AIAA: Reno NV.

11. *Robotic Access to Planetary Surfaces*, NASA Science Mission Directorate.

12. Kearns, J., M. Usui, S. Smith, S. Scarborough, T. Smith, D. Cadogan, *Development of UV-Curable Inflatable Wings for Low Density Flight Applications*, in *5th AIAA Gossamer Spacecraft Forum*. 2004, AIAA: Palm Springs, CA.

13. Smith, S.W., J.D. Jacob, R. Jones, S. Scarborough and D. Cadogan, *A High-Altitude Test of Inflatable Wings for Low-Density Flight Applications*, in *7th AIAA Gossamer Spacecraft Forum*. 2006, AIAA: Newport, RI.

14. Usui, M., J.D. Jacob, S.W. Smith, S. Scarborough and D. Cadogan, *Second Generation Inflatable/RigidizableWings for Low-Density Applications*, in *6th AIAA Gossamer Spacecraft Forum*. 2005, AIAA: Austin, TX.

15. Usui, M., *Design of Inflatable-Rigidizable Wings for Low-Density Flight Applications*, in *Dept. of Mechanical Engineering*. 2004, University of Kentucky: Lexington, KY.

16. *http://www.nasm.si.edu/research/aero/aircraft/goodyear_xao.htm*.

17. *http://www.ilcdover.com/products/aerospace_defense/uavwings.htm*.

18. Cadogan, D., et al., *Recent Development and Test of Inflatable Wings*, in *AIAA SDM Conference*. 2006, AIAA: Newport, Rhode Island.

19. Jacob, J.D., S.W. Smith, D. Cadogan and S. Scarborough, *Expanding the Small UAV Design Space with Inflatable Wings*, in *SAE AeroTech Congress and Exhibition*. 2007, SAE: Los Angeles, CA.

20. Jacob, J.D., S.W. Smith, D. Cadogan and S. Scarborough, *Inflatable Wings as a UAV Design Alternative*, in *AUVSI Unmanned Systems North America 2007*. 2007: Washington DC.

21. Jacob, J.D., A.D. Simpson, and S.W. Smith, *Design and Flight Testing of Inflatable Wings with Wing Warping*, in *SAE World Aerospace Congress*. 2005, SAE: Dallas, Texas.

22. Simpson, A., J.D. Jacob and S.W. Smith, *Flight Control of a UAV with Inflatable Wings with Wing Warping*, in *24th AIAA Applied Aerodynamics Conference*. 2006, AIAA: San Francisco, California.

23. Simpson, A., N. Coulombe, J.D. Jacob, and S.W. Smith, *Morphing of Inflatable Wings*, in *AIAA SDM Adaptive Structures Conference*. 2005: Austin, TX.

24. Simpson, A., O.Rawashdeh., J.D. Jacob, J.E. Lumpp, W.T. Smith and S.W. Smith, *BIG BLUE II: Mars Aircraft Prototype with Inflatable-Rigidizable Wings*, in *AIAA Unmanned Unlimited Conference*. 2004: Chicago, IL.

25. Simpson, A.D., J.M. Rowe, S.W. Smith and J.D. Jacob, *Aeroelastic Deformation and Buckling of Inflatable Wings Under Dynamic Loads*, in *48th AIAA/ASME/ASCE/AHS/ASC Structures, Structural Dynamics, and Materials Conference*. 2007, AIAA: Honolulu, Hawaii.

26. Simpson, A.D., S.W. Smith and J.D. Jacob, *Aeroelastic Behavior of Inflatable Wings: Wind Tunnel and Flight Testing*, in *45th Aerospace Sciences Meeting*. 2007, AIAA: Reno, Nevada.

27. Simpson, A.D., J.D. Jacob and S.W. Smith, *Inflatable and Warpable Wings for Meso-Scale UAVs*, in *AIAA Infotech@Aerospace Conference*. 2005: Arlington, Virginia.

28. Simpson, A.D., et. al., *BIG BLUE: A High-Altitude UAV Demonstrator of Mars Airplane Technology*, in *IEEE Aerospace Conference*: Big Sky, MT.

29. Simpson, A., *Design and Performance of UAVs with Inflatable Wings*, in *Mechanical Engineering*. 2007, University of Kentucky: Lexington, KY.

30. Campbell, J.E., S.W. Smith, J.A. Main, and J. Kearns, *Staged Microgravity Deployment of a Pressurizing Scale Model Spacecraft.* AIAA Journal of Spacecraft and Rockets, 2004. **Vol. 41**(No. 4): p. 534-542.

31. Main, J.A., P.S. Peterson, A.M. Strauss, *Beam-Type Bending of Space-Based Inflated Membrane Structures.* Journal of Aerospace Engineering, 1995. **Vol. 8**(No. 2): p. 120-125.

32. Smith, S.W., and J.A. Main, *Modeling the Deployment of Inflating Space Structures.* Gossamer Spacecraft: Membrane/Inflatable Structures Technologies for Space Applications, 2001: p. 203-241.

33. Welch, A.L., and S.W. Smith, *Experimental Results Regarding Two-Dimensional Deployment of Inflatable Beams*, in *4th AIAA SDM Gossamer Spacecraft Forum.* 2003, AIAA: Norfolk, Virginia.

34. Rendall, C.Chang., P. Marzocca, E. Bollt and P. Zamankhan, *Aeroelastic Behavior of a Non-rigidizable Inflatable UAV Wing*, in *47th AIAA/ASME/ASCE/AHS/ASC Structures, Structural Dynamics, and Materials Conference*. 2006, AIAA: Newport, Rhode Island.

35. Rendall, C.Cormier., P. Marzocca, and R. Jha, *Static, Buckling and Dynamic Behavior of Inflatable Beams*, in *47th AIAA/ASME/ASCE/AHS/ASC Structures, Structural Dynamics, and Materials Conference*. 2006, AIAA: Newport, Rhode Island.

36. Griffith, D.T., *Experimental and Analytical Modal Analyses of an Inflated Thin Film Torus*, in *Dept. of Mechanical Engineering*. 2000, University of Kentucky: Lexington, KY.

37. Slade, K.N., M. L. Tinker, J. O. Lassiter, and R. Engberg, *Dynamics of an Inflatable Structure in Vacuum and Ambient Conditions.* AIAA Journal, 2001. **Vol. 39**(No. 5): p. 894-901.

38. Song, H., S.W. Smith, and J.A. Main, *Dynamic Testing of an Inflatable, Self-Supporting, Unpressurized Thin-Film Torus.* Journal of Guidance, Control, and Dynamics, 2006. **Vol. 29**(No. 4): p. 839-845.

39. Gere, J.M., and S.P. Timoshenko, *Mechanics of Materials*. 4th ed. 1997, Park Plaza, Boston: PWS Publishing Co.

40. *ANSYS 8.0 Documentation*. 2003, SAS IP, Inc.

41. *http://www.aeroplanemonthly.com/glossary/*.

VITA

Johnathan Michael Rowe

Birthplace:
Somerset, KY, September 8, 1982

Education:
University of Kentucky, Lexington, KY
B.S. in Mechanical Engineering, with a Minor in Mathematics

Experience:
Graduate Research Assistant, University of Kentucky, Aug. 2005-Present.

Cooperative Education Student FE Analyst, Belcan Corporation, West Palm Beach, FL, May – Aug., 2003, and Jan. – Aug. 2004.

Honors and Awards:
- Recipient of Fellowship from the Kentucky Space Grant Consortium
- Recipient of Fellowship from the Center for Computational Sciences at UK
- Student Member AIAA, SEM
- Member Order of the Engineer

Publications:
- **Rowe, J.M.**, Smith, S.W., *Challenges of Modeling Inflatable Wings*, AIAA-2007-1848, 48th AIAA/ASME/ASCE/AHS/ASC Structures, Structural Dynamics & Materials Conference, 8th AIAA Gossamer Spacecraft Forum, April 23-26, 2007, Honolulu, Hawaii

- **Rowe, J.M.**, Smith, S.W., Simpson, A.D, Jacob, J.D., *Preliminary Modal Analysis of Inflatable Wings*, Paper No. 194, 25th SEM IMAC Conference, February 19-22, 2007, Orlando, Florida

- **Rowe, J.M.**, Smith, S.W., Simpson, A.D, Jacob, J.D., Scarborough, S.E. *Development of a Finite Element Model of Warping Inflatable Wings*, AIAA-2006-1697, 47th AIAA/ASME/ASCE/AHS/ASC Structures, Structural Dynamics & Materials Conference, 7th AIAA Gossamer Spacecraft Forum, May 1-4, 2006, Newport, Rhode Island

Presentations:
- *AIRCAT: Development of Unmanned Aerial Vehicle Technology*, presented as part of the William Maxwell Reed Mechanical Engineering Seminar series at the University of Kentucky, November 3, 2005